# Measuring the Harmonics of Electroconvection in Liquid Crystals with Optical Methods

**By**
**Ryan J. Cardman**
**Department of Physics**
**Allegheny College**
**Meadville, Pennsylvania**

**April, 2017**

# Measuring the Harmonics of Electroconvection in Liquid Crystals with Optical Methods

**By**
**Ryan J. Cardman**
**Department of Physics**
**Allegheny College**
**Meadville, Pennsylvania**

**April, 2017**

**Submitted in fulfillment of the senior thesis requirements of the**
**Department of Physics at Allegheny College**
**and approved by the senior thesis committee.**

| | | | |
|---|---|---|---|
| _____ | _____ | _____ | _____ |
| **Dr. David Statman** | **Date** | **Dr. Doros Petasis** | **Date** |

_____

**Pledge**

**Table of Contents**

Acknowledgements……vii

Abstract……...ix

Introduction……..1

Theory……10

*Standard Model (SM) of Electroconvection*……..10

*Beam Propagation through Sample*……...15

*Flexoelectric Effects*……...19

Methodology……..20

Results & Analysis…….27

Conclusion & Discussion……...39

References……..41

Appendix……42

*Lagrange Multipliers*…….43

*Measuring the thickness* d *of Sample*…….46

*Spectral Leakage*……47

*Laser Diffraction Results on Cell C*……...49

*Laser Diffraction Results on Cell A (Rectangular Windowed)*……..66

*Laser Diffraction Results on Cell A (Hann Windowed)*……71

*Laser Diffraction Results on Cell A (Second Trial) (Hann Windowed)*……....76

*Second-Order Diffraction Fringes (Time Domain)*……...83

*Laser Diffraction Results on Central Fringe of Cell A (Hann Windowed)*……...84

*Additional Results for the $I_{-4}$ Fringe*……..88

**Acknowledgements**

I primarily would like to thank the two readers of my thesis, Dr. Statman and Dr. Petasis. While a hands-off professor, Dr. Statman always prodded me with helpful advice and words of encouragement while setting up and executing my experiment. Dr. Petasis afforded me the opportunity to work in his EPR lab and bring a spectrometer back from the dead; during that project, I appreciated the electronic complexity of the machinery needed to make precise Landé g-factor measurements. Additionally, I would like to thank both professors for recommending me for graduate school.

I would like to also thank Rob for his assistance in providing me with fully-functioning electronic devices and purchasing the parts needed for my experiment. Additionally, I want to thank my friends in SPS for creating a thoughtful and welcoming environment to study physics.

My undergraduate research was not constrained to AMO and condensed matter topics; during my REU at Indiana University, where I worked with Matt Shepherd on a nuclear physics project, I gained exposure to the methods (both experimental and computational) routinely used in that field. I also want to thank Matt for recommending me for graduate school.

My family has always been supportive throughout my education. It has always been their goal to provide me with the best possible education, and I want to thank them for that. They were extremely helpful in helping me choose the best undergraduate and graduate school options. While raising me, they continuously fostered my interest in science with a loving atmosphere.

I would like to close these acknowledgements with a quote from Charles H. Townes, a physicist who inspired me to undertake this field: “Science is exploration. The fundamental nature of exploration is that we don’t know what’s there. We can guess and hope and aim to find out certain things, but we have to expect surprises.”

Name: Ryan J. Cardman Date: Spring, 2017

Major: Physics
Thesis Committee: Dr. David Statman, Dr. Doros Petasis

Title: Measuring the Harmonics of Electroconvection in Liquid Crystals with Optical Methods

---

When driven under a sinusoidal electric field of a set fundamental frequency, the director field of a nematic liquid crystal (NLC) is influenced by restoring torques, electric torques, and viscous torques such that their imbalance induces a molecular flow pattern of convecting rolls known as electroconvection. In the standard model (SM) solution describing the velocity components and director distortion angle ($\theta$), the temporal response of these variables were originally predicted to prohibit linear combinations of odd and even harmonics. However, the inclusion of the flexoelectric polarization vector, which arises when the molecules align in a splay or bend formation, allows a linear combination of odd and even-harmonic temporal solutions. This project studies the nonlinear temporal response to an ac driving field of the NLC N-(4-methoxybenzylidene)-4-butylaniline (MBBA), which is situated within two glass electrodes spaced at ~20μm, coated with indium tin oxide (ITO), and rubbed with polyimide coating. When electroconvection is reached, the rolls produce a diffraction grating that scatters a helium-neon (He-Ne) laser beam linearly polarized in the rubbing direction. The intensity of a diffraction fringe, detected by a photodiode, depends on the same harmonics that $\theta$ does. Therefore, fast Fourier-transforms (FFTs) from the time to frequency domains were conducted on intensity signals, where both odd and even harmonics were detected when the NLC was driven at 10-200Hz frequencies.

# 1 Introduction

Liquid crystals (LCs) have a growing presence in modern technology for their ability to manipulate the light that is incident upon them with one example being how they can elliptically polarize a linearly polarized incident beam. These substances exist between the solid and liquid phase of matter in which aligned lattices of the molecules are able to flow past each other [1]. The direction that is most energetically favorable for the molecules to align is represented by a unit vector $\hat{n}$ known as the director[2,3]. In the case of this experiment, the director is represented by molecules which align in a definite direction but not a definite position, i.e., nematics (shown in Fig.1) [1,3]. Furthermore, the electric and magnetic properties of liquid crystals behave in ways that give rise to unusual pattern formations, with one of them being electroconvection, where a row of rolls, formed by the flowing molecules, produces a diffraction grating within the sample.

**Director Alignment of Nematic Liquid Crystal**

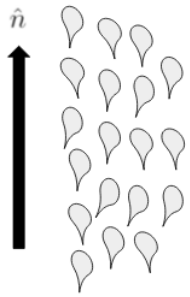


**Figure 1.** Nematic liquid crystal molecules are not fixed in position, just direction denoted by the director $\hat{n}$, so they are free to flow past each other [3]; here, the molecules are tear-shaped.

In order to understand electorocnvection, shown in Fig. 2, one must realize how liquid crystals behave in the presence of external electric and magnetic fields. In an ordinary liquid, the dielectric permittivity of the material $\epsilon$ would remain the same in all directions, i.e., along its length, width, and height. However, liquid crystals exhibit anisotropy, i.e., $\epsilon$, the magnetic susceptibility, $\chi$, the conductivity, $\sigma$, and, in some instances, [4], the mobility, $\mu$, exhibit the following general form,

$$c_a = c_{\parallel} - c_{\perp} \neq 0, \tag{1}$$

where the subscript $a$ denotes anisotropy, $c$ is a property, $\parallel$ is the direction parallel to $\hat{n}$, and $\perp$ is the direction perpendicular to $\hat{n}$ [3,4,5,6]. In my study, the mobility and magnetic susceptibility may be

neglected. It is assumed that the dielectric anisotropy is negative and the conductive anisotropy is positive for the LC used. These parameters explain electroconvective pattern formation, via Gauss's law and the continuity equation, respectively,

$$\nabla \cdot \mathbf{D} = \nabla \cdot [\epsilon_0 \epsilon_\perp \mathbf{E} + \epsilon_0 \epsilon_a (\hat{n} \cdot \mathbf{E}) \hat{n}] = \rho_{el} \tag{2}$$

$$\nabla \cdot \mathbf{J} = \nabla \cdot [\sigma_\perp \mathbf{E} + \sigma_a (\hat{n} \cdot \mathbf{E}) \hat{n} + \rho_{el} \mathbf{v}] = -\partial_t \rho_{el}, \tag{3}$$

where $\mathbf{D}$ and $\mathbf{J}$ are the respective electric displacement and current density vectors, $\mathbf{E}$ is the electric field within the sample, $\rho_{el}$ is the charge density given by ionic impurities moving along the director and focusing in certain regions along the $x$-axis, and $\mathbf{v}$ is the fluid velocity of the ionic impurities [1,3,5,6].

**Schematic of Liquid Crystal Sample**

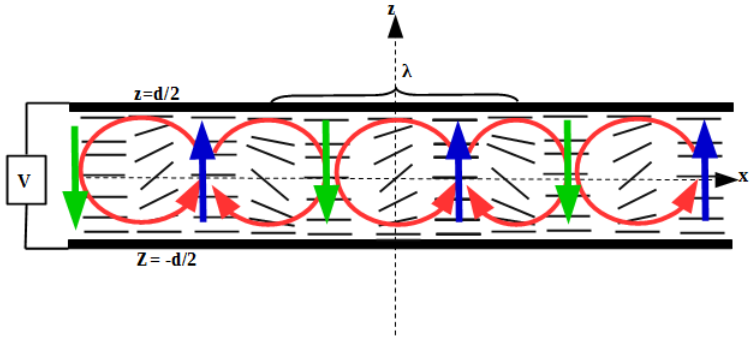


**Figure 2.** An ac electric field $\mathbf{E}_0$ is applied in the $z$-direction by the electrodes containing the sample and separated by a distance $d$. This induces the rolling molecular flow and the focusing of ions between each roll that exert a viscous torque on the director due to the electrostatic attraction to the electrodes, as shown by the green and blue arrows. Here, $\lambda$ is the wavelength associated with the striped pattern of rolls that would be viewed on the $xy$-plane [3].

Condensed matter theorists Carr and Helfrich [7] proposed a one-dimensional mechanism that explains how this molecular rolling comes into play. They assumed three torques acting on the director $\hat{n}$: an elastic restoring torque due to director distortions, $\mathbf{\Gamma_d}$, an electric torque due to an external electric field, $\mathbf{\Gamma_e}$, and a viscous torque, $\mathbf{\Gamma_v}$, due to the Coulomb force acting on the regions of charge

density [3,5]. The director remains undistorted if, for the net torque $\mathbf{\Gamma_{net}}$,

$$\mathbf{\Gamma_{net}} = \mathbf{\Gamma_d} + \mathbf{\Gamma_e} + \mathbf{\Gamma_v} = \mathbf{0}, \quad (4)$$

and the molecular field, which is a minimization of the free energy density with respect to director orientation, $\mathbf{H}$ aligns in the same direction as the director [3,5,6]. However, if an appreciable potential difference ($V_d$) is applied across the electrodes of the sample, Eq.4 becomes unbalanced, a Fréedericks transition occurs, and the patterns shown in Fig. 3 and Fig.4, known as Williams domains, form [3,5]. A three-dimensional model, using the same initial equations as Helfrich (i.e., Gauss's law, continuity equation, Navier-Stokes, and director torque balance), known as the standard model (SM), has been developed. The SM is derived from Eq.2, Eq.3, Eq.4, and the general Navier-Stokes equation,

$$\rho\big[\partial_t \mathbf{v} + (\mathbf{v}\cdot\nabla)\mathbf{v}\big] = -\nabla p + \eta\nabla^2\mathbf{v} + \rho_{el}\mathbf{E}, \quad (5)$$

where $\rho$ is the density of the liquid crystal, $\mathbf{v}$ is the velocity of the fluid flow, and $\eta$ is the Miesowicz viscosity coefficient [3,5]. The left-hand side of the equation describes the force density and, therefore, acceleration of the fluid, while the first two terms on the right-hand side are equivalent to the divergence of the stress tensor (the quantity that explains how the liquid crystal responds to deformations) [3]. The third term is the Coulomb force acting on the regions of charge density. These equations were rewritten in the form of a system of six, coupled partial differential equations [5]. The solution that describes the director distortion angle, $\theta$, the $x$, $y$, and $z$-velocity components, $v_x$, $v_y$, $v_z$, and the azimuthal director distortion angle, $\psi$, have temporal dependencies that may be neatly expanded into a Fourier series with director distortions having two modes of oscillation, one that is expanded only by odd harmonics and one by even harmonics [3,5,6,8,9].

**Williams Domains**

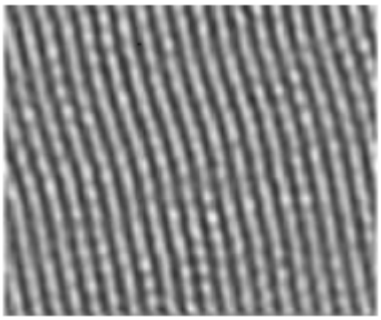

**Figure 3.** The striped patterns shown from the $xy$-plane of the sample are known as Williams domains [3].

These solutions have physical meaning to them. In the solution of even harmonics, the director distortion angle has the following time dependence

$$\theta(t) = A + B\sin(2\omega t) + ..., \tag{6}$$

with the constants $A$ and $B$ and the frequency of the external ac electric field, $\omega$; however, for the odd harmonics, we see that,

$$\theta(t) = C\sin(\omega t) + D\sin(3\omega t) + ..., \tag{7}$$

with the constants $C$ and $D$ [8]. Usually, $A$ and $C$ are much larger than $B$ and $D$, which means that the director distortion angle may either primarily be a constant value or oscillate with the frequency of the applied electric field. It turns out that external electric fields with frequencies below a cutoff ($\omega_C$), follow the even-harmonic distortion[3,5,6,8]. This is known as the "conduction" regime because the regions of charge density depend upon the fundamental harmonic[3,5,6,8]; likewise, driving frequencies above $\omega_c$ follow the "dielectric" regime, as the director is distorted with dependence on the fundamental harmonic (the dielectric permittivity must come into play for this)[3,5,6,8]. A figure exhibiting the two regimes is shown in Fig. 4.

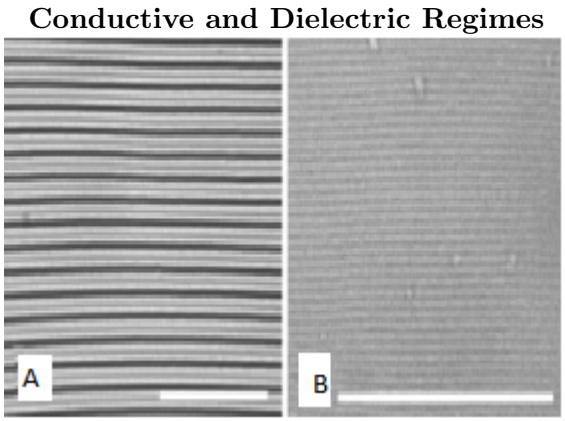


**Figure 4.** A liquid crystal under the conductive regime is shown in (A), while the dielectric regime is shown in (B) [9].

Optical experiments have been conducted to study the accuracy of the SM [2,3,4,6,8,9,10,11]. The birefringent properties of liquid crystals allow patterns to be seen. Birefringence occurs when the liquid crystal exhibits two different indices of refraction parallel (extraordinary index $n_e$) and perpendicular (ordinary index $n_o$) to the optical axis (the axis of the director) [10,12], with an effective refractive index, $n_{eff}$, given by

$$\frac{1}{n_{eff}^2} = \frac{\sin^2\tilde{\beta}}{n_o^2} + \frac{\cos^2\tilde{\beta}}{n_e^2}, \tag{8}$$

where $\pi/2 - \tilde{\beta}$ is the angle between the optical axis of the director and the wave vector, which is dependent on the director distortion angle, as shown in Fig.5 [9]. This leads to the simplification,

$$n_{eff} = \frac{n_o n_e}{\sqrt{n_o^2\cos^2\tilde{\beta} + n_e^2\sin^2\tilde{\beta}}}. \tag{9}$$

When Fermat's principle is taken into acount, the shortest path length traveled by the light rays is exhibited in Fig.6 [3,9,13,14]. Optical ray tracing shows that the incident light on the sample will illuminate the positions of the Williams domains (the rolls). This method of viewing electroconvection is known as the shadowgraph method, where a charge-coupled device (CCD) camera can photograph these patterns under a microscope [2,3].

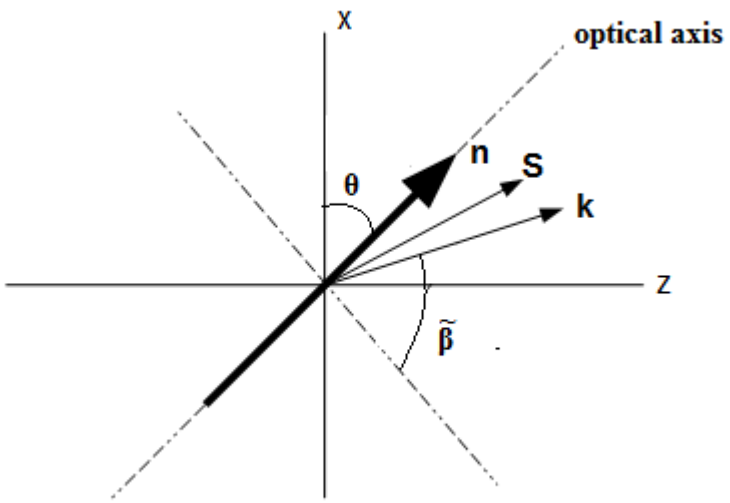


**Figure 5.** The effective refractive index depends upon the angle between the wave vector $\vec{k}$ and the director. The Poynting vector $\vec{S}$ is not assumed to have the same direction as the wave vector as it conventionally does [9].

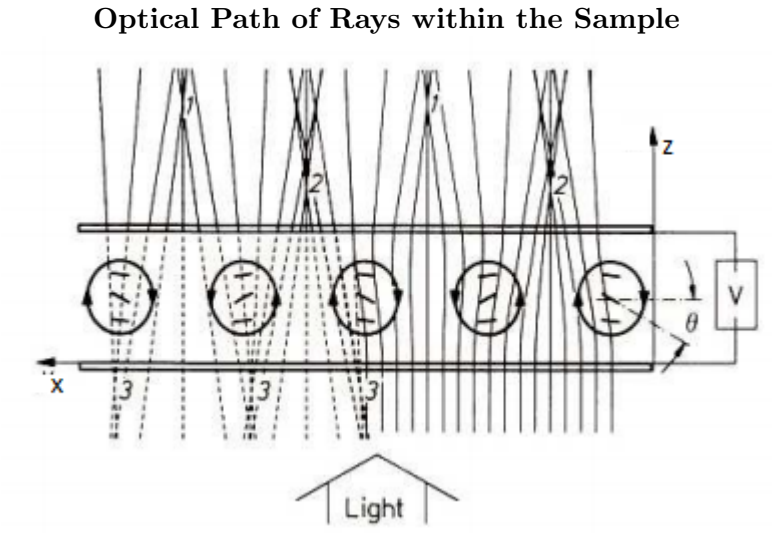


**Figure 6.** Proper calculations of Fermat's principle via the Euler-Lagrange equations yield the following path for light rays, converging at 1 and 2; tracing these rays back will produce the effect of the Williams domains being illuminated when viewed under a microscope (i.e., they converge at 3) [3].

This method has been particularly useful in the experiments of Dennin [2,4,10], where the striped

patterns of the Williams domains on the $xy$-plane of the sample through the shadowgraph method were described by wave functions with the momentum transfer vector of scattered light $\mathbf{k}$,

$$A(\mathbf{x})\cos\left(\mathbf{k}\cdot\mathbf{x}+\phi\right), \tag{10}$$

where $A$ is the maximum amplitude of the stripes shown in the CCD image, $\mathbf{x}$ is the $x$-poisition in the photograph, and $\phi$ is a phase difference within the wave [2]. In one experiment, it was shown that the Williams domains can propagate at an angle $\Theta$ from the original director alignment in a pattern of electroconvection known as oblique or "zig" and "zag" rolls [2]. The magnitudes of the wave vectors were determined by taking a Fourier transform of the photograph from a spatial domain to $k$-space, i.e., performing the following transformation,

$$\frac{1}{\sqrt{2\pi}}\int_{\text{all space}} A(\mathbf{x})\cos\left(\mathbf{k}\cdot\mathbf{x}+\phi\right)e^{-i\mathbf{k}\cdot\mathbf{x}}d\mathbf{x}. \tag{11}$$

It turns out that summing the product of the amplitude of the striped pattern with the factor $e^{-i\mathbf{k}\cdot\mathbf{x}}$ at every position, and scaling it by $\sqrt{2\pi}$, results in the amplitude of the pattern as a function of the wave number (directly proportional to momentum). From there, it is evident what wave numbers are associated with the domains. Perhaps the most remarkable finding from these studies was the discovery that these domains can travel in time with a frequency known as the Hopf frequency $\omega_H$ [2,4]. Instances like these showed that the SM was not quite complete; an extra anisotropy known as the ionic mobility anisotropy had to be introduced into the equations [2,4]. One image of the patterns discovered, along with its Fourier transform, is shown in Fig.7.

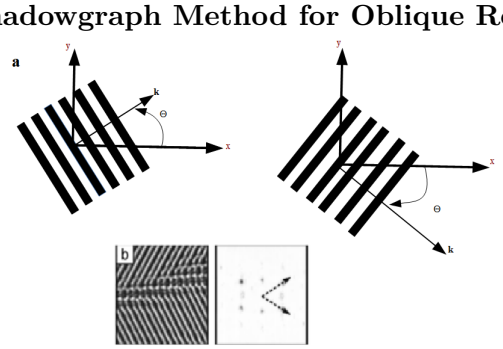


**Figure 7.** Rolls may follow the "zig" ($\Theta > 0$) or "zag" ($\Theta < 0$) oblique patterns when viewed from the

$xy$-plane, where the wavevector of the striped pattern is given by **k** [2]. The shadowgraph method is shown in (b) with the Fourier transform into $k$-space shown on the right [2].

An alternative method of viewing patterns that has not been as widely used as the shadowgraph method is He-Ne laser diffraction. When considering the diffraction of monochromatic light, one finds through the integration of the effective refractive index over the thickness of the sample ($d$) that there is a phase difference in the electric field $\Delta\phi$ given by

$$\Delta\phi = -kn_e d\frac{n_e^2 - n_o^2}{8n_o^2}\theta(t)^2\cos(2k_x x), \tag{12}$$

where $k$ is the wave number associated with the He-Ne laser and $k_x$ is the wave number associated with the x-direction of fluid flow [9,14,15]. When the optical field of the laser is integrated over an entire circular area for an n-th order fringe, for small director distortion angles, the intensity of the fringe over the intensity of the central maximum $I_n/I_0$ is given by the $J_{n/2}^2$ Bessel function. This results in the following proportions:

$$I_1/I_0 \propto \theta(t)^2 \tag{13}$$

$$I_2/I_0 \propto \theta(t)^4, \tag{14}$$

where $I_1$ is the intensity of the first-order diffraction fringe and $I_2$ is the intensity of the second-order fringe, both of which have been experimentally confirmed [8,9].

The results of experiments conducted by Buka and experiments done at Allegheny have possibly found evidence supporting another correction to the SM known as flexoelectricity [6,7]. Intensity versus time curves, shown in Fig. 8, have exhibited the patterns of curves that indicate the combination of an odd and even harmonic in the Fourier expansion for the director distortion angle.

In order to fully understand what flexoelectricity is, one must know the various distortions that directors may go through: splay, twist, and bend. To fully conceptualize these distortions, use the following example of a giant rubber, rectangular eraser. A twist to the top of the eraser from the bottom is known as a twist and is associated with an elastic force constant known as $K_{22}$ [3,16]. If one were to pinch the width of the eraser so that the unpinched end splays outward, one would be performing a splay deformation, associated with the constant $K_{11}$ [3,6,16]. And if one were to pinch

the length of the eraser so that the top bends down towards the bottom, one would be performing a bend associated with the constant $K_{33}$ [3,6,16]. These deformations, shown in Fig.9, give rise to the Frank-Oseen elastic free energy, $F_d$

$$F_d = \frac{1}{2}K_{11}|\nabla \cdot \hat{n}|^2 + \frac{1}{2}K_{22}|\hat{n} \cdot \nabla \times \hat{n}|^2 + \frac{1}{2}K_{33}|\hat{n} \times \nabla \times \hat{n}|^2, \tag{15}$$

where this expression gives rise to the director distortion torque, $\mathbf{\Gamma_d}$ [3,5]. For flexoelectricity, the splay and bend deformations contribute to a polarization $\mathbf{P}$ denoted by

$$\mathbf{P} = e_1\hat{n}(\nabla \cdot \hat{n}) + e_3(\hat{n} \cdot \nabla)\hat{n}, \tag{16}$$

where $e_1$ and $e_3$ are the flexocoefficeints, respectively associated with splay and bend deformations [3,8,16]. Including this in the electric displacement of Eq.2 results an a more difficult set of solutions to the SM, with the combination of odd and even harmonics being one of them [6,8]. Experimentally, flexoelectricity has been observed in liquid crystals with both negative conductive and dielectric anisotropies, as well as ones subject to an external field with both ac and dc components [6,11].

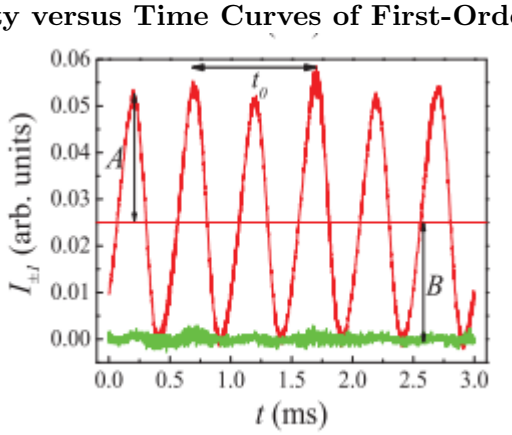


**Figure 8.** This graph was obtained by placing a photodetector on the first order fringe in a liquid crystal diffraction experiment; the shape is a superposition of the first and second harmonic, which can be explained by electroconvection [6,8]. Here $t_0$ is the period of the ac voltage.

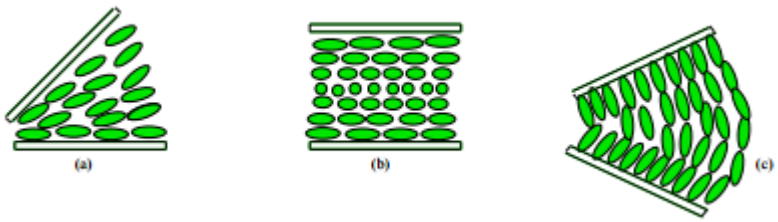


**Figure 9.** Examples of the (a) splay, (b) twist, and (c) bend deformations on liquid crystal directors [3].

However, flexoelectricity may not be the only culprit to the former unusual patterns observed. In order to go through with this prediction, I also want to make sure that the time patterns we have been seeing are not the results of the heterodyned (multiplied) signals of a wave of red and blue Doppler-shifted He-Ne laser light [17]. The shifting could occur from the molecular flow induced within the sample and result in a beat frequency that arises when the blue Doppler-shifted wave is multiplied by the red Doppler-shifted wave. Therefore, we could be observing a harmonic that has to do with the shifting of the incident laser and not the harmonics of the director distortion angles.

This experiment sets out to study the intensity versus time and frequency domains in the fringes of a diffracted He-Ne laser in order to identify the harmonics of the distorted director field. The harmonics are to be identified via He-Ne laser diffraction at low frequencies of the applied ac field ($\leq$200Hz). It is expected that harmonics compatible with the extension to the SM are to be observed, i.e., combinations of odd and even harmonics, which is explained by flexoelectric effects [6]. Furthermore, it is desired to investigate the harmonic dependence on the driving frequency of the external electric field.

# 2 Theory

## 2.1 Standard Model (SM) of Electroconvection

Consider a nematic liquid crystal (LC), shown in Fig. 5, with a dielectric anisotropy that is negative ($\epsilon_a = \epsilon_\parallel - \epsilon_\perp < 0$), with $\epsilon_\parallel$ and $\epsilon_\perp$ being the dielectric constants parallel and perpendicular to the director, $\hat{n}$, respectively. The nematic LC is sandwiched between two glass electrodes with an ac electric

field applied across it. The electric displacement can therefore be written as

$$\mathbf{D} = \epsilon_0 \epsilon_\perp \mathbf{E} + \epsilon_0 \epsilon_a (\hat{n} \cdot \mathbf{E}) \hat{n}. \tag{17}$$

The electric energy density brought on by the electric displacement $\mathbf{D}$ is

$$F_e = -\frac{1}{2}(\mathbf{D} \cdot \mathbf{E}) = -\frac{1}{2}[\epsilon_0 \epsilon_\perp E^2 + \epsilon_0 \epsilon_a (\hat{n} \cdot \mathbf{E})^2] \tag{18}$$

where the first term goes to zero when the functional derivative is taken on it. Thus, this energy density is added to the Frank-Oseen free energy density, which is analogous to the elastic potential energy brought on by displacements for a mass attached to a spring, is

$$F_d = \frac{1}{2} K_{11} |\nabla \cdot \hat{n}|^2 + \frac{1}{2} K_{22} |\hat{n} \cdot \nabla \times \hat{n}|^2 + \frac{1}{2} K_{33} |\hat{n} \times \nabla \times \hat{n}|^2, \tag{19}$$

where $K_{11}$, $K_{22}$, and $K_{33}$ are elastic energy density constants corresponding to splaying, twisting, and bending of the director field [5].

In a mass attached to a spring that is oscillating along the $x$-axis, the distortion from equilibrium is given by

$$\mathbf{x} - \mathbf{x}_0, \tag{20}$$

where $\mathbf{x}_0$ is the equilibrium position of the mass and $\mathbf{x}$ is the position of the mass. This leads to an elastic potential energy of

$$\frac{1}{2} k |\mathbf{x} - \mathbf{x}_0|^2, \tag{21}$$

where $k$ is the force constant of the spring. LC directors can be thought of as behaving in the same way, where the magnitude of splay from its equilibrium position can be measured by how much a field of directors would diverge after the distortion. Hence, the distortion is given by the divergence of the director field. Similarly, the magnitude of twisting is determined by how much a director curls about an axis perpendicular to the rubbing direction (the direction of an undistorted $\hat{n}$) with the amount of bending determined by the curling of the directors about an axis parallel to the rubbing direction. Through the right-hand rule, one may arrive at the expressions for director distortions for twisting and bending.

The total free energy density in the presence of an electric field can then be written as

$$F = \frac{1}{2}K_{11}|\nabla \cdot \hat{n}|^2 + \frac{1}{2}K_{22}|\hat{n} \cdot \nabla \times \hat{n}|^2 + \frac{1}{2}K_{33}|\hat{n} \times \nabla \times \hat{n}|^2 - \frac{1}{2}\epsilon_0\epsilon_a(\hat{n} \cdot \mathbf{E})^2, \tag{22}$$

where the molecular field due to this free energy $\mathbf{H}$ is given by the functional derivative of the free energy ($\mathcal{F} = \int F d\tau$, where $d\tau$ is a volume element). In physics, fields (e.g. electric) tend to be the result of differentiation of some energy potential with respect to position. In this case, the field is the molecular field, and the potential is the free energy. Thus, using Einstein's summation convention,

$$H^i = -\frac{\delta \mathcal{F}}{\delta n_i} = \partial_{n_i} F - \partial_{r_j}\partial_{n_i^j} F, \tag{23}$$

where $r_j$ denotes the three directions ($x$,$y$, and $z$), $n_i$ gives the components of the director field, and $n_i^j$ is given by

$$n_i^j = \partial_{r_j} n_i. \tag{24}$$

The net torque on the director field can be given by the cross product of $\hat{n}$ and $\mathbf{H}$. For an explanation of Euler-Lagrange equations, see Section 0.1 of the Appendix. When the net torque on the system is zero, the molecular field aligns with the director field. However, regions of charge density $\rho_{el}$ brought on by the anisotropy in conductivity will experience an electrostatic force from one electrode to another given by $\rho_{el}\mathbf{E}$. This results in a viscous fluid torque against the torques brought on by the electric force and elastic restoring forces. That torque is given by

$$-\hat{n} \times (\gamma_1 \mathbf{N} + \gamma_2 \mathbf{A}\hat{n}), \tag{25}$$

where $\gamma_1 = \alpha_3 - \alpha_2$ and $\gamma_2 = \alpha_3 + \alpha_2$ are viscosity coefficients corresponding to the director rotating, with $\alpha_2$ and $\alpha_3$ being viscosity coefficients corresponding to a shear force applied to the LC [5]. The tensor $\mathbf{A}$ is the $3 \times 3$ symmetric strain rate tensor while $\mathbf{N}$ is the rate of change in the director with respect to the fluid motion [5]. The strain rate tensor measures the rate of the volume of the fluid deforming. And so, in order for no pattern to form, the net torque ($\vec{\Gamma}$) on the director must satisfy the following condition:

$$\vec{\Gamma} = -\hat{n} \times \left[\frac{\mathcal{F}}{\delta \hat{n}} + (\gamma_1 \mathbf{N} + \gamma_2 \mathbf{A}\hat{n})\right] = \mathbf{0}. \tag{26}$$

We can use Newton's Second Law to find the net force density on the LC in the $i$-th direction, i.e.,

$$\rho \frac{dv_i}{dt} = \rho_{el} E_i + \partial_{r_j} T_{ij}, \tag{27}$$

where $T_{ij}$ is the $ij$-th component of the stress tensor, i.e., the tensor that describes the force per area throughout the LC, $v_i$ is the $i$-th component of the fluid velocity, and $\rho$ is the density of the LC [5]. This second term on the right-hand side dimensionally makes sense because differentiation with respect to position of a quantity with dimensions of force per area will result in a quantity with dimensions of force per volume.

We must also consider the condition that the LC is incompressible, i.e.,

$$\nabla \cdot \mathbf{v} = 0, \tag{28}$$

where $\mathbf{v}$ is the velocity of the molecular flow. Furthermore, we consider Gauss's law for the electric displacement and the continuity equation, i.e.,

$$\nabla \cdot \mathbf{D} = \nabla \cdot [\epsilon_0 \epsilon_\perp \mathbf{E} + \epsilon_0 \epsilon_a (\hat{n} \cdot \mathbf{E}) \hat{n}] = \rho_{el} \tag{29}$$

$$\nabla \cdot \mathbf{J} = \nabla \cdot [\sigma_\perp \mathbf{E} + \sigma_a (\hat{n} \cdot \mathbf{E}) \hat{n} + \rho_{el} \mathbf{v}] = -\partial_t \rho_{el}, \tag{30}$$

where $\mathbf{J}$ is the current density and $\sigma_a$ is the anisotropy in conductivity. The potential of the external electric field ($\mathbf{E}_0$) applied in the z-direction is given by

$$\sqrt{2} V_{rms} \cos(\omega t), \tag{31}$$

where $V_{rms}$ is the rms-voltage of the ac field and $\omega$ is its angular frequency. Because we take the curl of the vector that the components in Eq. 27 form to get our system of equations, we may introduce an electric potential $f$ such that, within the LC sample,

$$\mathbf{E} = \mathbf{E}_0 - \nabla f, \tag{32}$$

where $\mathbf{E}$ is the total field within the cell. At the electrodes, i.e., at $z = d/2$, $f = 0$.

Eq. 26-30 can be written in the form of a $6 \times 6$ differential operator $\mathbf{B}$ such that

$$\mathbf{Bu} = \mathbf{0}, \tag{33}$$

where $\mathbf{u}$ is a $6 \times 1$ matrix of variables that describe the dynamics of the electroconvective rolls, i.e.,

$$\mathbf{u} = \begin{bmatrix} f \\ \theta \\ \psi \\ v_x \\ v_y \\ v_z \end{bmatrix},$$

where $v_x$, $v_y$, and $v_z$ are the $x$, $y$, and $z$-th components of the velocity field for the moving ions within the LC while $\psi$ is the azimuthal distortion angle (angle from the $x$-axis to the $y$-axis) [5]. We are concerned about the solution to $\theta$, as that will affect the intensity curves of the diffracted fringes and contribute to a phase shift in the optical field. We want to find a separable spatiotemporal solution; i.e., a spatial ($\theta_s(x, y, z)$) solution, as well as a temporal solution $\theta_t$. When considering normal rolls, the amplitude of $\theta$ contributes to a periodic pattern of bright and dark stripes when the $xy$-plane is viewed. This pattern has a wavelength of $2d$ making the wave number in the $x$-direction ($k_x$) become

$$k_x = \frac{2\pi}{2d} = \frac{\pi}{d}. \tag{35}$$

And so, this pattern of stripes can be represented by a sinusoidal wave, i.e.,

$$\theta = \theta_t(t)\theta_s(z)\cos(k_x x). \tag{36}$$

Because the polyimide coating on the electrodes exerts such a strong anchoring force on the directors at $z = \pm d/2$, $\theta = 0$. We notice from Fig. 2 that the director distortion along the z-axis starts at 0 at the electrodes and reaches a maximum at $z = 0$, much like a cosine wave from $-\pi/2$ to $\pi/2$. Thus, $\theta_s(z)$ can be expressed cosine wave between the electrodes, the points at which $k_z(d/2) = \pi/2$. By

solving for $k_z$, the wave number associated with the periodic spatial solution along the $z$-axis, we find that

$$k_z = \pi/d. \tag{37}$$

In order to solve for the temporal solution, we assume the following series solution:

$$\theta_t(t) = e^{\zeta t}\Sigma_n\Big[A_n e^{in\omega t}\Big], \tag{38}$$

where $\zeta$ is known as the Floquet exponent that describes how rapidly the harmonics grow and decay [5]. When Eq. 38 is placed in Eq. 33, the even and odd harmonics cannot be added together to solve the equation. Thus, there are two sets of solutions to the equation: those for the conduction regime (even) and those for the dielectric regime (odd). This means that, for the conduction regime,

$$\theta_t = e^{\zeta t}\Sigma_{n=0}^{\infty}\Big[A_{2n} e^{i2n\omega t}\Big] = A + B\sin(2\omega t) + ..., \tag{39}$$

and for the dielectric regime,

$$\theta_t = e^{\zeta t}\Sigma_{n=0}^{\infty}\Big[A_{2n+1} e^{i(2n+1)\omega t}\Big] = C\sin(\omega t) + D\sin(3\omega t) + ..., \tag{40}$$

where $A$,$B$,$C$, and $D$ are constants. And so, the solution for the director distortion angle from the $x$-axis to $z$-axis is given by

$$\theta(x, z, t) = \theta_t \cos(k_x x)\cos(k_z z). \tag{41}$$

## 2.2 Beam Propagation through Sample

Consider a ray of light propagating through a cell of a nematic LC sandwiched between indium tin oxide (ITO) coated glass slides. When a ray of light propagates throughout the sample (with wave vector $\mathbf{k}$), the components of its velocity can be broken into two. In this experiment, the basis associated with the wave vector will consist of a unit vector along the optical axis of the director (parallel to director n) and one perpendicular to it, as shown in Fig. 5. Hence, the speed of light in a vacuum ($c$) is written in terms of these components as

$$c^2 = c^2\cos^2(\tilde{\beta}) + c^2\sin^2(\tilde{\beta}), \tag{42}$$

where $\tilde{\beta}$ angle above the normal to the optical axis. The component in which the wave vector is perpendicular (and optical field $\tilde{\mathbf{E}}$ is parallel) to the optical axis is known as the extraordinary ray, with the component along the optical axis being the ordinary ray [12].

When light passes through a material, it moves at a speed reduced by tits refractive index $n$. Hence, the speed of light within that material is given by

$$\frac{c}{n} \tag{43}$$

LCs are uniaxially birefringent materials, meaning that $n$ will be different for the ordinary and extraordinary rays. The refractive indices for the extraordinary and ordinary rays, respectively, are $n_e$ and $n_o$. And so, since $c\cos(\tilde{\beta})$ and $c\sin(\tilde{\beta})$ are the respective speeds of the extraordinary and ordinary rays in a vacuum, their corresponding speeds within a uniaxially birefringent material are

$$\frac{c\cos(\tilde{\beta})}{n_e} \tag{44}$$

$$\frac{c\sin(\tilde{\beta})}{n_o}. \tag{45}$$

Subsequently, the effective speed (with refractive index $n_{eff}$) of the beam within the LC is related to the speeds of the components by

$$\frac{c^2}{n_{eff}^2} = \frac{c^2\cos^2(\tilde{\beta})}{n_e^2} + \frac{c^2\sin^2(\tilde{\beta})}{n_o^2}. \tag{46}$$

After factoring and canceling the speed of light on both sides, it can be shown that

$$\frac{1}{n_{eff}^2} = \frac{\cos^2(\tilde{\beta})}{n_e^2} + \frac{\sin^2(\tilde{\beta})}{n_o^2}. \tag{47}$$

Eq. 47 is a reciprocal sum, much like the sum of capacitors in series. Therefore, this equation can be simplified to

$$n_{eff}^2 = \left(\frac{n_e^2}{\cos^2(\tilde{\beta})}\right)\left(\frac{n_o^2}{\sin^2(\tilde{\beta})}\right)\left(\frac{n_e^2}{\cos^2(\tilde{\beta})} + \frac{n_o^2}{\sin^2(\tilde{\beta})}\right)^{-1}. \tag{48}$$

When the $\cos^2(\tilde{\beta})\sin^2(\tilde{\beta})$ term is distributed into the denominator and the square root is taken,

$$n_{eff} = \frac{n_o n_e}{\sqrt{n_e^2\sin^2(\tilde{\beta}) + n_o^2\cos^2(\tilde{\beta})}}. \tag{49}$$

When the laser beam of wave number $k$ passes through a material of refractive index $n$ and thickness $d$, it takes on a phase shift $\phi$ given by $knd$. However, if this refractive index fluctuates with respect to the axis along the thickness (the z-axis), $\phi$ must be written as

$$\phi = k \int_{-d/2}^{d/2} n dz. \tag{50}$$

In the case of the beam passing through a liquid crystal sample with $n_{eff}$ in the z-direction, as shown in Fig. 6,

$$\phi = k \int_{-d/2}^{d/2} n_{eff} dz. \tag{51}$$

The angle above the ordinary axis, $\tilde{\beta}$ has the same general solution and time dependence as the director distortion angle $\theta$ [9], i.e.,

$$\tilde{\beta} = \theta_t \cos(k_x x) \cos(k_z z). \tag{52}$$

We consider that $\tilde{\beta}$ is a small oscillation in order to approximate $n_{eff}$ to the second order by means of a Maclaurin expansion, as done in previous analyses [9,15]. And so,

$$n_{eff} \approx n_e - \frac{\tilde{\beta}^2 n_e (n_e^2 - n_o^2)}{2n_o^2}, \tag{53}$$

and because

$$\tilde{\beta}^2 = \theta_t^2 \cos^2(k_x x) \cos^2(k_z z) = \theta_t^2 \left[\frac{1}{2} + \frac{1}{2}\cos(2k_x x)\right]\left[\frac{1}{2} + \frac{1}{2}\cos(2k_z z)\right], \tag{54}$$

we can discard the product $\frac{\theta_t^2}{4}$, which results in a phase that is constant in position and, therefore, does not give rise to a diffraction pattern. Furthermore, we can discard the product $\frac{\theta_t^2 \cos(2k_z z)}{4}$ as that term will vanish under the integral [9]. Thus, the approximation, under the integral, can be written as

$$\phi(x) = k \int_{-d/2}^{d/2} dz \left[n_e - \frac{\theta_t^2 \cos(2k_x x) n_e (n_e^2 - n_o^2)}{8n_o^2}\right] = k n_e d + \Delta\phi(x), \tag{55}$$

where

$$\Delta\phi(x) = -\frac{n_e (n_e^2 - n_o^2) d}{8n_o^2} \theta_t^2 \cos(2k_x x), \tag{56}$$

with

$$\Delta\phi_{\max} = -\frac{n_e(n_e^2 - n_o^2)d}{8n_o^2}\theta_t^2 \tag{57}$$

being the maximum amplitude of the phase with respect to the $x$ position in the grating pattern. This result is significant, as it will contribute to the mathematical description of the diffraction pattern resulting from the electroconvective rolls. This result will soon show that the temporal solution to the SM for the director distortion angle ($\theta_t^2$) of a diffracted beam has an impact on the intensities of the maxima in the pattern.

Consider Fig. 10 of the diffraction pattern shown below. The path difference ($\Delta r$) of a ray of light diffracted by the grating at an angle $\alpha$ from the fundamental maximum can be written as

$$\Delta r(\alpha) = x \sin\alpha, \tag{58}$$

where the phase difference is given by $k\Delta r$. Therefore, the amplitude of the optical field $E(\alpha)$ for a fringe at an angle $\alpha$ is related to $\Delta\phi(x)$ by

$$E(\alpha) \propto \int_{\text{area of fringe}} dxdy\mathcal{E}_0 e^{i[k\Delta r(\alpha)+\Delta\phi(x)]}, \tag{59}$$

where $\mathcal{E}_o$ is the maximum value of the optical field, where the intensity $I_n$ of the $n$-th order fringe is related to the optical field by $I_n \propto |E(\alpha)|^2$ [9]. The ratio of the intensity of the $n$-th order fringe to that of the central maximum fringe is simply the product of Eq.59 with its complex conjugate for the $n$-th order fringe divided by that for $\alpha = 0$ and $x = 0$. The result is a Bessel function of $\Delta\phi_{max}$ [3]. And so,

$$\frac{I_n}{I_0} = J_{n/2}^2(\Delta\phi_{\max}) \approx \frac{\Delta\phi_{\max}^n}{2^n[(n/2)!]^2}. \tag{60}$$

Conclusively, because $\Delta\phi_{max}^n \propto (\theta_t^2)^n$, it follows that, for small oscillations,

$$I_1/I_0 \propto \theta_t^2 \tag{61}$$

$$I_2/I_0 \propto \theta_t^4. \tag{62}$$

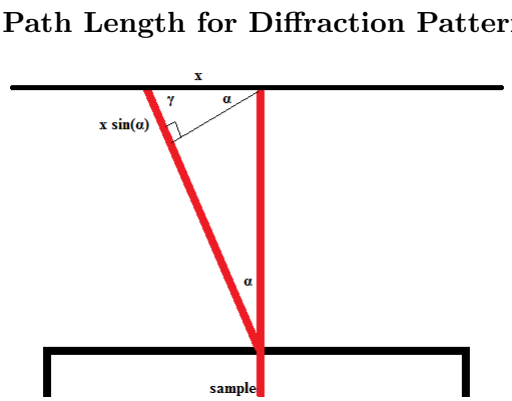


**Figure 10.** Figure showing the path length difference from the diffracted ray and the fundamental ray. Here, $\gamma$ is the angle complementary to $\alpha$.

### 2.3 Flexoelectric Effects

It has been shown that the bending and splaying of nematics with permanent dipoles under an external electric field contribute to a change in the system's internal energy $dU$ [18], which is a sum of the work done by the torques $t_i$ inducing a change in curvature $da_i$, where a curvature is a spatial derivative on a component of the director field $\hat{n}$, with the electric potential energy corresponding to the change in the overall electric displacement $dD_n$ due to these distortions. Hence,

$$dU = t_i da_i + (1/4\pi) E_n dD_n, \tag{63}$$

where $E_n$ is the $n$-th component of the electric field. We may construct a thermodynamic expression known as the "electric enthalphy" $H_E$ [18]. This quantity is given by

$$H_E = U - \frac{\mathbf{D} \cdot \mathbf{E}}{4\pi}. \tag{64}$$

Tus, we see that,

$$\frac{\partial H_E}{\partial a_i} = t_i = k_{ij} a_j - e_{in} E_n, \tag{65}$$

where $k_{ij}$ is the elastic force tensor associated with the constants $K_{11}$, $K_{22}$, and $K_{33}$ and $e_{in}$ is the piezoelectric coefficient tensor [18]. We also see that

$$-4\pi\frac{\partial H_E}{\partial E_n} = D_n = 4\pi e_{in}a_i + \epsilon_{mn}E_m, \tag{66}$$

where $\epsilon_{mn}$ is the dielectric permittivity tensor. It is from these two equations that the flexoelectric polarization vector $\mathbf{P}_{flexo}$ arises, as exhibited in Eq. 16.

When the equations to the SM are solved for the case where $\mathbf{P}_{flexo}$ is added to $\mathbf{D}$, the matrix equation connecting the coupled equations, as exhibited in Eq.33, yields the following solution for the $z$-th component of the director ($n_z$), which is proportional to $\theta$:

$$e^{\zeta t}n_z(z,t) = e^{\zeta t}\Sigma_{n=1}^{N}\Sigma_{k=-K}^{K}\overline{n_z}(n|k)e^{ik\omega t}S_n, \tag{67}$$

where $\overline{n_z}(n|k)$ is a complex constant with a constant phase [6].

$$S_n = \cos\left[n\pi z/d\right], \tag{68}$$

with $d$ being the thickness of the cell [6]. It turns out that the two different regimes of oscillation in this case that solve Eq. 33 are for when either $|n+k|$ is odd or even[6]. Thus, it is not unusual to measure harmonics of electroconvection with both odd and even modulations, nor is it unusual to observe several local maxima with respect to $z$ for the director distortion angle when considering flexoelectric polarization.

# 3 Methodology

For this investigation, I am determining the external driving frequencies and voltages at which various patterns form under director distortions, i.e., oblique rolls, normal rolls, dielectric rolls, traveling rolls. This is to be done with microscopy. Subsequently, I will study He-Ne laser diffraction to examine the intensity versus time and frequency curves of the first and second order fringes from the resulting pattern. From these curves, it is possible to discern the harmonics of the director distortion angle.

Three Aldrich® N-(4-methoxybenzylidene)-4-butylaniline (MBBA) (Fig. 11) samples with a 98% purity are inserted between two slides of separated at a distance $d = 20\mu$m with a disposable pipette.

They are then sealed with a 5-Minute Epoxy® mixture of resin and hardener to prevent any additional impurities into the display. The slides have a polyimide layer to create a planar alignment within the cell; furthermore, each slide features a layer of indium tin oxide (ITO) to serve as an electrode for the sample. Before the cell may be used for the experiment, the glass must be cleaned with methanol.

**Chemical Structure of MBBA**

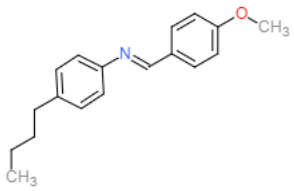


**Figure 11.** Chemical structure of MBBA [1].

The glass slides are cleaned as follows. A lens-cleaning paper is tightly folded at the corners (it is important not to touch the paper) into a small square. The edge of the paper, held by plastic forceps, is soaked with methanol. With the forceps, each side of the cell is stroked with the paper in one direction. This is important because "mopping" the slides would result in the wiped-off dirt being brushed onto the cell.

An Instec® cell holder, shown in Fig. 12, features two electrodes, one grounding and one positive, which may be connected to the top and bottom ITO slides of the cell with copper foil tape. The BNC cable connectors on the holders are connected to the output of a function generator of a sinusoidal wave and a ground.

**Cell Holder Apparatus**

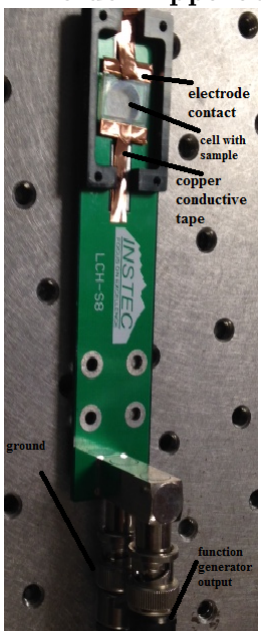


**Figure 12.** The electrodes connect to the top and bottom slides through copper foil tape. The bottom BNC connector attaches to the ground while the top connects to the output from the function generator.

It is important that the temperature of the sample not exceed the critical value at which MBBA exists in the liquid phase. Therefore, a temperature controlling system is required to sustain a temperature around 20.0°C, as it is reported in literature [19]. The system will require two Peltier coolers, shown in Fig. 13, that, when charged by the temperature controller, expel heat to a heat sink. In this instance, the heat sinks used are copper fins attached to the Peltier coolers with a thermally conductive adhesive. When activating the temperature controller, shown in Fig. 14, the arrows shown on the console allow the desired temperature to be set (in °C); it is important to know that the plate to which the leads of the temperature controllers are attached will be heated and should be in contact with the heat sink [20].

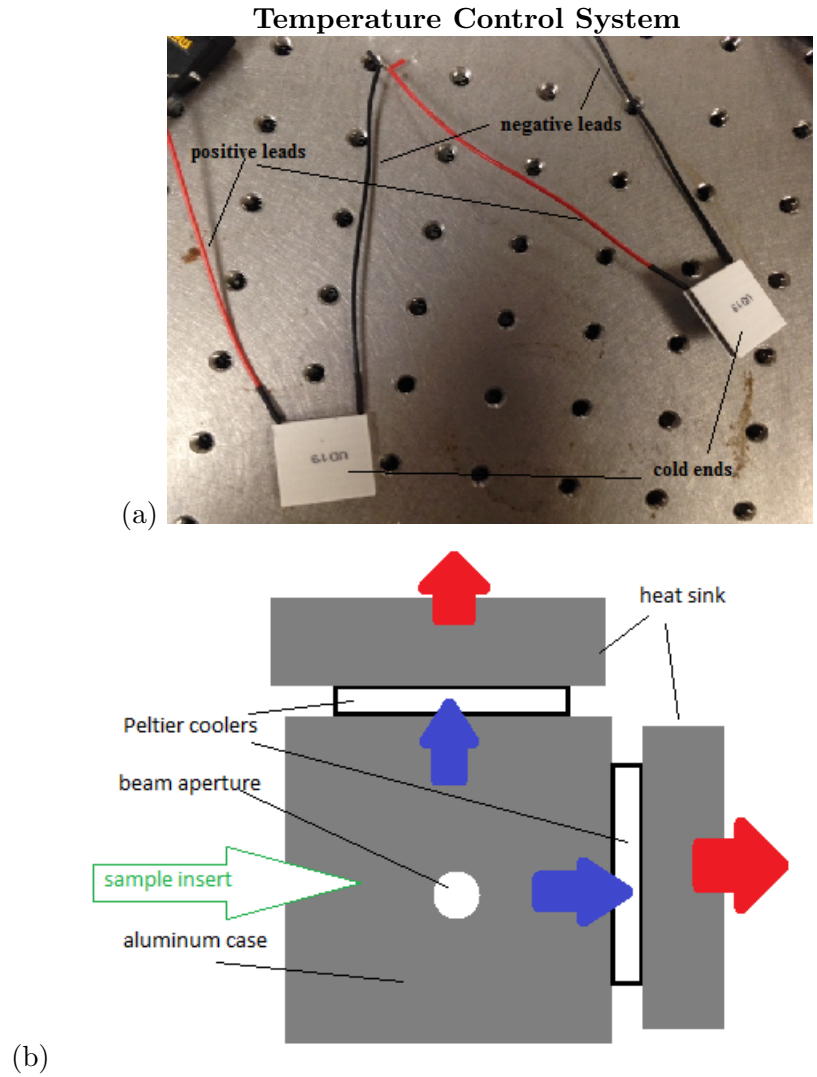


**Figure 13.** In (a), the two Peltier coolers are connected in series while a (+) lead and (-) lead are connected to the corresponding leads of the temperature controller. The bottom plate of these coolers will come in contact with the heat sink while the top plate is to be in contact with the aluminum case, as it is the "cold end." In (b), the apparatus is shown during a cooling phase. The cell holder fits into the case through the left side. Heat is expelled from the aluminum case (with its circular aperture for the laser beam) when the temperature controller delivers a current to the (+) lead for the series of coolers. The heat sink, a copper fin, absorbs this heat that is expelled into the atmosphere with a computer fan [20].

Microscopy is used to locate the Fréederickz transitions at certain rms-voltages ($V_c$) for frequency settings, i.e., the transitions at which the net torque on the director is nonzero and electroconvective patterns emerge. This portion of the experiment is done by setting the frequency of the function generator from 20 to 200 Hz in 10 Hz increments and slowly adjusting the peak-to-peak voltage of

the sinusoid from zero to a value at which an identifiable pattern emerges. The pattern type, driving frequency, and rms-voltage is recorded. This range of frequencies is selected because it has been used before to identify the regimes of oblique and normal rolls in nematics [8]. The temperature of the sample, however, must still be held around 20.0°C, lest an inconsistent relationship between rms-voltage and sinusoidal frequency may be determined. This is done for the three different samples of MBBA.

**Temperature Controller Front Console**




**Figure 14.** Front console of temperature controller. The arrows adjust the temperature setting, while the actual temperature is shown above in °C. LED 1 signifies that current is being supplied to the coolers for cooling; LED 2 indicates that it is being supplied for heating. LED 3 indicates that the power is shut off to prevent the coolers from overheating; LED 4 is associated with adjustments to the operation. The "%" LED is indicates whether the device is in automatic or manual mode [19]. The bottom left two buttons are associated with scrolling through the settings of the device.

The harmonics of the director distortion angle can be determined from the intensity of light scattered for a He-Ne laser beam diffracted by the gratings produced by the director instabilities. Previous experiments have confirmed a $I_1/I_0 = \theta(t)^2$ and $I_2/I_0 = \theta(t)^4$ relationship in the instensity $I_n$ of the $n$-th ordered fringe, where $\theta(t)$ is the director distortion angle with respect to time [8,9]. These dependencies arise from the phase shift in the laser's electric field due to it propagating through director-distortion-dependent refractive index of the sample [4].

The optical setup is shown in Fig. 15. Because the electric field of the incoming laser light

would be polarized in the rubbing direction of the directors along the $xy$-plane, it is important that the optical field of the He-Ne laser light remain parallel to it. Thus, a half waveplate rotates the optical field of the vertically polarized beam in the direction of the polyimide rubbing direction on the cell [9,14]. To ensure that the intensity of the incident beam does not influence the torques on the director field, the diameter of the beam is decreased with a two-lens system, shown in Fig. 16. Once the diffraction pattern emerges from the sample, the fringes detected by the photodiode tend to be unfocused. Therefore, a converging lens could reduce such spherical aberration and, consequently, minimize the amount of noise detected; however, one was not used in this study.

**Diffraction Experiment Schematic**

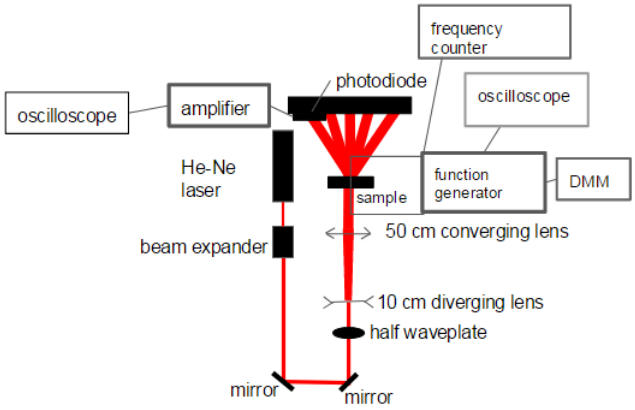


**Figure 15.** A He-Ne laser is directed to a 632.8 nm half waveplate with mirrors; the beam is then expanded by means of a diverging lens in series with a converging lens. The beam is then incident on the convecting sample within the aluminum case through the aperture. This light is diffracted; a photodiode is illuminated by one of the fringes. When the photodiode detects the signal, it is then amplified by a large dynamic range amplifier for the digital oscilloscope.

**Lens System for Increasing Beam Diameter**

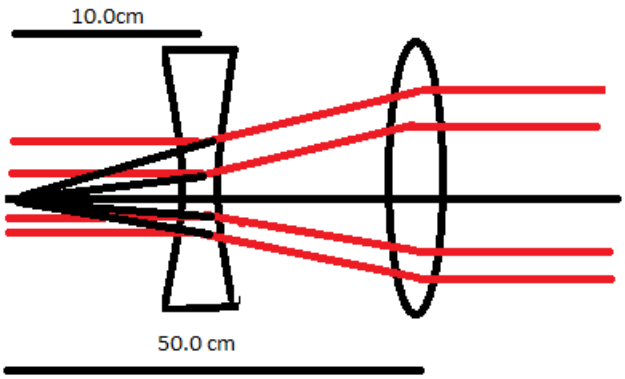


**Figure 16.** The diverging lens with a focal length of -10.0 cm is spaced approximately 40.0 cm from the converging lens with focal length of 50.0 cm. This results in the magnification of the incident beam.

The photodetection system uses a photodiode with a neutral density filter (for preventing saturation) for the conversion of photons into an electric signal and is set up so that a minimum amount of noise in the detected intensity signals is acquired. A photodiode is connected, by means of a BNC cable, to a Melles Griot® large dynamic range amplifier, an op-amp circuit that amplifies the electric signal detected by the photodiode, shown in Fig. 17. When conducting experiments, it is important to have the range setting at mA and adjusting it accordingly so that saturation in the op-amp does not occur [21]. The output of this device is then connected to a Lecroy® Waverunner LT322 digital oscilloscope for the time and frequency domains of the fringe intensity curves to be determined.

**Large Dynamic Range Amplifier**




**Figure 17.** The knob sets the current range at which the op-amp circuit will take. If one does not know the order of magnitude of the incoming current, one should should select "mA" in order to prevent saturation in the device. The input BNC connector, shown on the left, connects to the photodiode while the output

shown on the right connects to the oscilloscope.

By selecting "Find" in the Channel 1 control panel for the oscilloscope, the detected intensity versus time curve will be obtained. In order to average this curve over the frequency domain, "Math Tools" must be selected. Under "Math Type", "Average" and "Summed" must then be selected, and, under the "of" menu, the appropriate channel is selected. This procedure yields a summed average of the intensity curve, which displays a large reduction in noise. Another significant math tool that must be used is the fast Fourier transform (FFT) to transform the curves from a time domain to a frequency domain. This is done on the oscilloscope by selecting "FFT" under "Math Type"; a "Power Spectrum" of the transform "of" channel "1" must be selected in order for the oscilloscope to exhibit the power (in dB) of the frequency peaks [22]. Be sure to reduce the sampling rate to at most 100kS/s. Furthermore, "AC" must be selected under the "with window" menu in order to filter out any DC signals. It is prudent to take a summed average of this frequency domain waveform in order to greatly reduce noise. Once waveforms are obtained, they are ready to be saved for analysis. The "Wave Storage" option on the oscilloscope allows for the labeled waveforms to be stored into memory. Under the "Store" menu, the waveform to be stored is selected. It is then stored "to" the desired memory. By selecting "Do Store", the waveform is saved to the memory [22].

This diffraction experiment is done with a sinusoidal driving signal on the electrodes of the liquid crystal cell at frequencies in the 10-200Hz range. This is done at voltages sufficiently above the corresponding $V_c$ such that a clear diffraction pattern around threshold is formed. The time and frequency domain curves are recorded for the first order fringes, as well as the second order fringes for each of the three liquid crystal cells.

# 4 Results & Analysis

The sample thickness was measured via transmittance spectra of empty cells, as explained in Section 0.2 of the Appendix. The cells were measured and found to have thicknesses of $20.3 \pm 0.3\mu$m, $20.0 \pm 0.1\mu$m, and $20.2 \pm 0.1\mu$m for cells A, B, and C respectively. Once MBBA is inserted into the cells, it occupies these thicknesses.

The voltage ($V_c$) dependence on ac frequency, at which a grating pattern was discerned throughout the sample for cells A, B, and C, is shown in Fig. 18 and is consistent with previous studies done on

MBBA. The samples were held at 23.0±0.1° C. Frequency was measured with a frequency counter while the rms-voltage of the applied field was measured with a digital multimeter (DMM). The measured uncertainties in $V_c$ correspond to the coarseness of the amplitude knob of the function generator (FG) of the sinusoid [18,22]. The exact point of transition has a possibility of lying within the measured uncertainty. Measured uncertainties in the frequencies correspond to fluctuations in the frequency counter.

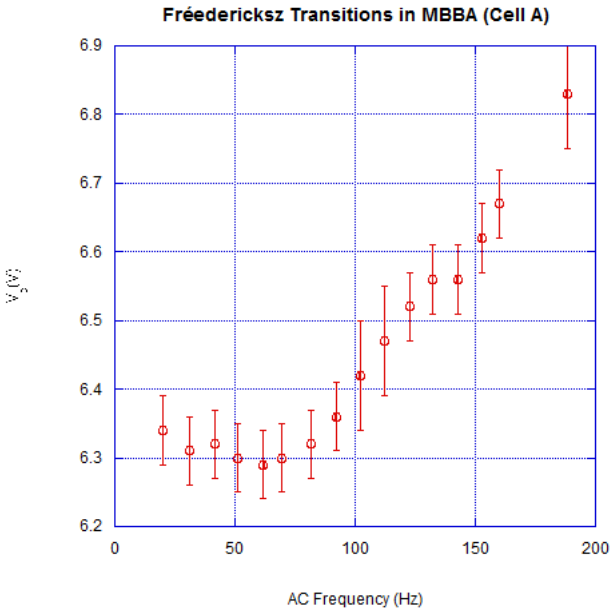


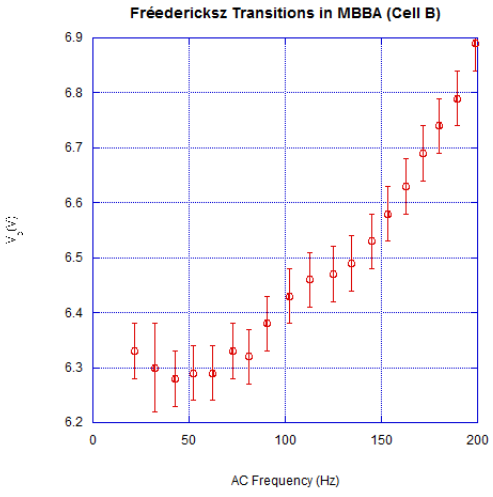

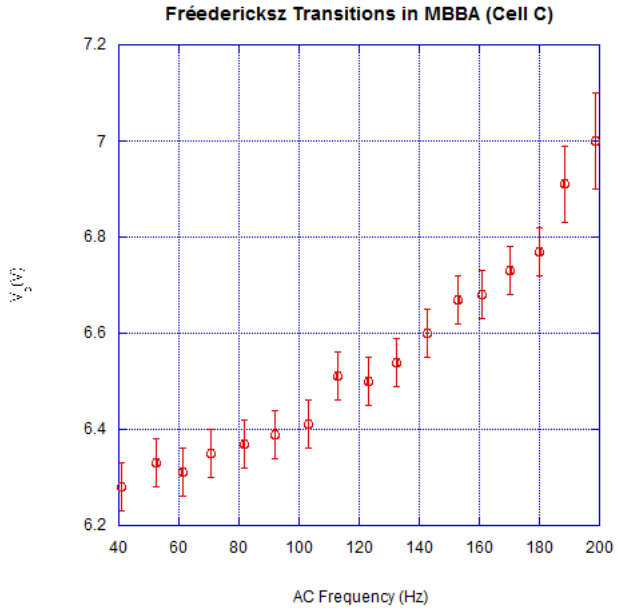


**Figure 18.** The threshold voltages at which the rolling patterns appeared under the microscope are shown for cells A, B, and C. Applied rms-voltages greater than the ones recorded at a particular frequency lead to a turbulent pattern within the sample.

A laser diffraction experiment was conducted on cell C, at temperatures $T \approx 23.0°\text{C}$ with a sinusoidal driving field of frequencies ranging from $30\text{Hz} - 190\text{Hz}$, where the driving field's frequency is represented by $f$. However, the effect of spherical aberration was not prevented in this experiment, as the converging lens was producing fringes that were not sufficiently resolved to be individually detected by the photodiode; a potential solution to this issue is discussed in the "Conclusion  Discussion" section. For the cell C measurements, the detector was placed on a second-order fringe to the left of the fundamental beam $(-2)$, where the intensity waves and FFT power spectra were captured from the digital oscilloscope. The measured time-dependence of the intensity of the fringe at a driving field of frequency $f = 59.6\text{Hz}$, along with the corresponding FFT power spectrum, is displayed in Fig. 19-20. A complete set of graphs is found in the "Appendix."

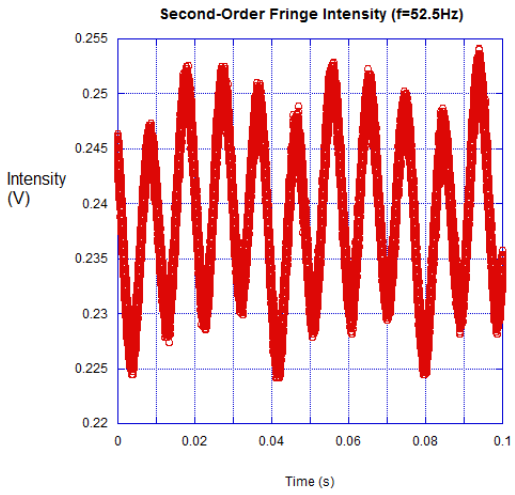


**Figure 19.** Here is a stored waveform exhibiting the time dependence on the intensity of the second-order fringe of the diffraction pattern. This curve is an amplified waveform of the signal detected by the photodiode.

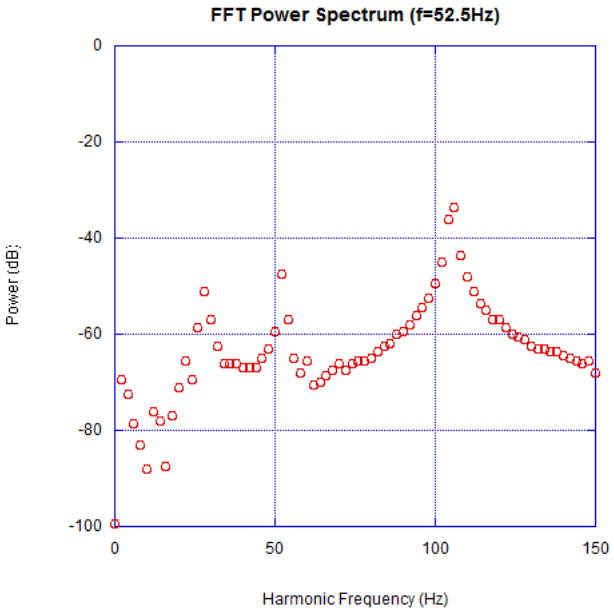


**Figure 20.** The waveform of Fig. 19 under the fast-Fourier transform algorithm is displayed here, exhibiting peaks at $0, \frac{f}{2}, f, 2f$.

Fig. 20 provides proof that the pattern exists within the conduction regime, as shown by the upward

slope at 0 and peak at $2f$ (a 0Hz harmonic frequency corresponds to a constant term). The peak at the $f$ harmonic frequency in the power spectrum provides support to the solutions of the SM when flexoelectric polarization is introduced [6,8]. What is the most unusual finding in Fig. 20, is the presence of a subharmonic frequency $\frac{f}{2}$ in some power spectra, as shown by the peak. While a subharmonic frequency has been detected before in laser diffraction experiments under asymmetric driving fields [24], theoretical work has shown that antisymmetric driving fields (e.g., sinusoidal, square), cannot allow the existence of subharmonics [25,26], hence its unusual presence.

Further evidence for this regime of harmonic driving is given by convective roll spacing measurements conducted by measuring the spaces between the diffraction fringes. An average roll spacing for cell C was found to be $d = 19.67 \pm 0.61\mu$m, where the uncertainty comes from the quotient between the standard deviation of seven measurements and the root of the sampling size. This roll spacing is expected for convection in the conduction regime, as found in the solutions to the SM [5]. For cell A, this spacing was found to be $d = 19.3 \pm 0.6\mu$m.

Two laser diffraction experiments were conducted on cell A held at $T \approx 23.0°$C at ac driving fields of $f$ spanning from 20Hz-200Hz. The photodiode was placed on the second-order diffraction fringe to the left of the fundamental beam (-2). In both experiments, FFT power spectra underwent summed averages of 1000 sweeps with sampling rates of 50-100kS/s (kS signifies 1000 samples). It was expected that the excessive noise found on the power spectra on cell C samples would diminish, including the subharmonics, as the FFT waveform was captured at single instances during the harmonic driving. Fig. 21 collected at an $f = 70.3$Hz exhibits the presence of $f, 2f, 3f,$ and$4f$, i.e., the coexistence of odd and even harmonics as mentioned earlier [6,8]. This waveform yields an estimated FWHM linewidth of 8Hz surrounding the measured peaks at harmonic frequencies $f = 21.75$Hz, $2f = 41.75$Hz, $3f = 63.75$Hz, and $4f = 81.75$Hz. Furthermore, the omission of a subharmonic frequency is exhibited in this spectrum as expected. It should be noted that these measured frequencies are actually bins designated by the oscilloscope during the FFT algorithm. Additional summed-averaged power spectra for cell A are included in the "Appendix."

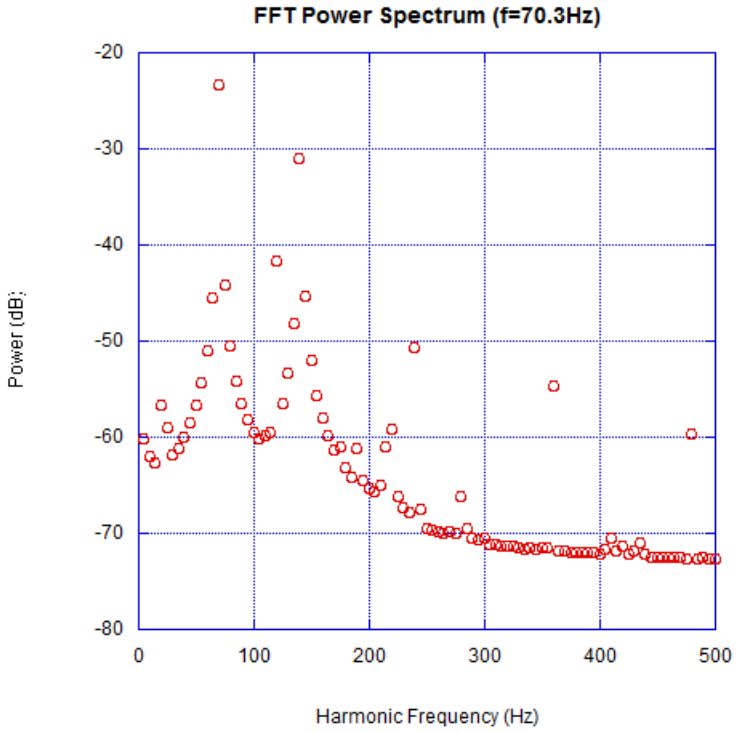


**Figure 21.** The FFT on cell A held with a driving $f = 70.3$Hz at $T \approx 23.0°$C exhibits the measured harmonics $f = 69.5$Hz and $2f = 139.5$Hz with a FWHM linewidth of of 8Hz.

The second diffraction experiment conducted on cell A involved reducing the leakage of the spectra by mixing the detected intensity signal with a Von Hann window on the oscilloscope. Essentially, spectral leakage occurs when the FFT algorithm collects data from the time-domain wave at a sampling rate that allows it to begin and cease sampling when the input signal has not completed an integer number of periods. This leads to a decrease in the frequency resolution as shown in the previously presented data; ideally, there would be a single peak at $f = 70.3$Hz in Fig. 21 instead of a distribution of peaks. The issue of spectral leakage and its rectification by Von Hann windowing (or Hanning) is further explained in the "Appendix."

One spectrum obtained from the data collected during this second experiment at an ac driving frequency of $f = 71.4$Hz is shown in Fig. 22, where the measured harmonics were found to be $f = 69.5 \pm 5.0$Hz and $2f = 139.5 \pm 5.0$Hz. The uncertainties provided with these measurements are not FWHM linewidths. They are simply the widths of the frequency bins calculated by the FFT

algorithm because we must assume, for instance, that the fundamental harmonic frequency must be within 64.5Hz and 74.5Hz. The FWHM linewidths for these measurements are estimated to be much less than the 10Hz width provided by the uncertainty. However, given the conservative FWHM value of $\Delta f = 10\text{Hz}$, we see by the uncertainty relation

$$\Delta f \Delta t \geq \frac{1}{4\pi} \tag{69}$$

that lifetime of the oscillation is $\Delta t \geq 7.9\text{ms}$. This uncertainty in oscillations can assist in determining the diffusion coefficient $D$ of the molecular flow when related to the scattering angle $\alpha$ from the fundamental beam of the diffraction pattern. If $\lambda$ is the wavelength of the He-Ne laser, then different uncertainties in oscillation lifetimes $\Delta t$ can be related to this angle in the following way:

$$\frac{1}{\Delta t} = D\left(\frac{16\pi^2 m^2 \sin^2\left[\alpha/2\right]}{\lambda^2}\right), \tag{70}$$

where $m$ is the $m$-th order diffraction fringe. Thus, it is prudent to get a fit of spectral peaks reasonable enough to determine an accurate $\Delta t$.

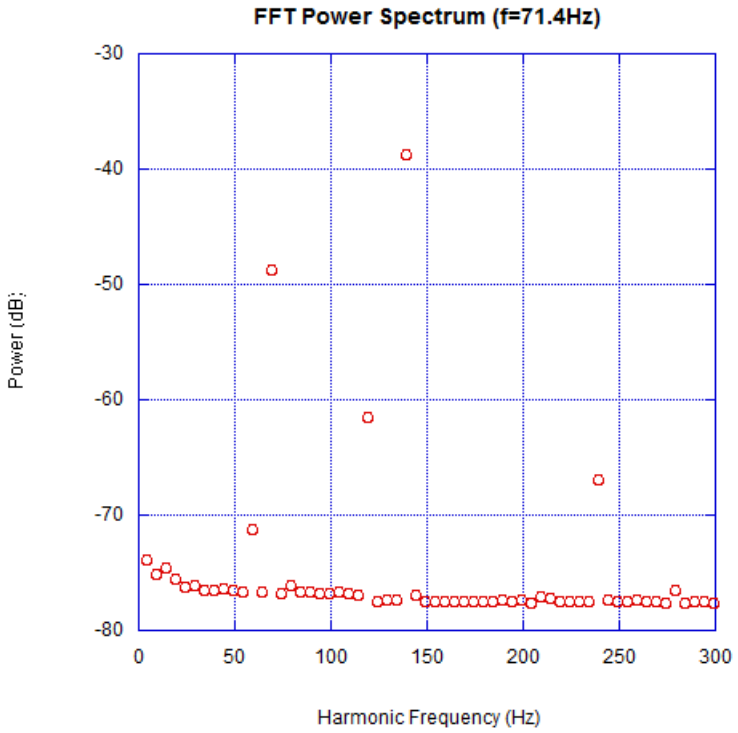

**Figure 22.** The Hann windowed FFT on cell A held with a driving $f = 71.4$Hz at $T \approx 23.0\circ$C exhibits the measured harmonics $f = 69.5 \pm 5.0$Hz and $2f = 139.5 \pm 5.0$Hz.

It should also be noticed that 60Hz harmonics appear throughout each spectrum, where this is assumed to come from the power source of the lab and a lack of a notch filter for these frequencies in the photodetection system. Such noise could be the source of a bias for the data presented. The frequencies of the driving field were subsequently selected in the third trial on cell A such that the response harmonics did not correspond with those of background signals.

In another diffraction experiment on the cell (Fig.23), an FFT power spectrum for $I_{-2}$ is shown in Fig. 24 for the sample under an ac driving field of 130.2Hz held at $23.0 \pm 0.1$°C . In addition to the $f$ and $2f$ harmonics being present in the response to the driving field, a 30Hz modulation is also apparent. This is more evident in the time domain of $I_{-2}$, shown in Fig. 25. Whether this is an effect of unwanted mixing in the detector or an actual response of the nematics under the field is currently under investigation. Additional FFT power spectra for this trial are featured in the "Appendix."

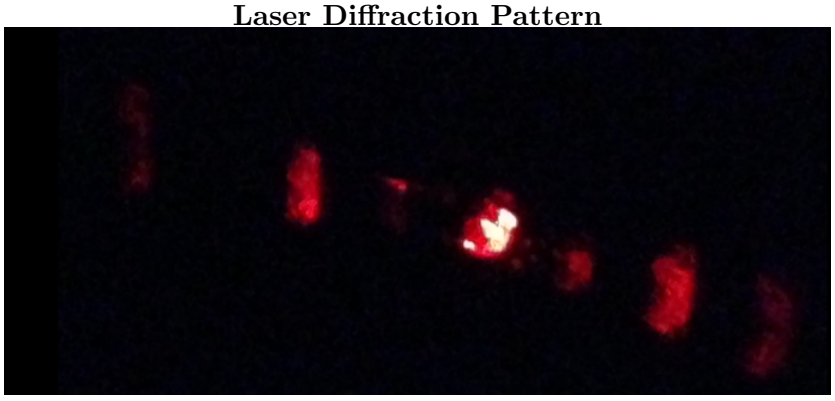


**Figure 23.** Laser diffraction pattern resulting from electroconvective grating.

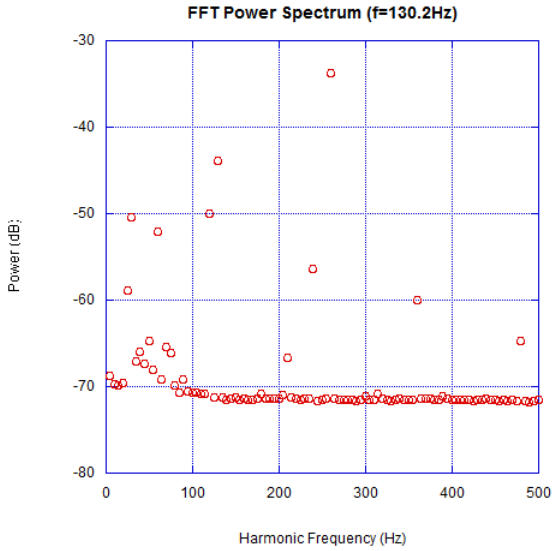


**Figure 24.** The Hann windowed FFT on cell A held with a driving $f = 130.2$Hz at $T = 23.0 \pm 0.1$°C exhibits the measured harmonics $f = 129.5 \pm 5.0$Hz, and $2f = 259.5 \pm 5.0$Hz.

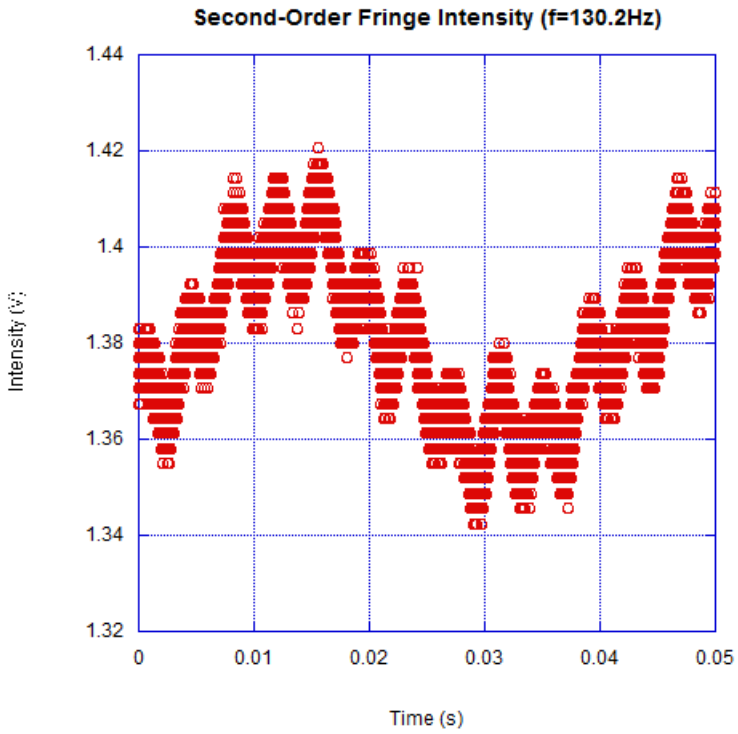


**Figure 25.** The time domain of $I_{-2}$ corresponding to the FFT spectrum in Fig. 23 is presented. A 30Hz

frequency is noticible in the time domain.

In order to provide evidence that coexistence of both odd and even harmonics in the temporal response of the LC was not unique to the $(-2)$-order fringe, measurements were taken on the central fringe and on the $(-4)$-order fringe. For the central fringe measurements, it can be inferred that the system is responding with a linear combination of odd and even harmonics as was shown in $I_{-2}$. An example is the measurement of harmonics for the LC that was driven with a frequency of 189.6Hz, shown in Fig. 26., where the existence of the $f, 2f$, and $3f$ harmonics can be discerned with uncertainties of $\pm$5.0Hz. It should also be noted that the 30Hz modulation was again measured but appears negligible in comparison with the expected harmonic response. Other measurements on the central fringe appear to have a 30Hz modulation as well; these graphs are presented in the "Appendix."

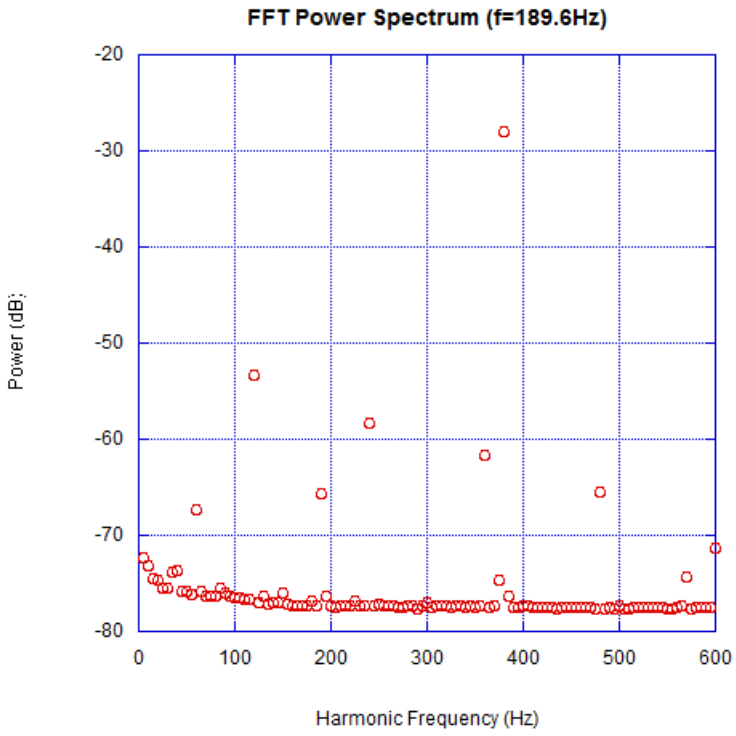


**Figure 26.** The Hann-windowed FFT on cell A from signal $I_0$ with a driving $f = 189.6$Hz at $T = 23.0 \pm 0.1°$C exhibits the measured harmonics $f = 189.5$Hz$\pm$5.0Hz, $2f = 379.5$Hz$\pm$5.0Hz, and $3f = 569.5$Hz$\pm$5.0Hz.

The director distortion angle also exhibited a linear combination of odd and even harmonics when the $I_{-4}$ signal was observed with the results of a measurement taken under a driving frequency of

$f = 189.9$Hz, as shown in Fig. 27., where the harmonics $f$ and $2f$ were observed.

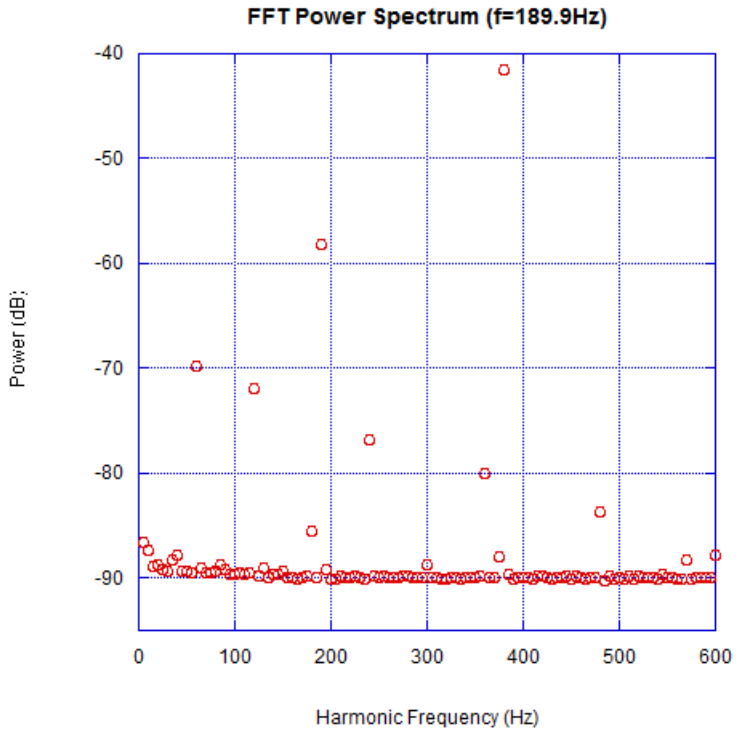


**Figure 27.** The Hann-windowed FFT on cell A from signal $I_{-4}$ with a driving $f = 189.9$Hz at $T = 23.0 \pm 0.1°$C exhibits the measured harmonics $f = 189.5$Hz$\pm 5.0$Hz and $2f = 379.5$Hz$\pm 5.0$Hz.

Fig. 27 also unfortunately displays almost every consecutive harmonic of 60Hz which arises from background signals and the power supply. This unwanted noise must be accounted for by exhibiting its existence during photodetection without the presence of the incident laser beam. In Fig. 28, peaks in the FFT spectrum during this run at 60Hz and 180Hz were detected. These higher-order harmonics of 60Hz may be the results of electrical background signals incident upon the sample undergoing the nonlinear response of the electroconvective rolls and director distortion angle or mixing with other signals upon being received by the photodiode.

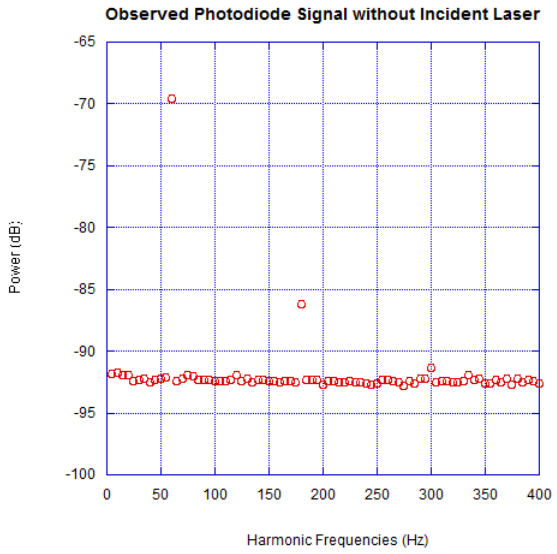


**Figure 28.** The Hann-windowed FFT of a photodiode signal not receiving a photons from a laser fringe. The 180Hz harmonic could either come from the mixing of 60Hz background signals or the nonlinear response from passing through the sample.

Because the efficiency of the production of harmonics from a function generator is not ideal, it is possible that the Fourier expansion of the output signal includes higher-order harmonics. A sinusoidal signal with a frequency $f$ =150.2Hz was produced and wired to the digital oscilloscope, where an FFT algorithm on the intensity vs. time signal was conducted. This spectrum is shown in Fig. 29 where higher-order harmonics are indeed found.

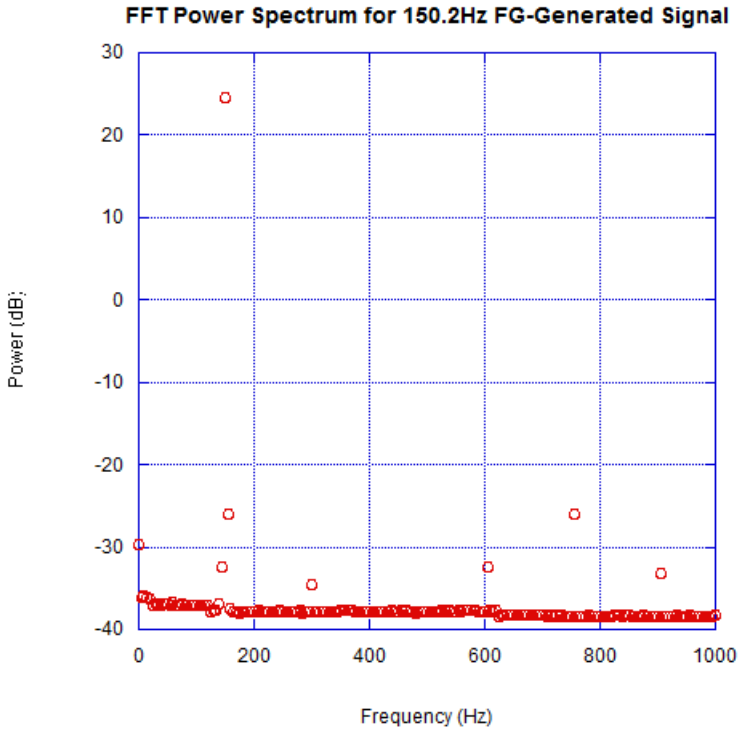


**Figure 29.** Resulting Hann-windowed FFT of a 150.2Hz output signal from a function generator (FG); higher-order harmonics, i.e., $2f$, $4f$, and $6f$ are evident.

## 5 Conclusion & Discussion

In summary, nematic LC samples of MBBA held at $T = 23.0 \pm 0.1°\text{C}$ with a planar alignment along two glass electrodes were driven under ac fields with magnitudes sufficient to induce electroconvective rolls, which were be observed underneath a polarizing microscope. In the conductive regime, where the molecules are expected to convect with even harmonics of the driving frequency $f$, it was found from the scattering of 632.8nm light that odd harmonics of $f$ were permissible. This finding supports extensions to the SM in which flexoelectric polarization is considered and allows temporal solutions to have combinations of odd and even harmonics [6,8]. It can be assumed that the rolls were characteristic of those in the conduction regime by measuring the spacing of the fringes in the pattern produced by the grating electroconvection generates. For cell C, it was found from this method that the rolls were spaced at $d = 19.67 \pm 0.61\mu\text{m}$, which aligns with the uncertainties imposed from the cell thickness

measurement of $20.2 \pm 0.1\mu$m. For cell A, the spacing was determined to be $d = 19.3 \pm 0.6\mu$m, which agrees with the cell thickness measurement of $20.3 \pm 0.3\mu$m. It was also estimated from an uncertainty relation that the oscillations in the samples have a minimum lifetime of 7.9ms.

Additional experiments on the temporal behavior of the electroconvective molecules should be conducted in the future. It is not clear how the relative power of the frequency peaks in the FFT spectra change with different experimental conditions. In my experiment, the rms voltage was adjusted for the samples so that the maximum amplified signal could be received by the oscilloscope. For a future experiment, it would be prudent to observe the ratios of the FFT amplitudes of the $f$ to the $2f$ peak as a function of the rms voltage $V_{rms}$ and the control parameter $\epsilon = V/V_c - 1$. It is also important to note that the FFT spectra obtained are time averages over 1000 sweeps of the time-domain intensity wave.

Two other experiments worth conducting involve the measurement of the diffusion coefficient $D$ from the FWHM of the peaks in the FFT spectra. However, this requires and accurate fitting of the peaks, which is difficult to obtain when only one data point characterizes it. Additionally, by reducing the sampling rate of the FFT algorithm, it would be possible to observe how the director distortion angle behaves at larger timescales and possibly measure the Floquet constant $\zeta$.

Some common complications that were experienced in the lab involved the fact that the FG did not generate an ac field solely at the fundamental harmonic; in the Fourier expansion, of the signal, higher-order harmonics are evident, as seen in Fig. 29. However, the fact that the electroconvective behavior had the ability to suppress the fundamental harmonic in some instances (as seen on the $I_{-4}$ FFT spectra in the "Appendix") and oscillate with its modulation at other instances still does not refute the evidence of flexoelectric effects. In the future, a lock-in amplifier should be wired to the FG before the driving signal reaches the electrodes. Additionally, in order to reduce the effect of spherical aberration in the fringes, it would be wise to place a converging lens before the photodiode. However, due to issues with the resolution of the fringes, it would be of interest to devise a setup to couple a fringe into a single-mode fiber in order that light from the fringe under study is the only one to reach the photodiode. Further studies, such as using LDV to quantify the velocity of the flow are also of interest.

## References


1. P. J. Collings. *Liquid Crystals: Nature's Delicate Phase of Matter*; Princeton University Press: Princeton (2002).

2. M. Dennin, D. S. Cannell, and G. Ahlers. "Patterns of electroconvection in a nematic liquid crystal." Phys. Rev. E **57**, 638-649 (1998).

3. G. R. Acharya. *Electroconvection and Pattern Formation in Nematic Liquid Crystals.* Ph.D. Dissertation, Kent State University, Kent, OH (2009).

4. M. Dennin, M. Trieber, L. Kramer, G. Ahlers, and D. S. Cannell. "Origin of Traveling Rolls in Electroconvection of Nematic Liquid Crystals." Phys. Rev. Lett. **76**, 319-322 (1996).

5. E. Bodenschatz, W. Zimmermann, and L. Kramer. "On electrically driven pattern-forming instabilities in planar nematics." J. Phys. France **49**, 1875-1899 (1988).

6. A. Krekhov, W. Pesch, N. Éber, T. Tóth-Katona, and Á. Buka. "Nonstandard electroconvection and flexoelectricity in nematic liquid crystals." Phys. Rev. E **77**, 021705 (2007).

7. W. Helfrich. "Conduction Induced Alignment of Nematic Liquid Crystals: Basic Model and Stability Considerations." J. Chem. Phys. **51**, 4092-4105 (1969).

8. T. Tóth-Katona, N. Éber, and Á. Buka. "Temporal response to harmonic driving in electroconvection." Phys. Rev. E **83**, 061704 (2011).

9. T. John, U. Behn, and R. Stannarius. "Laser diffraction by periodic dynamic patterns in anisotropic fluids." Eur. Phys. J. B **35**, 267-278 (2003).

10. D. Funfschilling, B. Sammuli, and M. Dennin. "Patterns of electroconvection in the nematic liquid crystal N4." Phys. Rev. E **67**, 016207 (2002).

11. A. Krekhov *et al.* "Patterns driven by combined ac and dc electric fields in nematic liquid crystals." Phys. Rev. E **89**, 052507 (2014).

12. S. M. Kelly and M. O'Neill. *Liquid Crystals for Electro-Optic Applications*; Academic Press: Cambridge (2000). 13. K. Kondo, M. Arakawa, A. Fukunda, and E. Kuze. "Light propagation in Williams Domains as Analyzed Numerically by Geometrical Optics." Jpn. J. Appl. Phys. **22**, 394-399 (1983).

14. J. A. Kosmopoulos and H. M. Zenginoglou. "Geometrical optics approach to the nematic liquid crystal grating: numerical results." Appl. Opt. **26**, 1714-1721 (1987).

15. T. O. Carroll. "Liquid-Crystal Diffraction Grating." J. Appl. Phys. **43**, 767 (1972).

16. F. Castles, S. M. Morris, and H. J. Coles. "The limits of flexoelectricity in liquid crystals." AIP

Advances **1**, 032120 (2011).

17. K. Kiger. "Introduction to Laser Doppler Velocimetry." Burgers Program for Fluid Dynamics, Turbulence School (2010).

18. R. B. Meyer. "Piezoeelectric Effects in Liquid Crystals." Phys. Rev. Lett. **22** 918-921 (1969).

19. N. C. Giebink, E. R. Johnson, S. R. Saucedo, E. W. Miles, K. K. Vardanyan, D. R. Spiegel, and D. S. Allen."Dynamics of laser-induced electroconvection pulses." Phys. Rev. E **69**, 066303 (2004).

20. *Series 800 and Series 850: Thermoelectric Cooler Controller Instruction Manual.* Cumberland: Alpha Omega Instruments (2002).

21. *Large Dynamic Range Amplifier: Operator's Manual.* Boulder: Melles Griot (1993).

22. *Waverunner: Operator's Manual.* Chestnut Ridge: LeCroy Corporation (2002).

23. E. A. Kirsanov, A. A. Razumov, and Y. S. Mushnikov. "Threshold characteristics of electroconvective flow in nematics." Sov. Phys. JETP **54**, 310-313 (1981).

24. T. John and R. Stannarius. Preparation of subharmonic patterns in nematic electroconvection. Phys. Rev. E **70**, 025202 (2004).

25. T. John, J. Heuer, and R. Stannarius. "Influence of excitation wave forms and frequencies on the fundamental time symmetry of the system dynamics, studied in nematic electroconvection." Phys. Rev. E **71**, 056307 (2005).

26. R. Stannarius, J. Heuer, and T. John. "Fundamental relations between the symmetry of excitation and the existence of spatiotemporal subharmonic structures in a pattern-forming dynamic system." Phys. Rev. E **72**, 066218 (2005).

27. P.G. De Gennes and J. Prost. *The Physics of Liquid Crystals, Second Edition*; Oxford University Press: Oxford (1993).

28. F.J Harris. "On the Use of windows for Harmonic Analysis with the Discrete Fourier Transform." Proceedings of the IEEE **66**, No. 1, 51 (1978).

29. D. Lyon. "The Discrete Fourier Transform, Part 4: Spectral Leakage." Journal of Object Technology **8**, No. 7, 23 (2009).

# Appendix

## Lagrange Multipliers

I will show how variational calculus is used to derive the Euler-Lagrange equations for a system of two generalized coordinates ($q_1$ and $q_2$) constrained by the function $f = \text{const}$.

The action $S$ associated with the Lagrangian $L$ of this system is given by

$$S = \int L(q_1, q_2, \dot{q}_1, \dot{q}_2)dt. \tag{71}$$

Let's assume that the paths of least action formed by $q_1$ and $q_2$ are perturbed by $\delta q_1$ and $\delta q_2$. Then the small change in $S$ becomes $\delta S$. The functional derivative is the rate of change in the time-dependent function $S$ with respect to the time-dependent function $q_i$, where $i = 1, 2$. Thus,

$$\delta S = \int \left( \frac{\partial L}{\partial q_1}\delta q_1 + \frac{\partial L}{\partial q_2}\delta q_2 + \frac{\partial L}{\partial \dot{q}_1}\delta \dot{q}_1 + \frac{\partial L}{\partial \dot{q}_2}\delta \dot{q}_2 \right) dt. \tag{72}$$

For the moment, we will consider the part of the integral containing $q_1$ and its time derivative $\dot{q}_1$, so

$$\begin{aligned} \delta S = \int \left( \frac{\partial L}{\partial q_1}\delta q_1 + \frac{\partial L}{\partial \dot{q}_1}\delta \dot{q}_1 \right) dt = \int \left( \frac{\partial L}{\partial q_1}\delta q_1 + \frac{\partial L}{\partial \dot{q}_1}\delta \frac{dq_1}{dt} \right) dt = \int \left[ \frac{\partial L}{\partial q_1}\delta q_1 - \frac{d}{dt}\left( \frac{\partial L}{\partial \dot{q}_1}\delta q_1 \right) \right] dt \\ = \int \left[ \frac{\partial L}{\partial q_1} - \frac{d}{dt}\left( \frac{\partial L}{\partial \dot{q}_1} \right) \right] \delta q_1 dt, \end{aligned} \tag{73}$$

where the last two steps come from integration by parts. In order to minimize $S$,

$$\frac{\delta S}{\delta q_i} = 0. \tag{74}$$

Thus,

$$\delta S = \int \left( \left[ \frac{\partial L}{\partial q_1} - \frac{d}{dt}\left( \frac{\partial L}{\partial \dot{q}_1} \right) \right] \delta q_1 + \left[ \frac{\partial L}{\partial q_2} - \frac{d}{dt}\left( \frac{\partial L}{\partial \dot{q}_2} \right) \right] \delta q_2 \right) dt = 0. \tag{75}$$

However, the Euler-Lagrange equations in the integrand are for unconstrained $q_1$ and $q_2$, so the constraint function $f$ must be employed. When the functional differential is taken on $f$ with respect to $q_1$ and $q_2$,

$$\delta f = \frac{\partial f}{\partial q_1}\delta q_1 + \frac{\partial f}{\partial q_2}\delta q_2 = 0. \tag{76}$$

Because the functional derivative of $f$ is 0, $\lambda \delta f$ may be added to the integrand, where $\lambda$ is known as

the Lagrange multiplier.

And so, $\delta S$ becomes $\delta S = \int \left( \left[ \frac{\partial L}{\partial q_1} + \lambda \frac{\partial f}{\partial q_1} - \frac{d}{dt}\left( \frac{\partial L}{\partial \dot{q}_1} \right) \right] \delta q_1 + \left[ \frac{\partial L}{\partial q_2} + \lambda \frac{\partial f}{\partial q_2} - \frac{d}{dt}\left( \frac{\partial L}{\partial \dot{q}_2} \right) \right] \delta q_2 \right) dt = 0.$

This leads to the following final result to minimize $S$:

$$-\left[ \frac{\partial L}{\partial q_1} - \frac{d}{dt}\left( \frac{\partial L}{\partial \dot{q}_1} \right) \right] = \lambda \frac{\partial f}{\partial q_1} \tag{77}$$

$$-\left[ \frac{\partial L}{\partial q_2} - \frac{d}{dt}\left( \frac{\partial L}{\partial \dot{q}_2} \right) \right] = \lambda \frac{\partial f}{\partial q_2}. \tag{78}$$

In the context of liquid crystals, we want to minimize $\mathcal{F}$, the total free energy with respect to director alignment, which, analogous to a Lagrangian, is the free energy density integrated over volume element $d\tau$ with the coordinates of director components. That is, we want to find the molecular alignment at which the system resides in an energetically favorable state. In this case, our system is constrained by the total magnitude of a director:

$$n^2 = n_x^2 + n_y^2 + n_z^2 = 1, \tag{79}$$

if we consider the Cartesian coordinates. Subsequently, the components of the molecular field $\mathbf{H}$ can be shown to be related to the components of the director by

$$H_i = \lambda n_i, \tag{80}$$

which shows that the molecular field must align with the director field in equilibrium.

Let's now consider an incompressible liquid crystal in the static regime. When there is a small change in the change of the director field with respect with respect to position due to the directors changing their position by a rotational displacement $\mathbf{u}$ , the total free energy of the system $\delta\mathcal{F}$ changes as well. Thus, the two conditions arise

$$\mathbf{r'} = \mathbf{r} + \mathbf{u} \tag{81}$$

$$\hat{n}'(\mathbf{r}') = \hat{n}(\mathbf{r}), \tag{82}$$

where $\hat{n}'$ is the orientation of the director field after displacement, which should not be different than $\hat{n}$, and $\mathbf{r}'$ is the change in the position vector due to the rotational displacement [27]. When these

equations are differentiated with respect to $\mathbf{r}'$,

$$\partial_{r'_j} r_k = \partial_{r'_j} r'_k - \partial_{r'_j} u_k \approx \delta^j_k - \partial_{r_j} u_k \tag{83}$$

$$\partial_{r'_j} n'_i = (\partial_{r_k} n_i)(\partial_{r'_j} r_k), \tag{84}$$

where the approximation can be made in Eq. 83 due to a first-order approximation in $\mathbf{u}$. By placing Eq. 83 into Eq. 84, we see that

$$\partial_{r'_j} n'_i = (\partial_{r_k} n_i)(\delta^j_k - \partial_{r_j} u_k) = \partial_{r_j} n_i - (\partial_{r_k} n_i)(\partial_{r_j} u_k), \tag{85}$$

which can be rewritten as

$$\partial_{r'_j} n'_i - \partial_{r_j} n_i = -(\partial_{r_k} n_i)(\partial_{r_j} u_k). \tag{86}$$

Note that because $\mathbf{u}$ is a small displacement, this equation is the formula for a small change in the change of the director field with respect to position, $\delta n^j_i$. And so, when examining $\delta\mathcal{F}$ due to this rotational displacement of the directors,

$$\delta\mathcal{F} = \int d\tau \delta F = \int d\tau \delta n^j_i \frac{\delta F}{\delta n^j_i} = \int d\tau \frac{\delta F}{\delta n^j_i}(-\partial_{r_k} n_i)(\partial_{r_j} u_k) = -\int d\tau \frac{\delta F}{\delta n^j_i} n^k_i (\partial_{r_j} u_k). \tag{87}$$

However, due to the incompressibility of the fluid,

$$\nabla \cdot \mathbf{u} = 0. \tag{88}$$

This equation leads to a constraint on the $n^j_i$ variables with the Lagrange multiplier turing out to be the pressure within the fluid $p(\mathbf{r})$ which reduces the total free energy of the system [27]. Then

$$\delta\mathcal{F} = -\int d\tau \left[\frac{\delta F}{\delta n^j_i} n^k_i (\partial_{r_j} u_k) + p(\mathbf{r})\delta^k_j (\nabla \cdot \mathbf{u})\right]. \tag{89}$$

By factoring out $\partial_{r_j} u_k = \nabla \cdot \mathbf{u}$, one arrives at the stress tensor for a static liquid crystal without a viscous flow of ionic impurities

$$T^k_j = -\left[\frac{\delta F}{\delta n^j_i} n^k_i + p(\mathbf{r})\delta^k_j\right]. \tag{90}$$

### Measuring the Thickness $d$ of Sample

Transmittance of light through the empty cells is a property that can be measured with the Ocean Optics spectrometer, shown in Fig. A1. The cell is placed in the stand that features incoming light from a halogen lamp via a fiber optic cable and a stand with another fiber optic cable that detects the light passed through the cell.

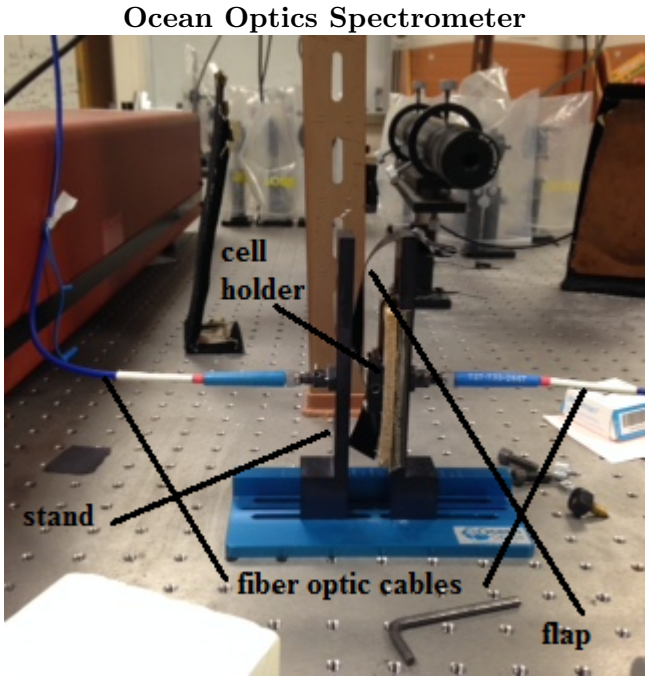


**Figure A1.** The empty cell fits between the two clips shown on the right stand. The flap is used for detecting and erasing background noise for the spectra. Light from the halogen lamp enters through the right fiber optic cable and is detected through transmission through the left fiber optic cable.

Before the empty cell is placed between the stands, the spectrometer must be calibrated. This is done through the SpectraSuite software. After the lamp is turned on, the bright light bulb icon is selected to tell the machine that it should acknowledge the detected signal as coming from the halogen lamp and from noise. A flap is then placed in front of the aperture of the lamp light before selecting the dark light bulb icon. This tells the detector to acknowledge the signal as coming from noise only. Noise is then erased from the signal by selecting the dark light-bulb icon with the minus sign in front of it. The sample is then placed in the stand, and the flap is subsequently removed. The "T" icon is then selected to display the percent of light transmitted through the cell at various wavelengths. A pattern of maxima of light at various wavelengths should then be displayed on the transmittance

spectrum. This pattern is due to the phase difference between a ray of transmitted light of wavelength $\lambda_n$ and a ray of that wavelength that has been reflected by both slides of the cell. As it reflects off both slides, it takes on a path difference given by $2d$, where $d$ is the thickness of the cell. Thus, for constructive interference between two rays of light with wavelength $\lambda_n$, the phase difference must meet the following condition:

$$\left(\frac{2\pi}{\lambda_n}\right)2d = 2n\pi, \tag{91}$$

where $n$ is an integer. This leads to the following formula for a maximum of wavelength $\lambda_n$:

$$2d = n\lambda_n. \tag{92}$$

Similarly, for an adjacent peak of wavelength $\lambda_{n+1}$,

$$2d = (n+1)\lambda_{n+1}. \tag{93}$$

Using the previous two equations, we see that

$$\frac{2d}{\lambda_{n+1}} = \frac{2d}{\lambda_n} + 1. \tag{94}$$

This equation can be rearranged into the following form:

$$d = \frac{1}{2}\left(\frac{\lambda_{n+1}\lambda_n}{\lambda_n - \lambda_{n+1}}\right). \tag{95}$$

And so, when the wavelengths of two adjacent peaks are recorded, the thickness of the empty cell can be measured.

### Spectral Leakage

As mentioned in the "Results & Analysis" section, spectral leakage is the undesired effect of a distribution of peaks surrounding the measured harmonic as shown in Fig. 21. This comes from the algorithm terminating its sampling of input data when the time-domain waveform has not completed an entire period [28,29].

A conceptual way of understanding this requires consideration of the sampling rate $f_s$, which is

related to the period of sampling $\Delta t$ by

$$\Delta t = \frac{1}{f_s}, \tag{96}$$

which also influences the frequency quantum, or the width of a frequency bin [29]. The frequency of the $k$-th bin ($f_k$) is given by,

$$f_k = \frac{k}{N\Delta t}, \tag{97}$$

where $N$ is the total number of data points collected [28,29]. Thus, consider the case explained by Lyon [29], where $N = 2048$ and $f_s = 8000$Hz. This implies that if the waveform has a frequency of 400Hz, it would have a nonzero peak in the

$$k = 2048 * (400\text{Hz})/(8000\text{Hz}) = 102.4 \tag{98}$$

bin; however, because we are dealing with quantized bins, $k$ should be an integer [29]. Thus, the narrow uncertainty in waveform's frequency will cause a noticeable distribution of peaks around the 102-nd and 103-rd bin, reducing the frequency resolution.

A more rigorous approach of understanding this involves a look at discrete Fourier transforms and the convolution theorem. The discrete Fourier transform ($\mathcal{F}$) of $N$ samples ($x(n)$) $X_k = \mathcal{F}(x(n))$ is given by

$$X_k = \sum_{n=-N/2}^{(N/2)-1} x(n) e^{-j2\pi kn/N}, \tag{99}$$

where $k = 0, 1, ..., N-1$ and $j$ is an imaginary number. When an FFT algorithm is conducted, we assume that it is mixed with a square wave with an amplitude of 1 within the sampling period and 0 elsewhere [28,29]. This signal is known as a rectangular window $w(n)$ and contributes to spectral leakage, as it is convolved with $x(n)$, meaning that their FFT's are multiplied together [28,29]. Unfortunately, the Fourier transform of a rectangular wave is the sinc function ($\sin(x)/x$), which permits the distribution of peaks shown in Fig. 21 [28,29].

A solution to spectral leakage involves Hann windowing [29], i.e. mixing the received signal with

$$w(n) = \frac{1}{2}\left[1 - \cos\left(\frac{2\pi n}{N-1}\right)\right], \tag{100}$$

where $w(n)$ is displayed in Fig. A2. Such a window, mixed with the time-domain waveform, zeros the

end points of the sampling period, where the wave is not given a chance to complete an entire period [29]. The effect of spectral leakage is therefore diminished, allowing strong frequency resolution.

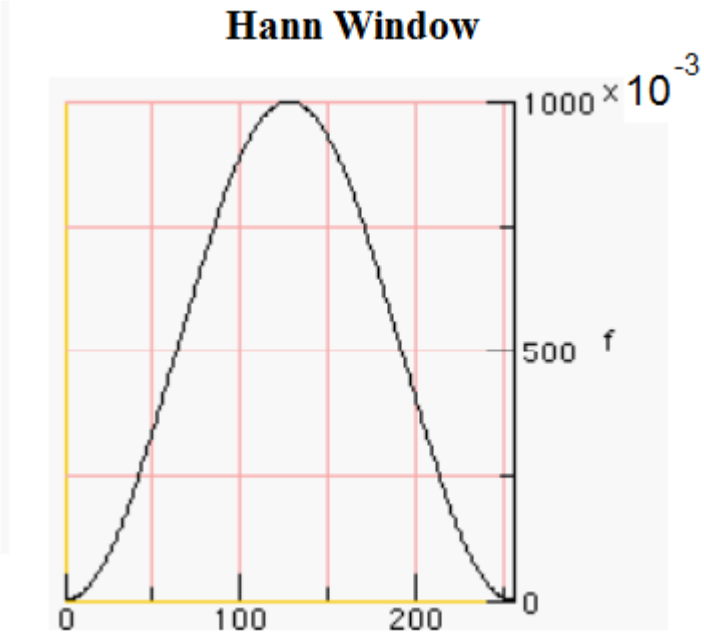


**Figure A2.** The Von Hann window for approximately 250 samples (f is measured in arbitrary units)[29].

### Laser Diffraction Results on Cell C

**Figure A3.** FFT power spectra collected on LC cell C are presented below. Note that these graphs are not averaged.

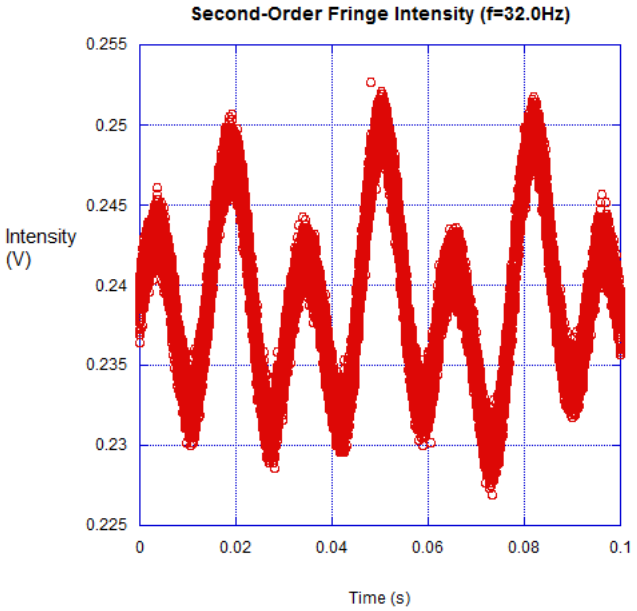
Second-Order Fringe Intensity (f=32.0Hz)
Intensity (V)
0.255
0.25
0.245
0.24
0.235
0.23
0.225
0
0.02
0.04
0.06
0.08
0.1
Time (s)

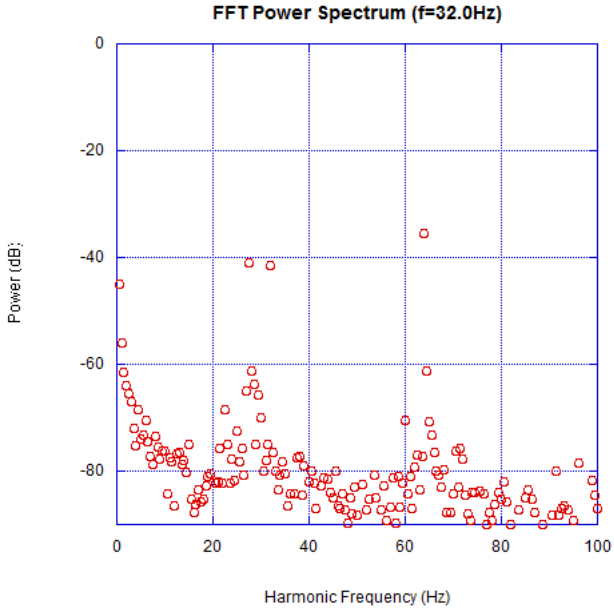
FFT Power Spectrum (f=32.0Hz)
Power (dB)
0
-20
-40
-60
-80
0
20
40
60
80
100
Harmonic Frequency (Hz)

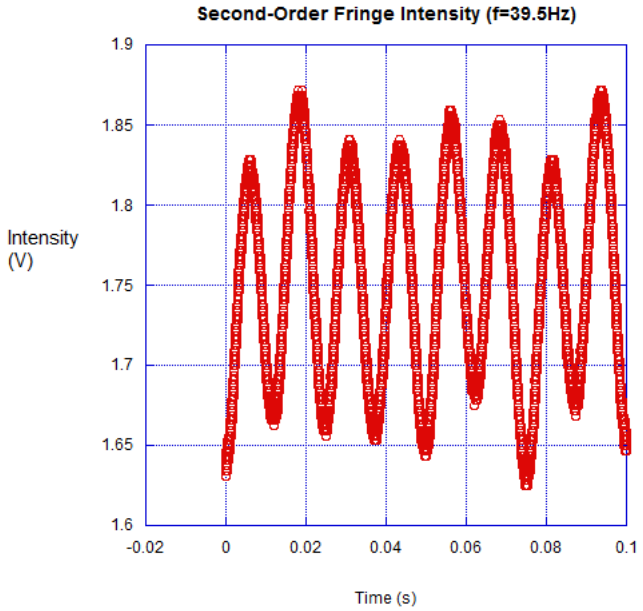
Second-Order Fringe Intensity (f=39.5Hz)
Intensity (V)
1.9
1.85
1.8
1.75
1.7
1.65
1.6
-0.02
0
0.02
0.04
0.06
0.08
0.1
Time (s)

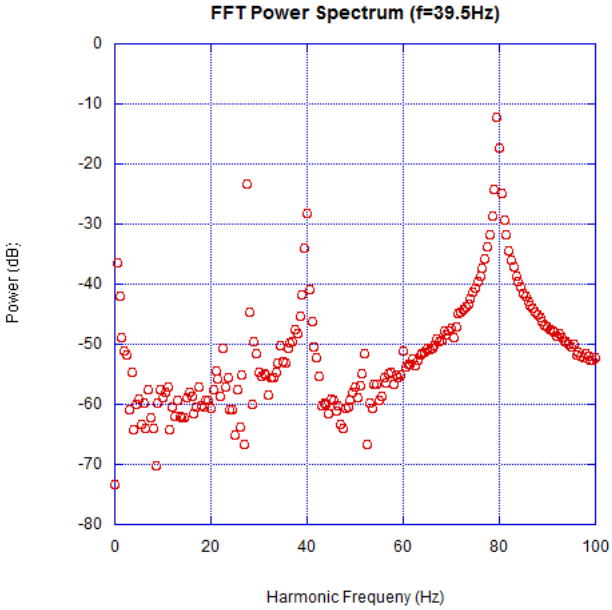
FFT Power Spectrum (f=39.5Hz)
Power (dB)
0
-10
-20
-30
-40
-50
-60
-70
-80
0
20
40
60
80
100
Harmonic Frequeny (Hz)

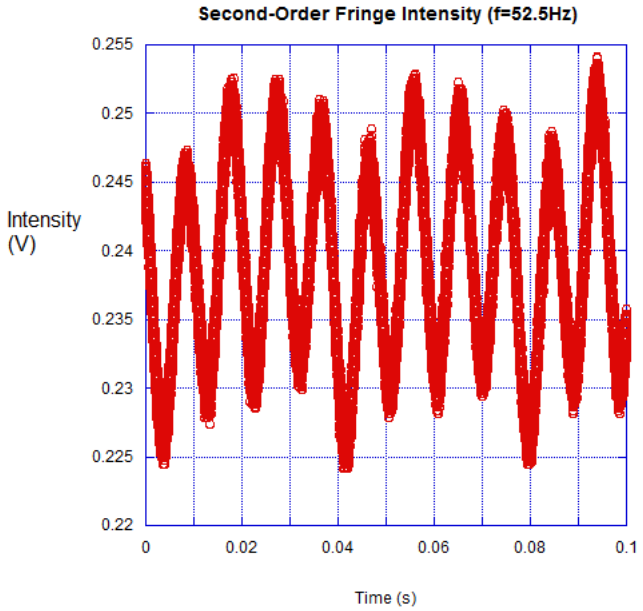
Second-Order Fringe Intensity (f=52.5Hz)
Intensity (V)
0.255
0.25
0.245
0.24
0.235
0.23
0.225
0.22
0
0.02
0.04
0.06
0.08
0.1
Time (s)

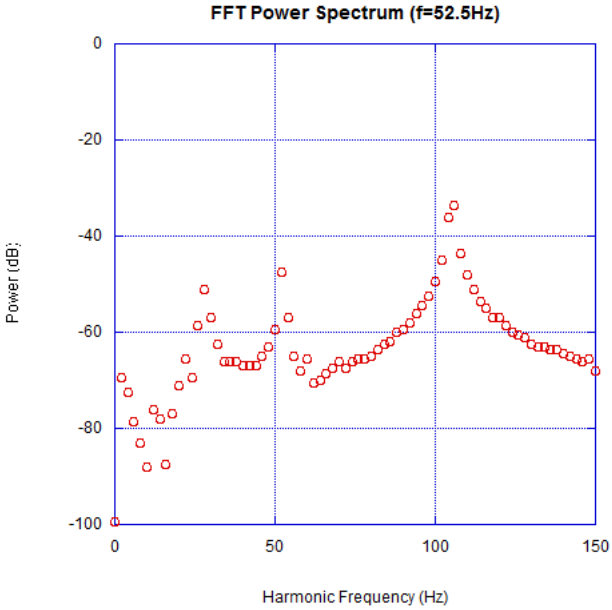
FFT Power Spectrum (f=52.5Hz)
Power (dB)
0
-20
-40
-60
-80
-100
0
50
100
150
Harmonic Frequency (Hz)

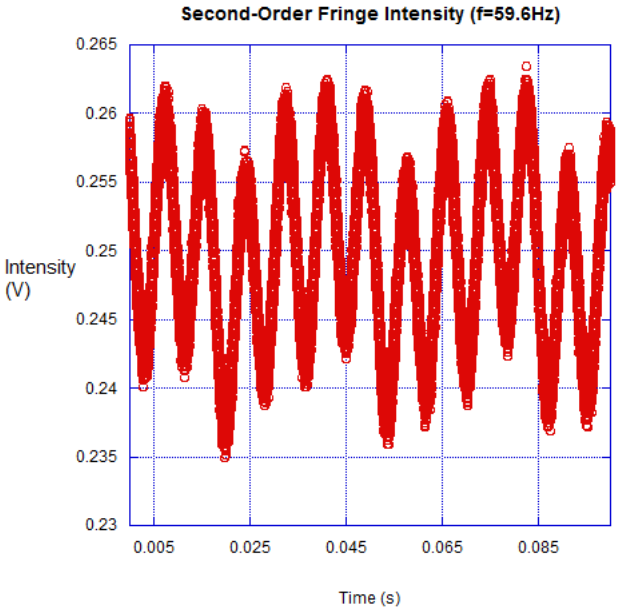
Second-Order Fringe Intensity (f=59.6Hz)
Intensity (V)
0.265
0.26
0.255
0.25
0.245
0.24
0.235
0.23
0.005
0.025
0.045
0.065
0.085
Time (s)

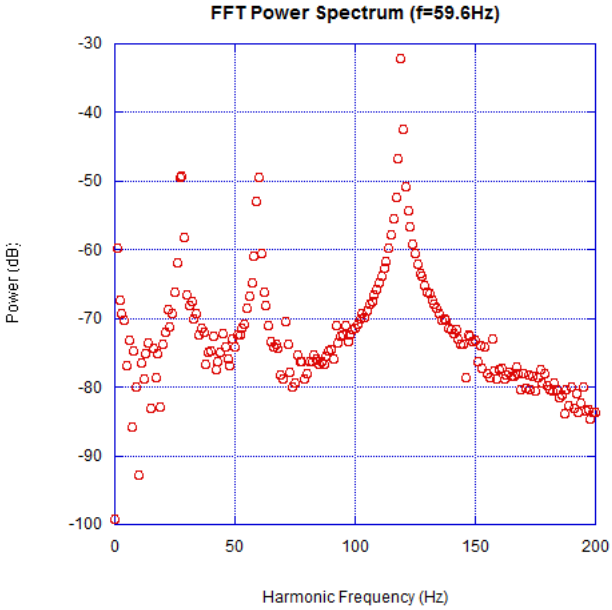
FFT Power Spectrum (f=59.6Hz)
Power (dB)
-30
-40
-50
-60
-70
-80
-90
-100
0
50
100
150
200
Harmonic Frequency (Hz)

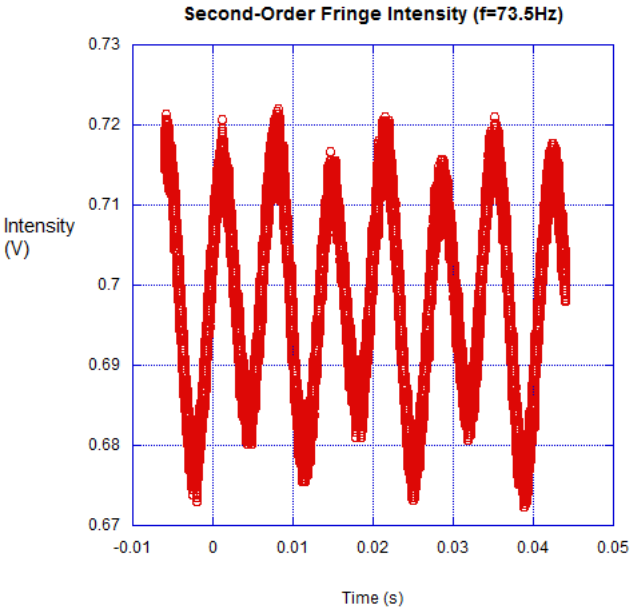
Second-Order Fringe Intensity (f=73.5Hz)
Intensity (V)
0.73
0.72
0.71
0.7
0.69
0.68
0.67
-0.01
0
0.01
0.02
0.03
0.04
0.05
Time (s)

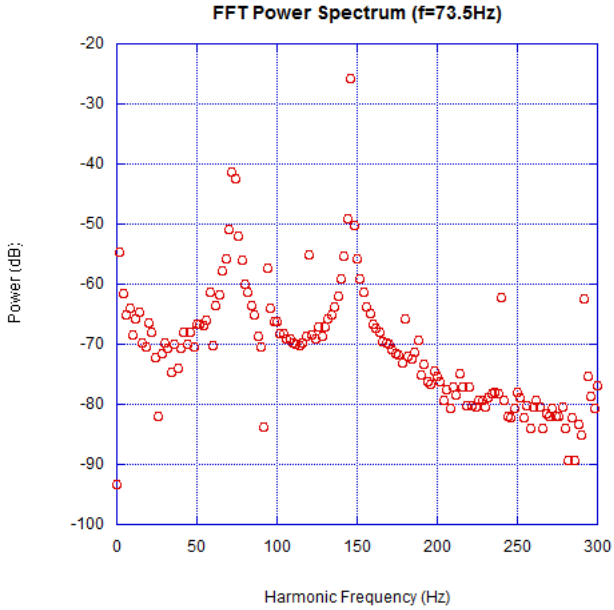
FFT Power Spectrum (f=73.5Hz)
Power (dB)
-20
-30
-40
-50
-60
-70
-80
-90
-100
0
50
100
150
200
250
300
Harmonic Frequency (Hz)

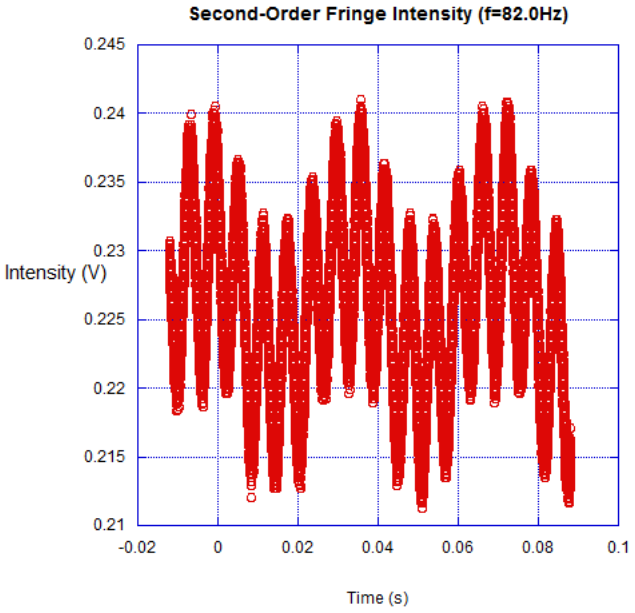
Second-Order Fringe Intensity (f=82.0Hz)
Intensity (V)
0.245
0.24
0.235
0.23
0.225
0.22
0.215
0.21
-0.02
0
0.02
0.04
0.06
0.08
0.1
Time (s)

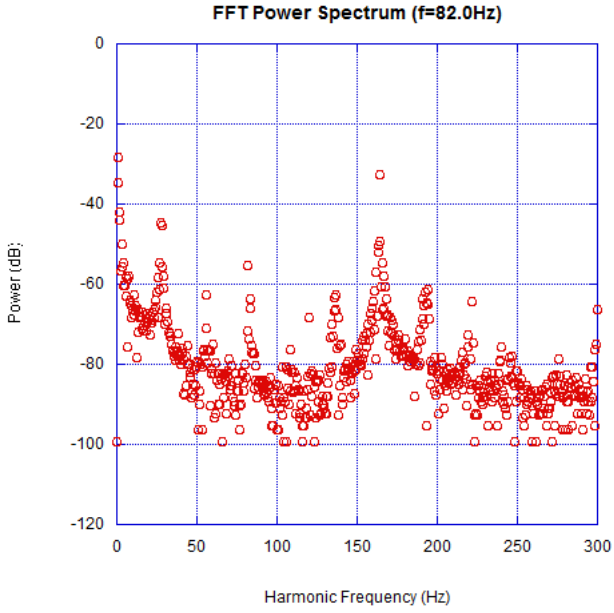
FFT Power Spectrum (f=82.0Hz)
Power (dB)
0
-20
-40
-60
-80
-100
-120
0
50
100
150
200
250
300
Harmonic Frequency (Hz)

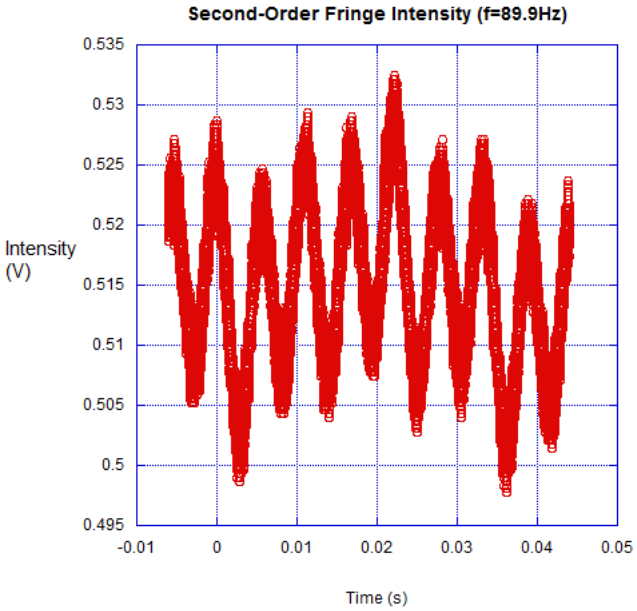
Second-Order Fringe Intensity (f=89.9Hz)
Intensity (V)
0.535
0.53
0.525
0.52
0.515
0.51
0.505
0.5
0.495
-0.01
0
0.01
0.02
0.03
0.04
0.05
Time (s)

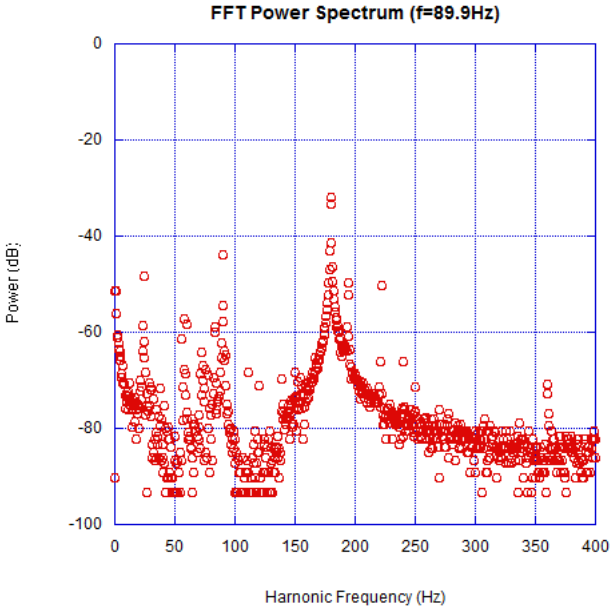
FFT Power Spectrum (f=89.9Hz)
Power (dB)
0
-20
-40
-60
-80
-100
0
50
100
150
200
250
300
350
400
Harmonic Frequency (Hz)

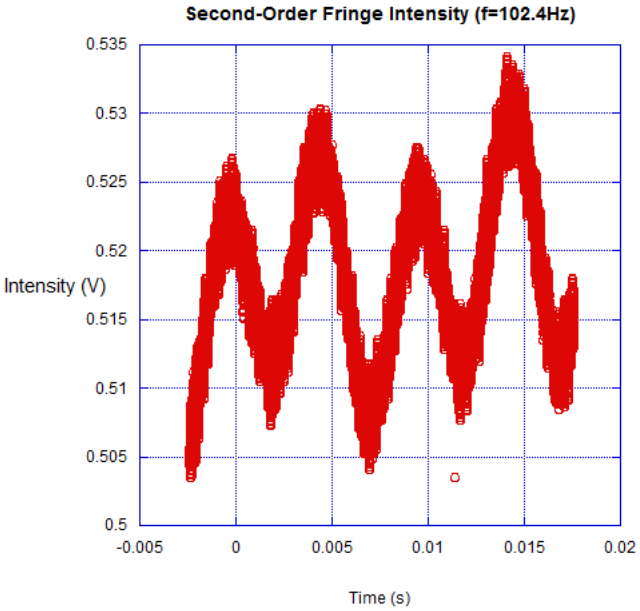
Second-Order Fringe Intensity (f=102.4Hz)
Intensity (V)
0.535
0.53
0.525
0.52
0.515
0.51
0.505
0.5
-0.005
0
0.005
0.01
0.015
0.02
Time (s)

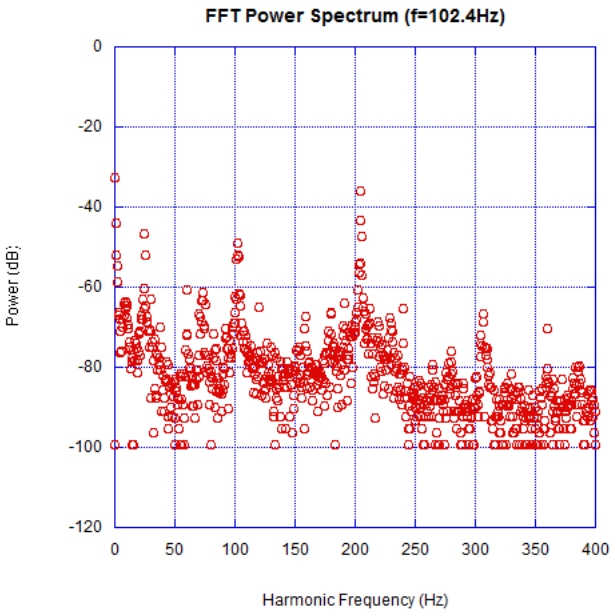
FFT Power Spectrum (f=102.4Hz)
Power (dB)
0
-20
-40
-60
-80
-100
-120
0
50
100
150
200
250
300
350
400
Harmonic Frequency (Hz)

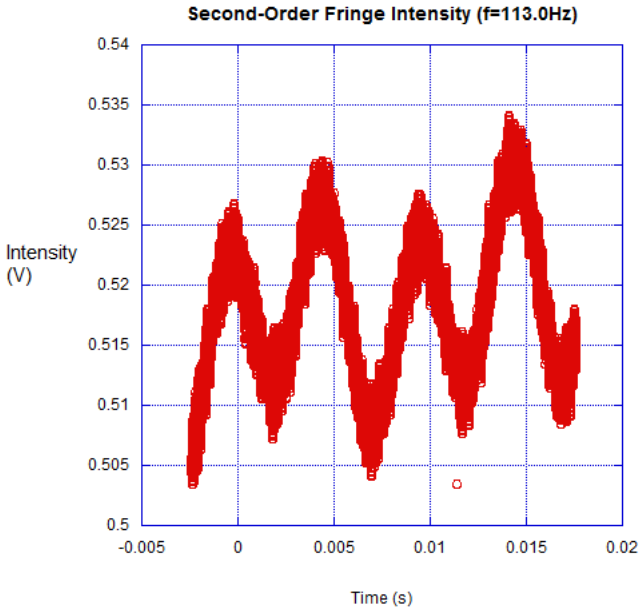
Second-Order Fringe Intensity (f=113.0Hz)
Intensity (V)
0.54
0.535
0.53
0.525
0.52
0.515
0.51
0.505
0.5
-0.005
0
0.005
0.01
0.015
0.02
Time (s)

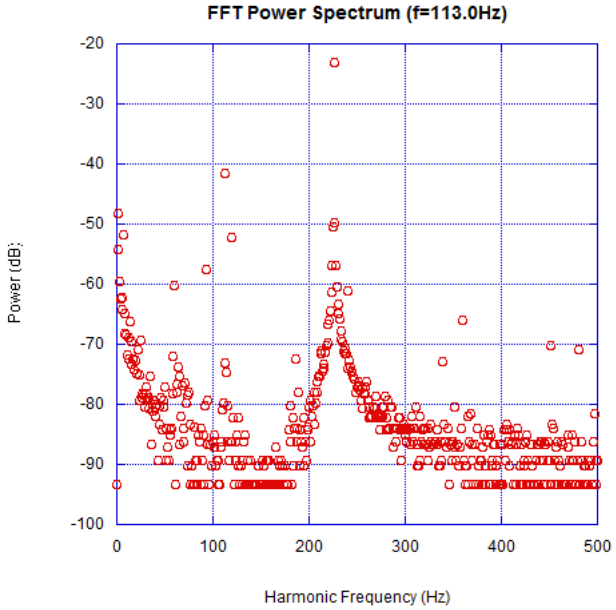
FFT Power Spectrum (f=113.0Hz)
Power (dB)
-20
-30
-40
-50
-60
-70
-80
-90
-100
0
100
200
300
400
500
Harmonic Frequency (Hz)

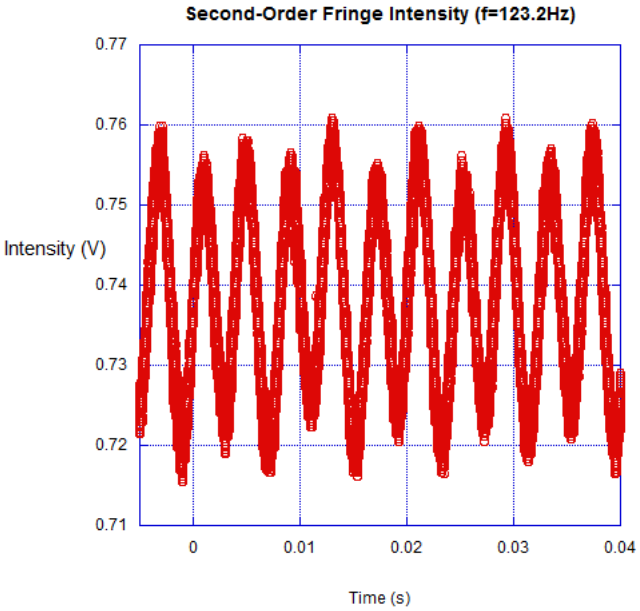
Second-Order Fringe Intensity (f=123.2Hz)
Intensity (V)
0.77
0.76
0.75
0.74
0.73
0.72
0.71
0
0.01
0.02
0.03
0.04
Time (s)

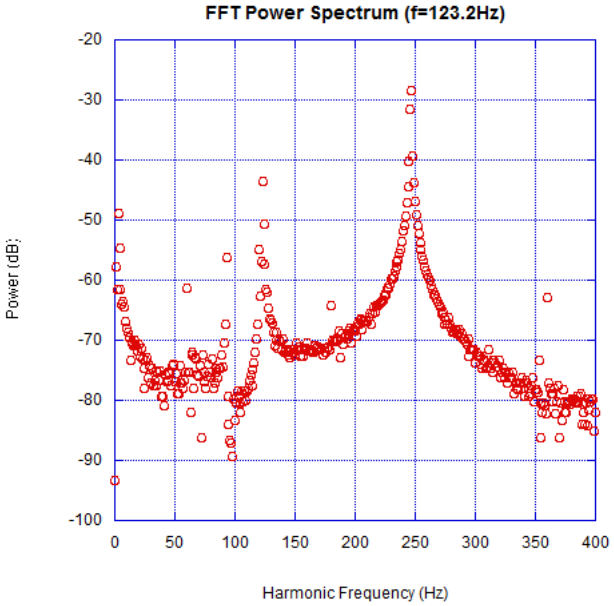
FFT Power Spectrum (f=123.2Hz)
Power (dB)
-20
-30
-40
-50
-60
-70
-80
-90
-100
0
50
100
150
200
250
300
350
400
Harmonic Frequency (Hz)

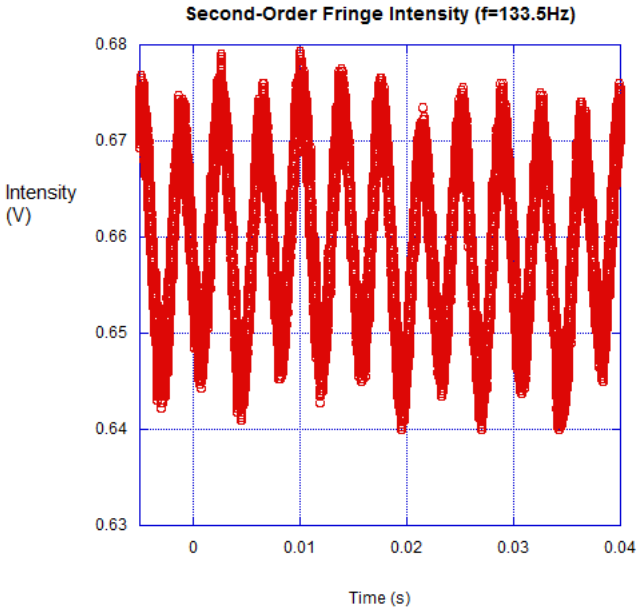
Second-Order Fringe Intensity (f=133.5Hz)
Intensity (V)
0.68
0.67
0.66
0.65
0.64
0.63
0
0.01
0.02
0.03
0.04
Time (s)

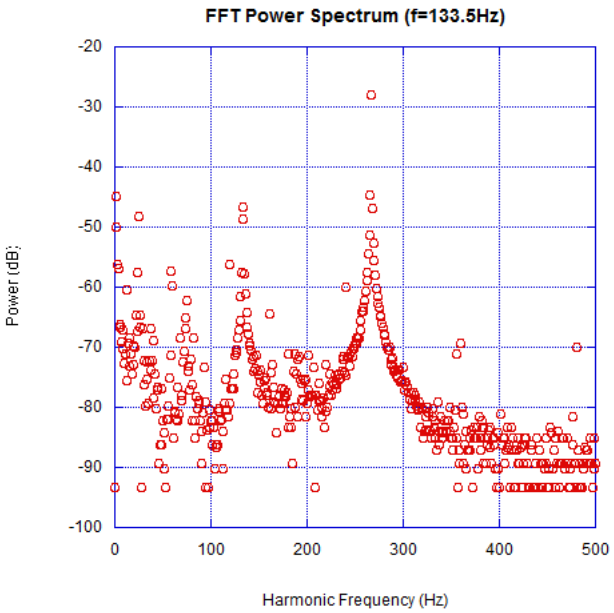
FFT Power Spectrum (f=133.5Hz)
Power (dB)
-20
-30
-40
-50
-60
-70
-80
-90
-100
0
100
200
300
400
500
Harmonic Frequency (Hz)

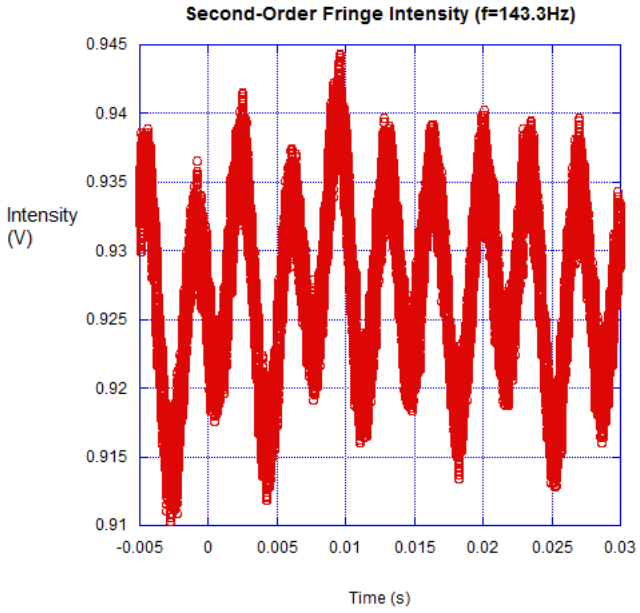
Second-Order Fringe Intensity (f=143.3Hz)
Intensity (V)
0.945
0.94
0.935
0.93
0.925
0.92
0.915
0.91
-0.005
0
0.005
0.01
0.015
0.02
0.025
0.03
Time (s)

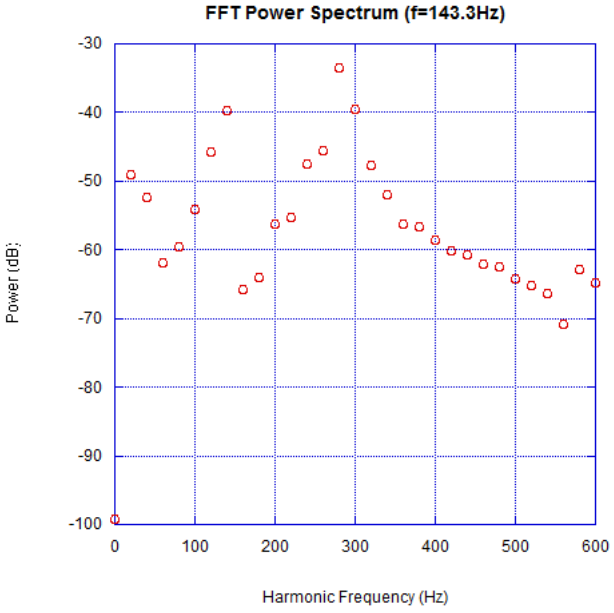
FFT Power Spectrum (f=143.3Hz)
Power (dB)
-30
-40
-50
-60
-70
-80
-90
-100
0
100
200
300
400
500
600
Harmonic Frequency (Hz)

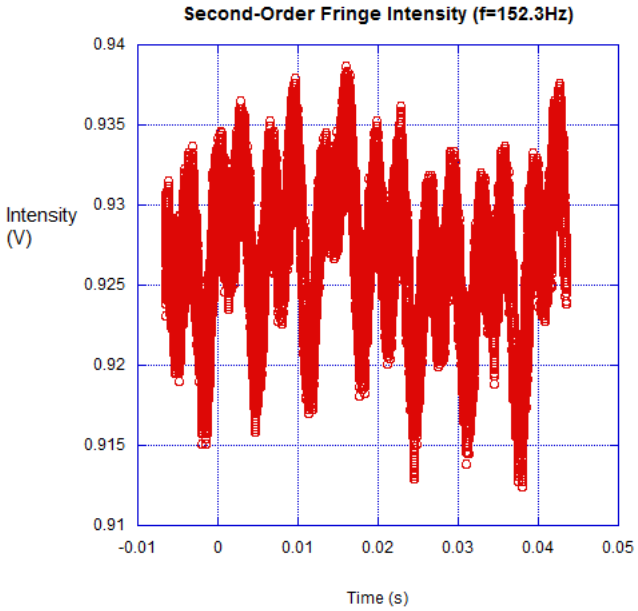
Second-Order Fringe Intensity (f=152.3Hz)
Intensity (V)
0.94
0.935
0.93
0.925
0.92
0.915
0.91
-0.01
0
0.01
0.02
0.03
0.04
0.05
Time (s)

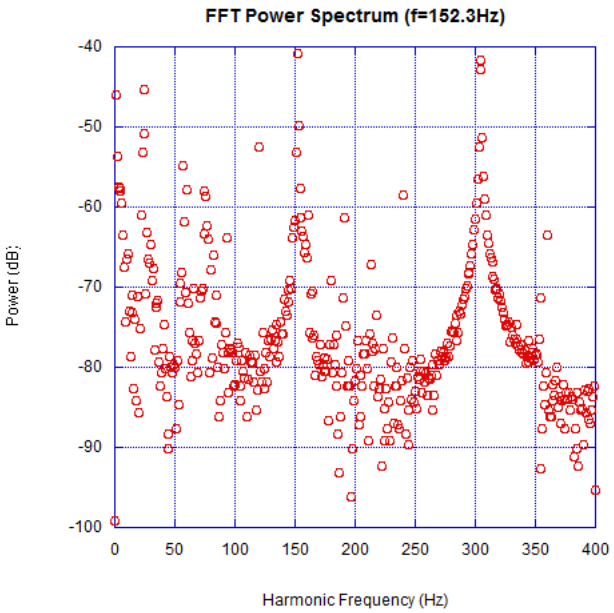
FFT Power Spectrum (f=152.3Hz)
Power (dB)
-40
-50
-60
-70
-80
-90
-100
0
50
100
150
200
250
300
350
400
Harmonic Frequency (Hz)

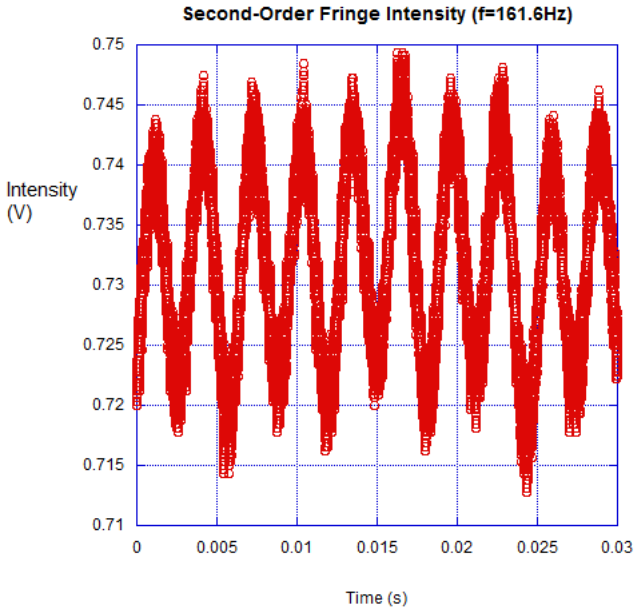
Second-Order Fringe Intensity (f=161.6Hz)
Intensity (V)
0.75
0.745
0.74
0.735
0.73
0.725
0.72
0.715
0.71
0
0.005
0.01
0.015
0.02
0.025
0.03
Time (s)

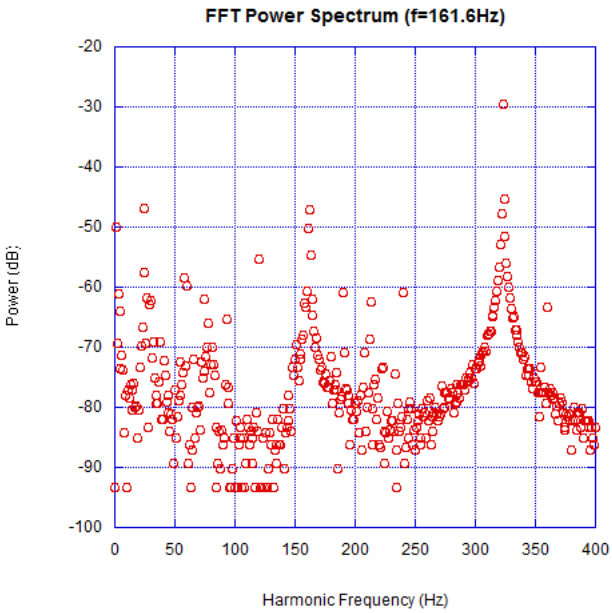
FFT Power Spectrum (f=161.6Hz)
Power (dB)
-20
-30
-40
-50
-60
-70
-80
-90
-100
0
50
100
150
200
250
300
350
400
Harmonic Frequency (Hz)

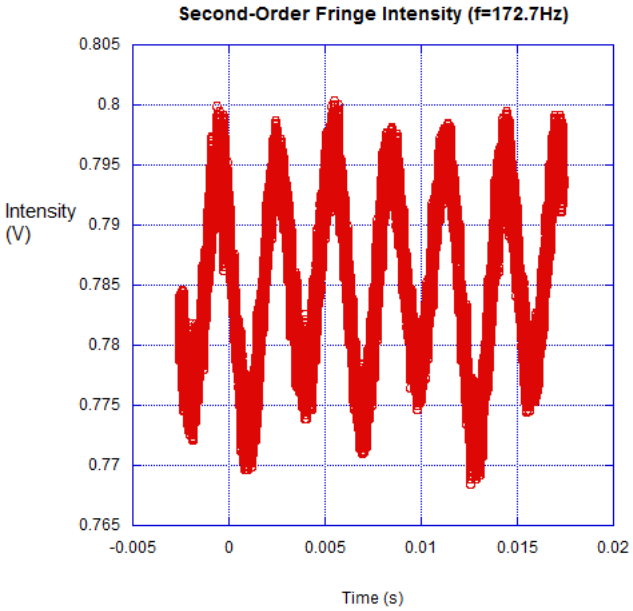
Second-Order Fringe Intensity (f=172.7Hz)
Intensity (V)
0.805
0.8
0.795
0.79
0.785
0.78
0.775
0.77
0.765
-0.005
0
0.005
0.01
0.015
0.02
Time (s)

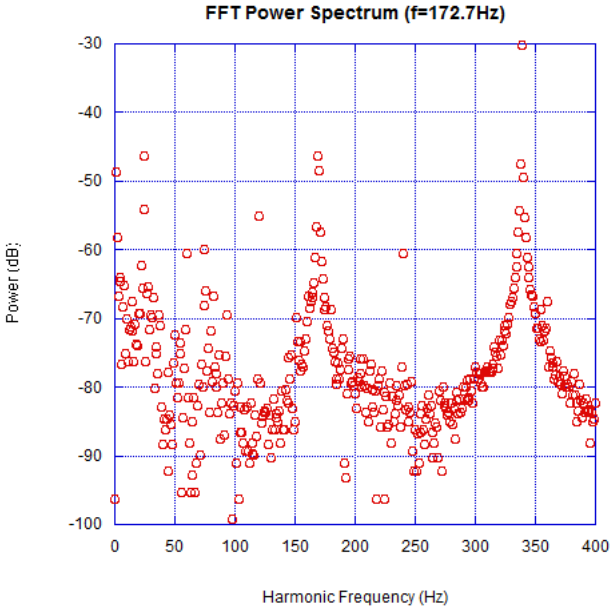
FFT Power Spectrum (f=172.7Hz)
Power (dB)
-30
-40
-50
-60
-70
-80
-90
-100
0
50
100
150
200
250
300
350
400
Harmonic Frequency (Hz)

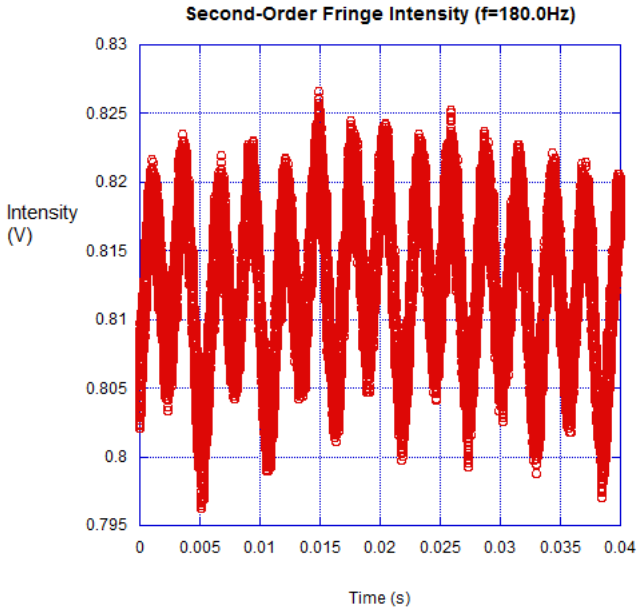
Second-Order Fringe Intensity (f=180.0Hz)
Intensity (V)
0.83
0.825
0.82
0.815
0.81
0.805
0.8
0.795
0
0.005
0.01
0.015
0.02
0.025
0.03
0.035
0.04
Time (s)

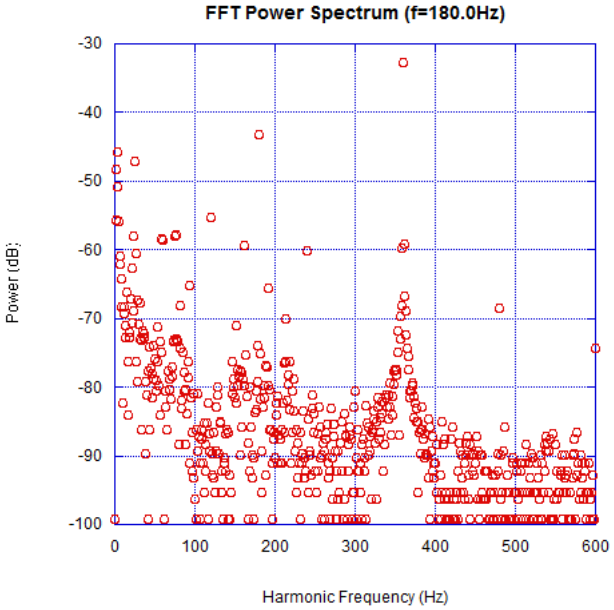
FFT Power Spectrum (f=180.0Hz)
Power (dB)
-30
-40
-50
-60
-70
-80
-90
-100
0
100
200
300
400
500
600
Harmonic Frequency (Hz)

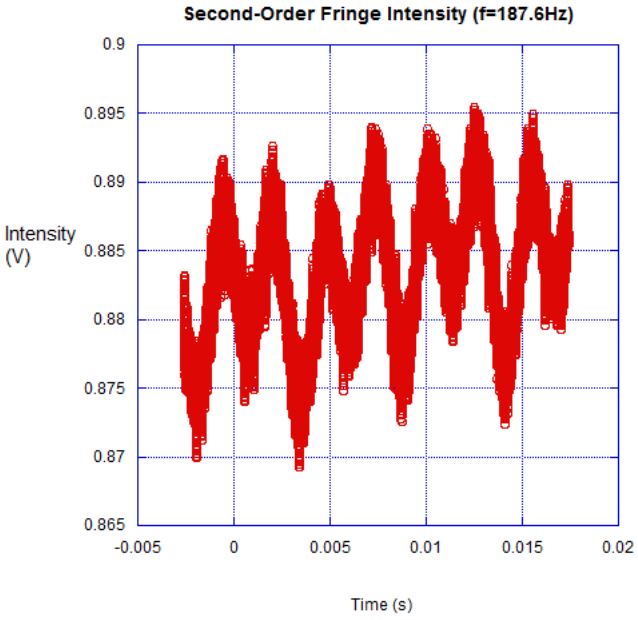


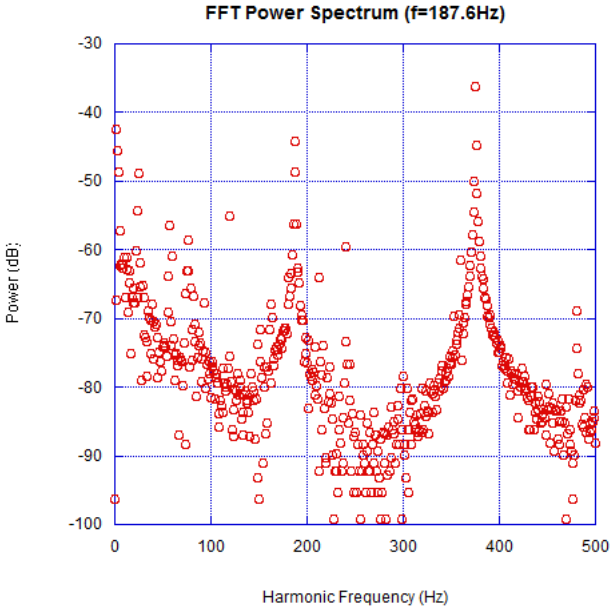


## Laser Diffraction Results on Cell A (Rectangular Windowed)

**Figure A4.** FFT power spectra collected on LC cell A are presented below. These spectra are summed-averaged for 1000 sweeps and multiplied by a Hann window. The measured harmonics are as follows with FWHM uncertainties (1) $f = 20.75 \pm 4.0$Hz, $2f = 39.75 \pm 4.0$Hz, $3f = 59.75 \pm 5.0$Hz, and $4f =$

$81.75\pm5.0$Hz (2) $f = 59.5\pm5.0$Hzand $2f = 124.5\pm10.0$Hz, (3) $f = 69.5\pm10.0$Hz and $2f = 139.5\pm10.0$Hz (4) $f = 99.5 \pm 10.0$Hz and $2f = 204.5 \pm 5.0$Hz (5) $f = 119.5 \pm 5.0$Hz and $2f = 244.5 \pm 8.0$Hz (6) $f = 139.5 \pm 5.0$Hz and $2f = 284.5 \pm 5.0$Hz(7) $f = 159.5 \pm 10.0$Hz and $2f = 319.5 \pm 10.0$Hz(8) $f = 179.5 \pm 5.0$Hz and $2f = 359.5 \pm 8.0$Hz(9) $f = 194.5 \pm 8.0$Hz and $2f = 394.5 \pm 10.0$Hz

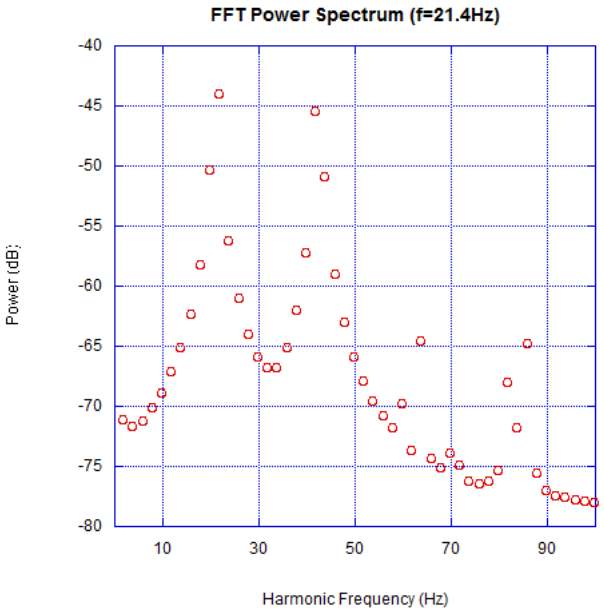


(1)

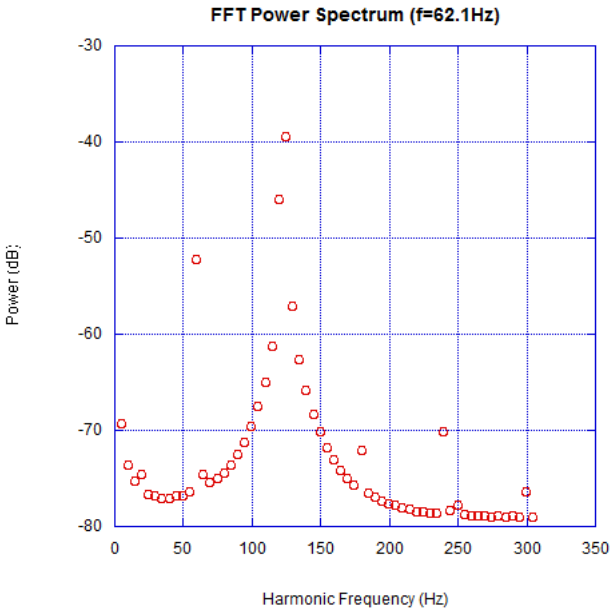

(2)

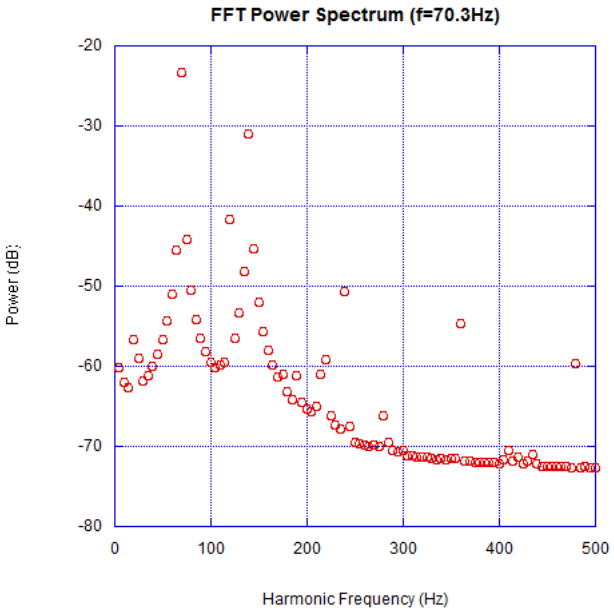
FFT Power Spectrum (f=70.3Hz)
Power (dB)
-20
-30
-40
-50
-60
-70
-80
0
100
200
300
400
500
Harmonic Frequency (Hz)

(3)

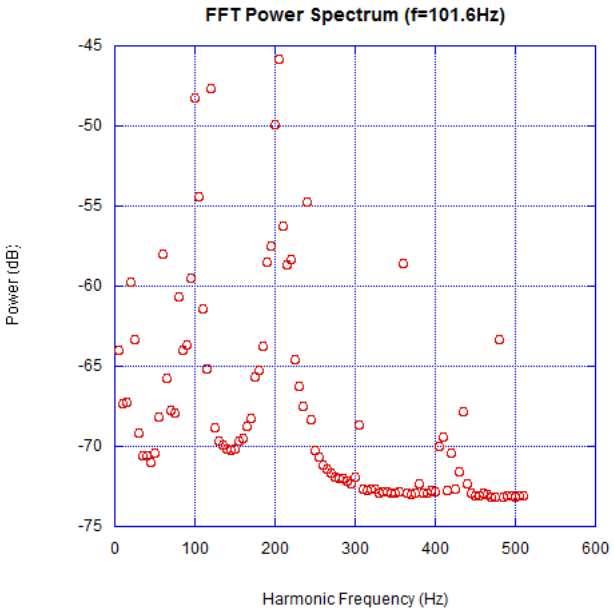
FFT Power Spectrum (f=101.6Hz)
Power (dB)
-45
-50
-55
-60
-65
-70
-75
0
100
200
300
400
500
600
Harmonic Frequency (Hz)

(4)

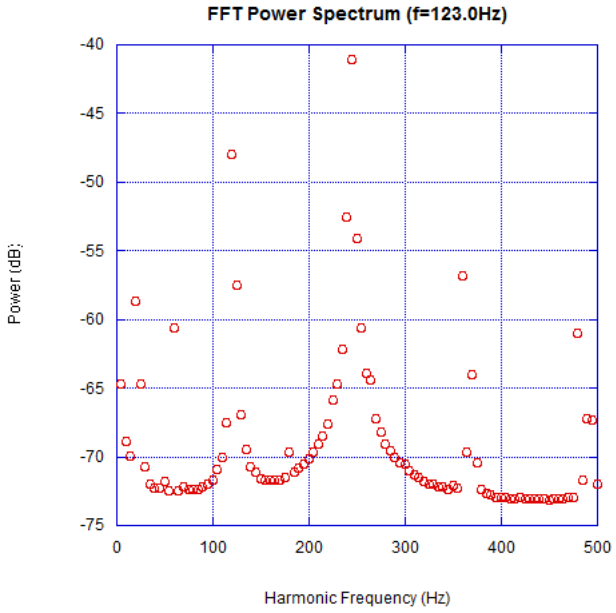
FFT Power Spectrum (f=123.0Hz)
Power (dB)
-40
-45
-50
-55
-60
-65
-70
-75
0
100
200
300
400
500
Harmonic Frequency (Hz)

(5)

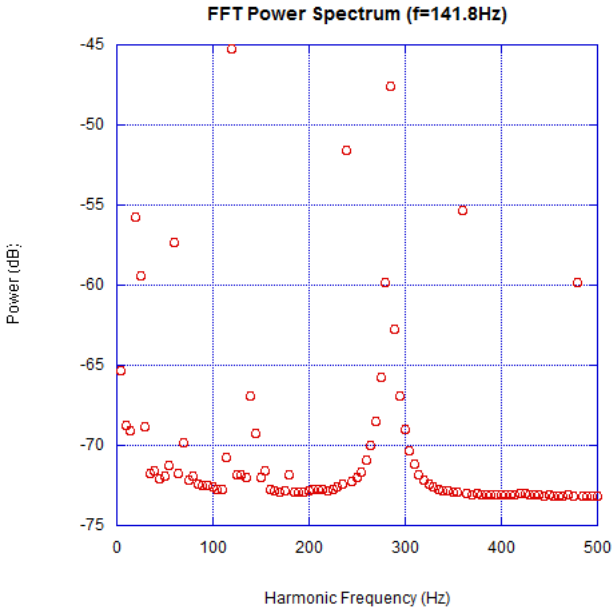
FFT Power Spectrum (f=141.8Hz)
Power (dB)
-45
-50
-55
-60
-65
-70
-75
0
100
200
300
400
500
Harmonic Frequency (Hz)

(6)

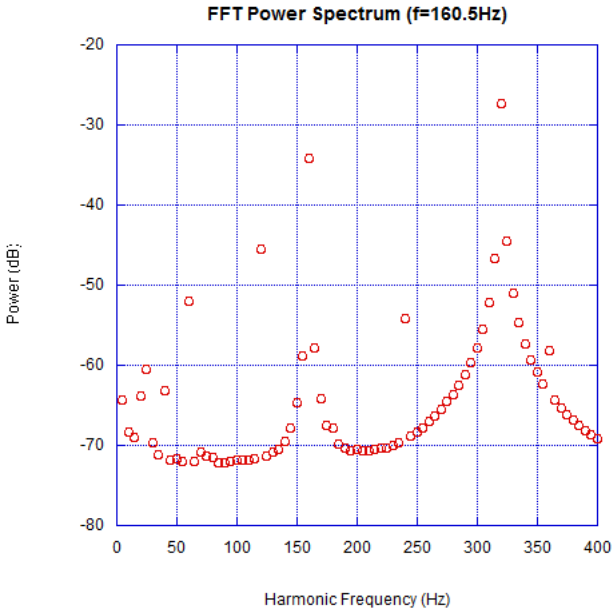
FFT Power Spectrum (f=160.5Hz)
Power (dB)
-20
-30
-40
-50
-60
-70
-80
0
50
100
150
200
250
300
350
400
Harmonic Frequency (Hz)

(7)

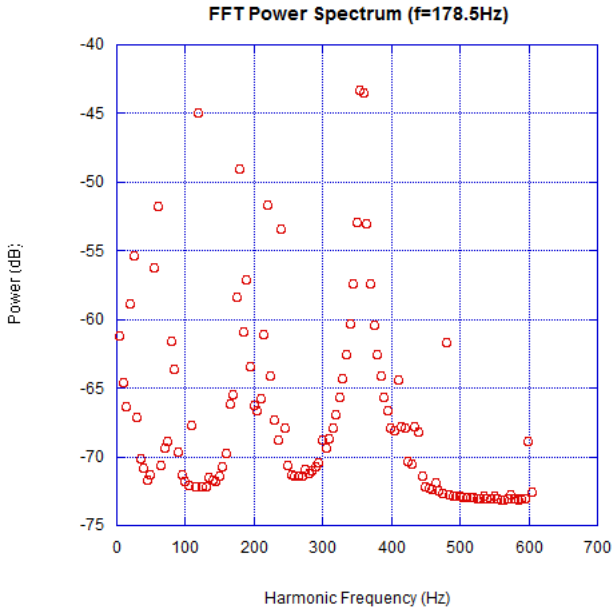
FFT Power Spectrum (f=178.5Hz)
Power (dB)
-40
-45
-50
-55
-60
-65
-70
-75
0
100
200
300
400
500
600
700
Harmonic Frequency (Hz)

(8)

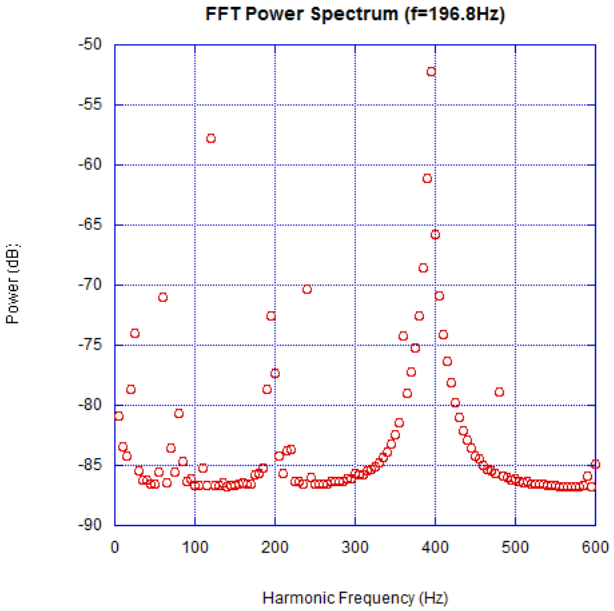


(9)

## Laser Diffraction Results on Cell A (Hann Windowed)

**Figure A5.** FFT power spectra collected on LC cell A are presented below. These spectra are summed-averaged for 1000 sweeps and multiplied by a Hann window. The measured harmonics are as follows (1) $f = 19.5 \pm 5.0$Hz, $2f = 39.5 \pm 5.0$Hz, $3f = 59.5 \pm 5.0$Hz, and $4f = 79.5 \pm 5.0$Hz (2) $f = 59.5 \pm 5.0$Hz, $2f = 119.5 \pm 5.0$Hz, $3f = 184.5 \pm 5.0$Hz, and $4f = 244.5 \pm 5.0$Hz (3) $f = 69.5 \pm 5.0$Hz and $2f = 139.5 \pm 5.0$Hz (4) $f = 119.5 \pm 5.0$Hz, $2f = 204.5 \pm 5.0$Hz, and $4f = 409.5 \pm 5.0$Hz (5) $f = 129.5 \pm 5.0$Hz and $2f = 259.5 \pm 5.0$Hz (6) $f = 144.5 \pm 5.0$Hz and $2f = 289.5 \pm 5.0$Hz(7) $f = 154.5 \pm 5.0$Hz and $2f = 314.5 \pm 5.0$Hz(8) $f = 169.5 \pm 5.0$Hz and $2f = 344.5 \pm 5.0$Hz(9) $f = 189.5 \pm 5.0$Hz and $2f = 384.5 \pm 5.0$Hz

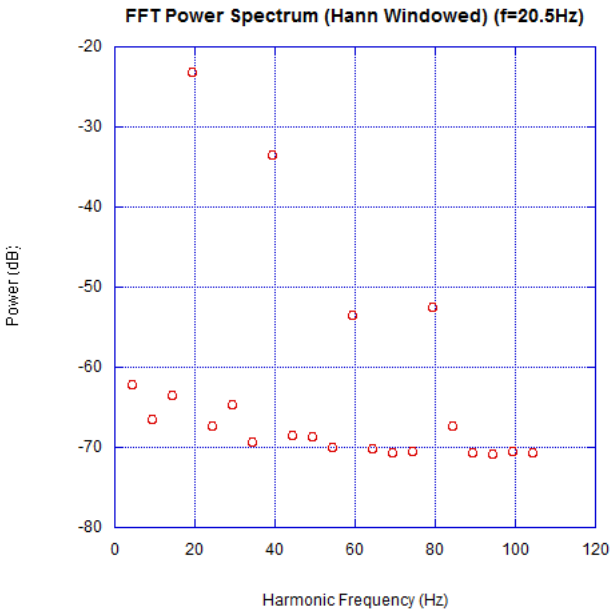
FFT Power Spectrum (Hann Windowed) (f=20.5Hz)
Power (dB)
-20
-30
-40
-50
-60
-70
-80
0
20
40
60
80
100
120
Harmonic Frequency (Hz)

(1)

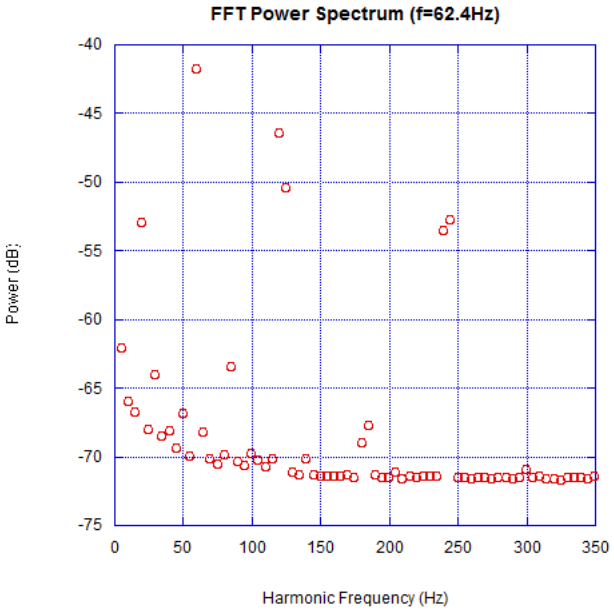
FFT Power Spectrum (f=62.4Hz)
Power (dB)
-40
-45
-50
-55
-60
-65
-70
-75
0
50
100
150
200
250
300
350
Harmonic Frequency (Hz)

(2)

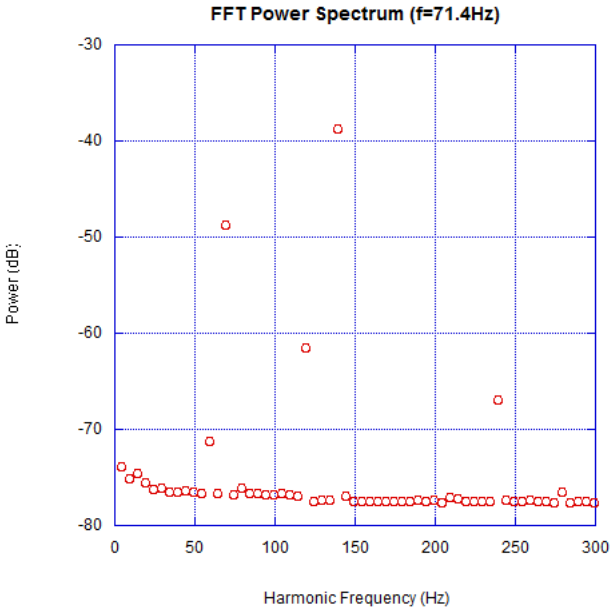
FFT Power Spectrum (f=71.4Hz)
Power (dB)
-30
-40
-50
-60
-70
-80
0
50
100
150
200
250
300
Harmonic Frequency (Hz)

(3)

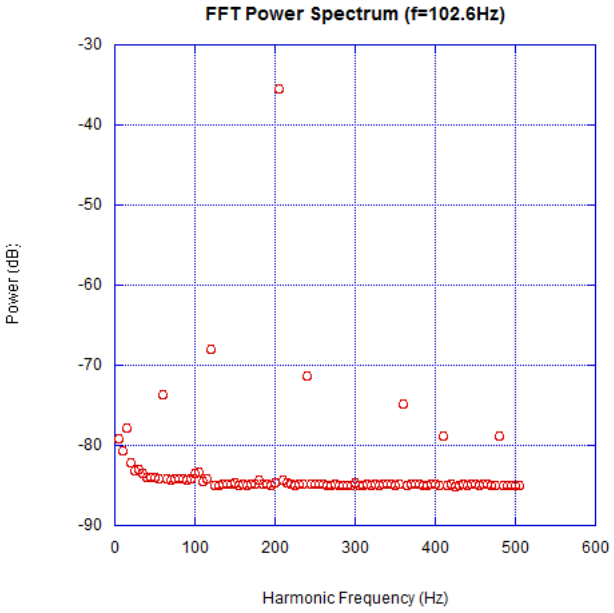
FFT Power Spectrum (f=102.6Hz)
Power (dB)
-30
-40
-50
-60
-70
-80
-90
0
100
200
300
400
500
600
Harmonic Frequency (Hz)

(4)

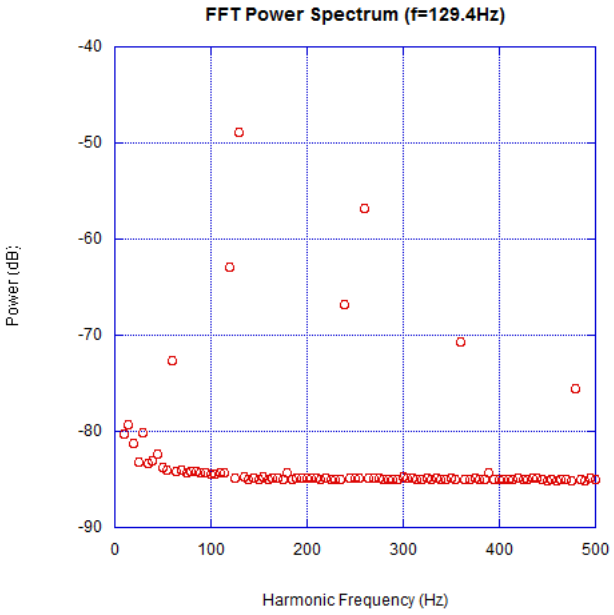
FFT Power Spectrum (f=129.4Hz)
Power (dB)
-40
-50
-60
-70
-80
-90
0
100
200
300
400
500
Harmonic Frequency (Hz)

(5)

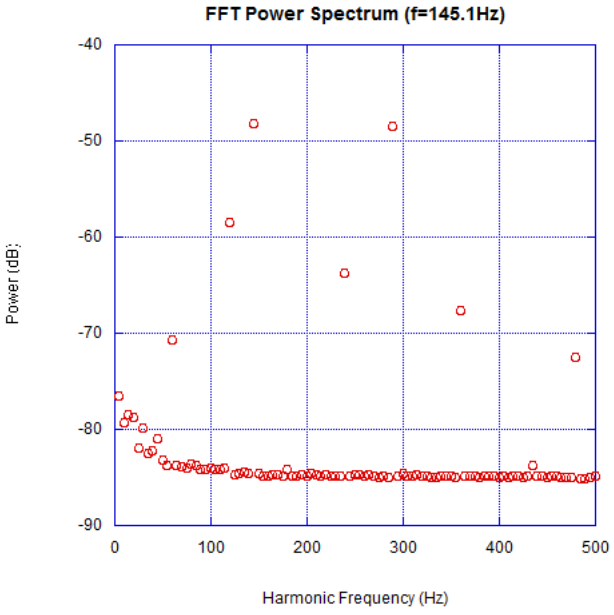
FFT Power Spectrum (f=145.1Hz)
Power (dB)
-40
-50
-60
-70
-80
-90
0
100
200
300
400
500
Harmonic Frequency (Hz)

(6)

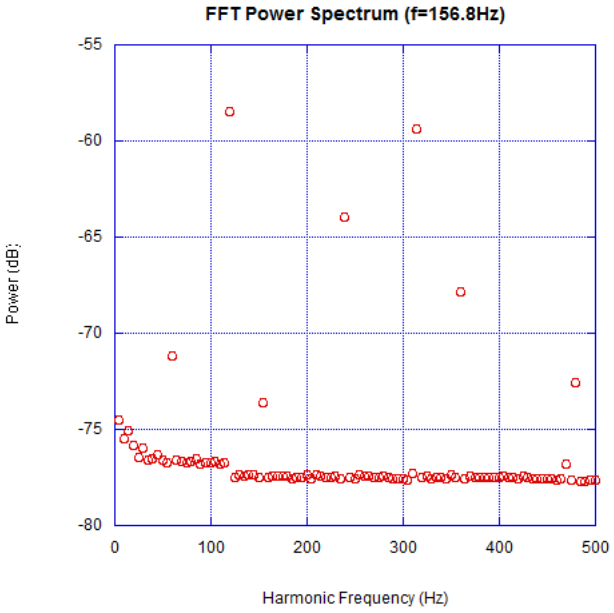
FFT Power Spectrum (f=156.8Hz)
Power (dB)
-55
-60
-65
-70
-75
-80
0
100
200
300
400
500
Harmonic Frequency (Hz)

(7)

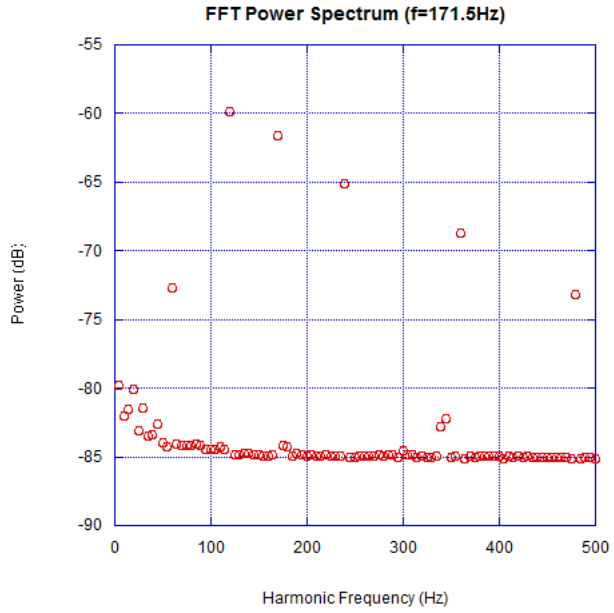
FFT Power Spectrum (f=171.5Hz)
Power (dB)
-55
-60
-65
-70
-75
-80
-85
-90
0
100
200
300
400
500
Harmonic Frequency (Hz)

(8)

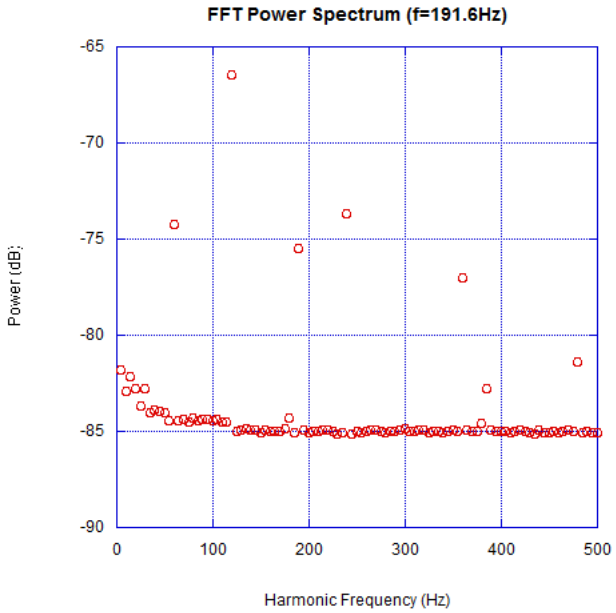


(9)

## Laser Diffraction Results on Cell A (Second Trial) (Hann Windowed)

**Figure A6.** FFT power spectra collected on LC cell A are presented below. These spectra are summed-averaged for 1000 sweeps and multiplied by a Hann window. The measured harmonics are as follows (1) $f = 9.5 \pm 5.0$Hz, $2f = 19.5 \pm 5.0$Hz, and $4f = 39.5 \pm 5.0$Hz(2) $f = 14.5 \pm 5.0$Hz and $2f = 29.5 \pm 5.0$Hz(3) $f = 24.5 \pm 5.0$Hz and $2f = 49.5 \pm 5.0$Hz (4) $f = 34.5 \pm 5.0$Hz, $2f = 74.5 \pm 10.0$Hz, $3f = 109.5 \pm 5.0$Hz, and $4f = 144.5 \pm 5.0$Hz (5) $f = 44.5 \pm 5.0$Hz and $2f = 89.5 \pm 7.0$Hz (6) $f = 69.5 \pm 5.0$Hz, $2f = 134.5 \pm 10.0$Hz, $3f = 204.5 \pm 5.0$Hz, and $4f = 274.5 \pm 5.0$Hz (7) $f = 74.5 \pm 5.0$Hz and $2f = 149.5 \pm 5.0$Hz(8) $f = 89.5 \pm 5.0$Hz and $2f = 179.5 \pm 5.0$Hz(9) $f = 129.5 \pm 5.0$Hz and $2f = 259.5 \pm 5.0$Hz(10) $f = 159.5 \pm 5.0$Hz (11)$f = 174.5 \pm 5.0$Hz and $2f = 344.5 \pm 5.0$Hz (12) $f = 189.5 \pm 5.0$Hz and $2f = 379.5 \pm 10.0$Hz

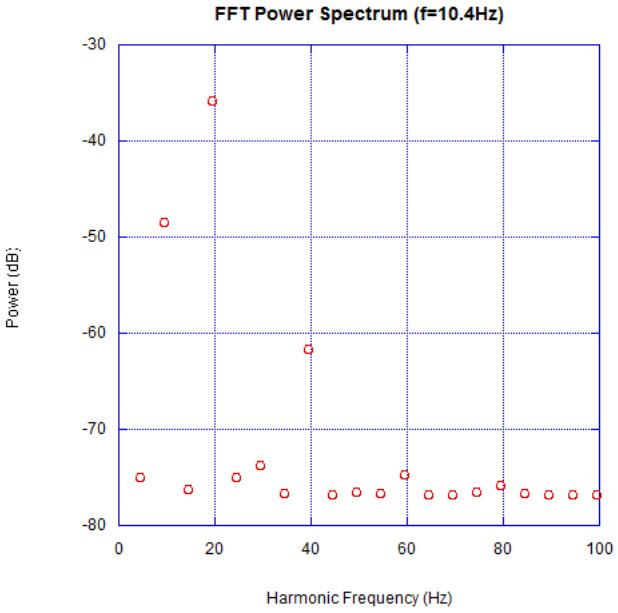
FFT Power Spectrum (f=10.4Hz)
Power (dB)
-30
-40
-50
-60
-70
-80
0
20
40
60
80
100
Harmonic Frequency (Hz)

(1)

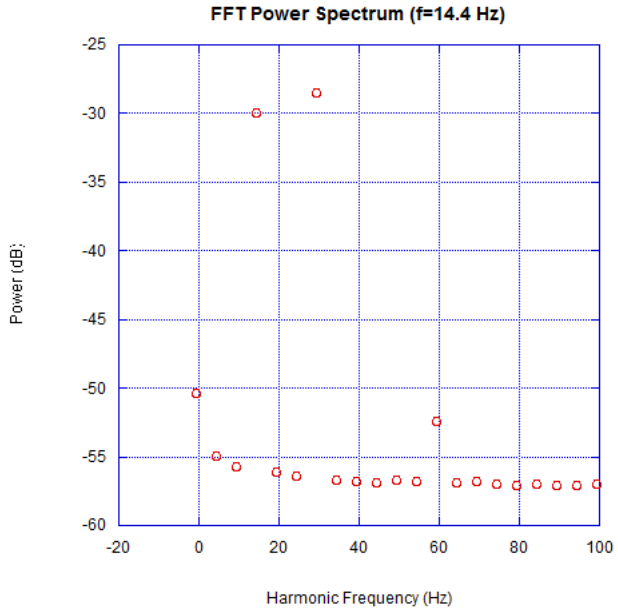
FFT Power Spectrum (f=14.4 Hz)
Power (dB)
-25
-30
-35
-40
-45
-50
-55
-60
-20
0
20
40
60
80
100
Harmonic Frequency (Hz)

(2)

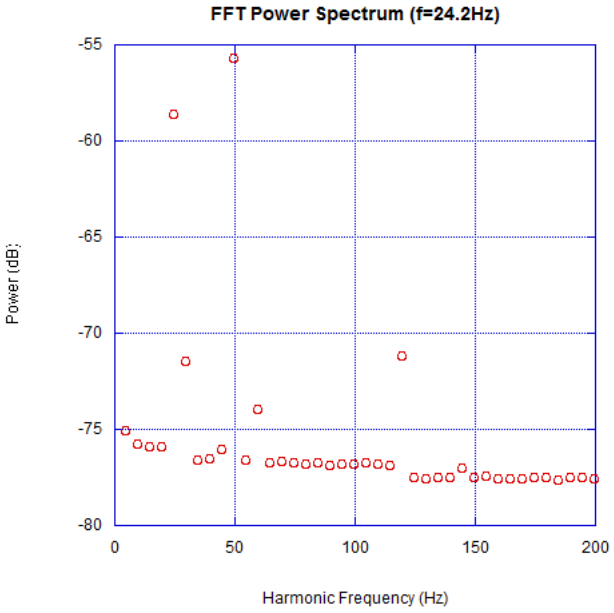
FFT Power Spectrum (f=24.2Hz)
Power (dB)
-55
-60
-65
-70
-75
-80
0
50
100
150
200
Harmonic Frequency (Hz)

(3)

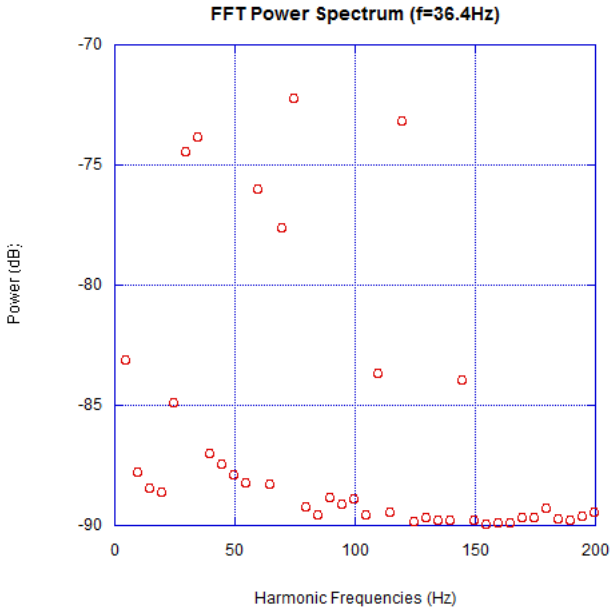
FFT Power Spectrum (f=36.4Hz)
Power (dB)
-70
-75
-80
-85
-90
0
50
100
150
200
Harmonic Frequencies (Hz)

(4)

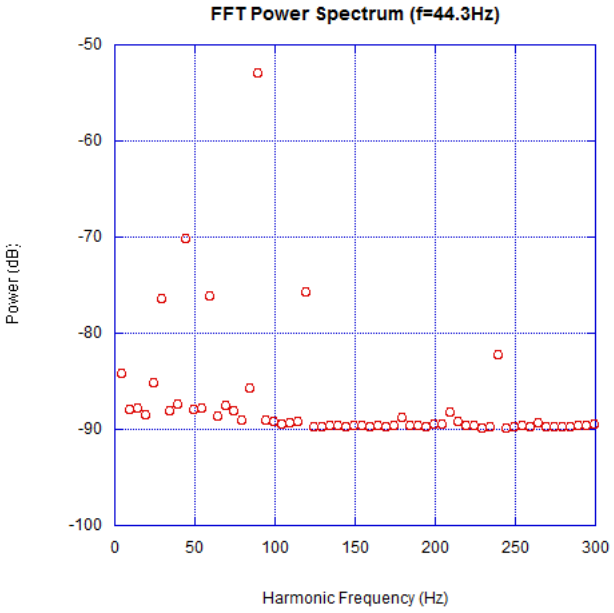
FFT Power Spectrum (f=44.3Hz)
Power (dB)
-50
-60
-70
-80
-90
-100
0
50
100
150
200
250
300
Harmonic Frequency (Hz)

(5)

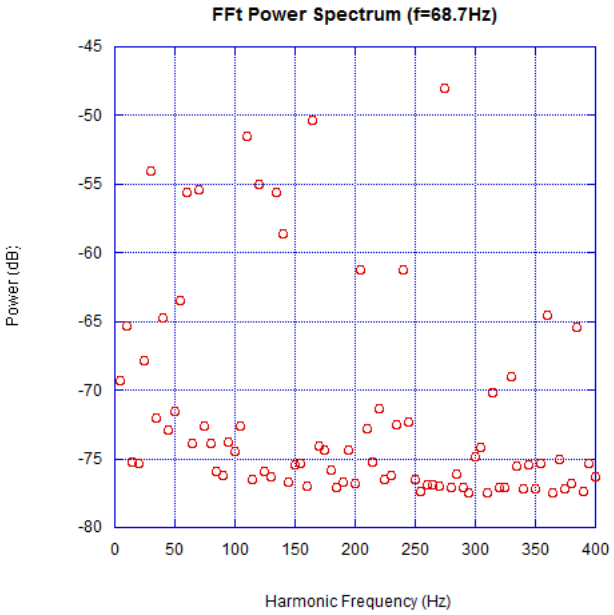
FFt Power Spectrum (f=68.7Hz)
Power (dB)
-45
-50
-55
-60
-65
-70
-75
-80
0
50
100
150
200
250
300
350
400
Harmonic Frequency (Hz)

(6)

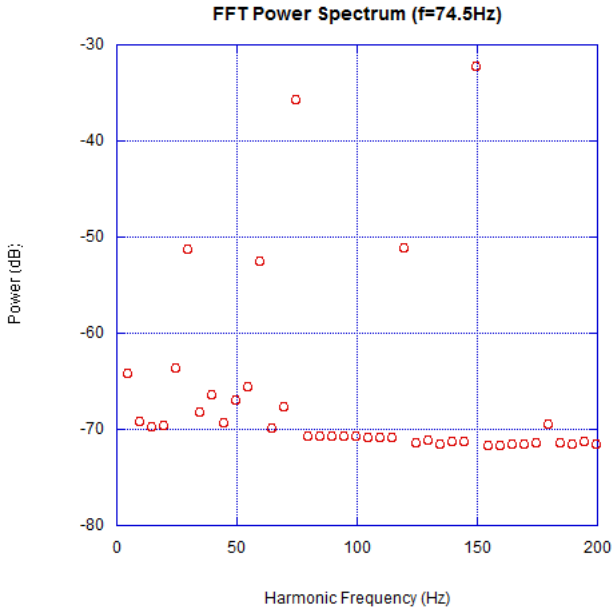
FFT Power Spectrum (f=74.5Hz)
Power (dB)
-30
-40
-50
-60
-70
-80
0
50
100
150
200
Harmonic Frequency (Hz)

(7)

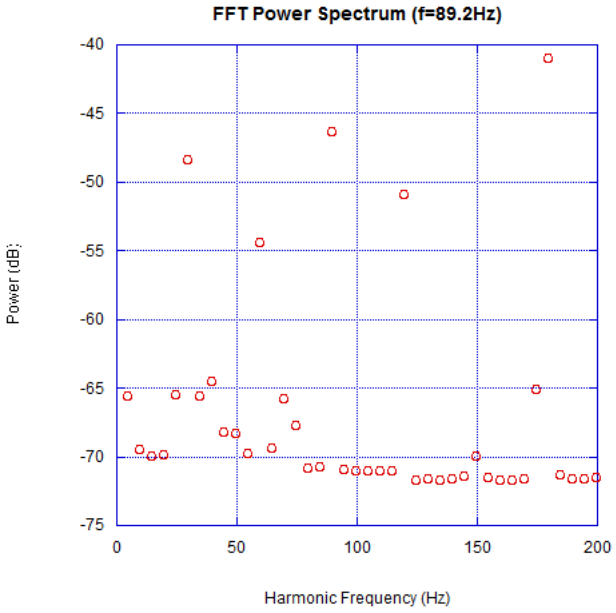
FFT Power Spectrum (f=89.2Hz)
Power (dB)
-40
-45
-50
-55
-60
-65
-70
-75
0
50
100
150
200
Harmonic Frequency (Hz)

(8)

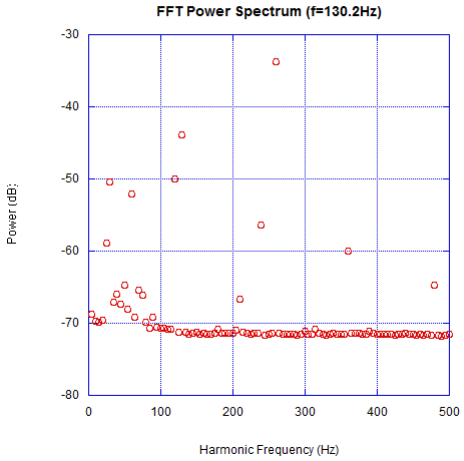
FFT Power Spectrum (f=130.2Hz)
Power (dB)
-30
-40
-50
-60
-70
-80
0
100
200
300
400
500
Harmonic Frequency (Hz)

(9)

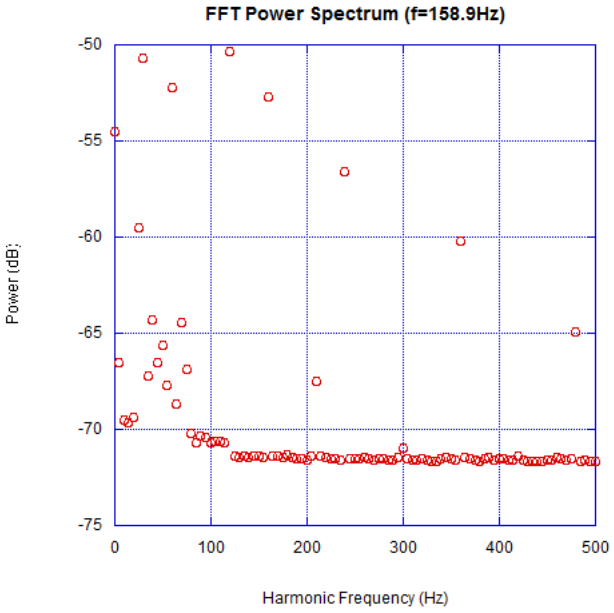
FFT Power Spectrum (f=158.9Hz)
Power (dB)
-50
-55
-60
-65
-70
-75
0
100
200
300
400
500
Harmonic Frequency (Hz)

(10)

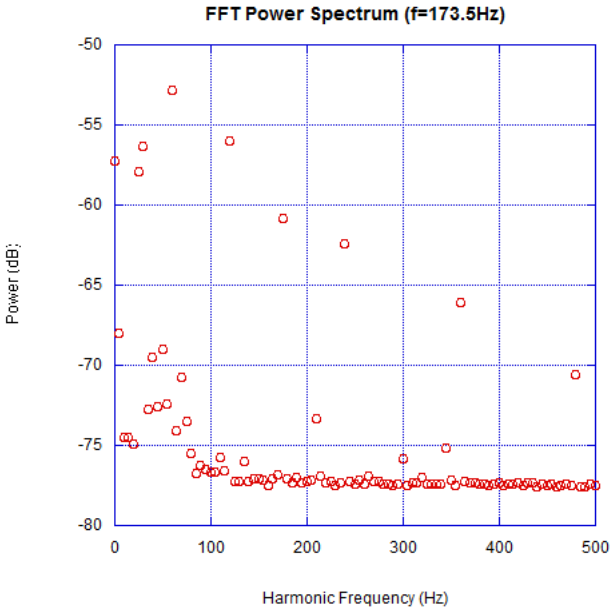
FFT Power Spectrum (f=173.5Hz)
Power (dB)
-50
-55
-60
-65
-70
-75
-80
0
100
200
300
400
500
Harmonic Frequency (Hz)

(11)

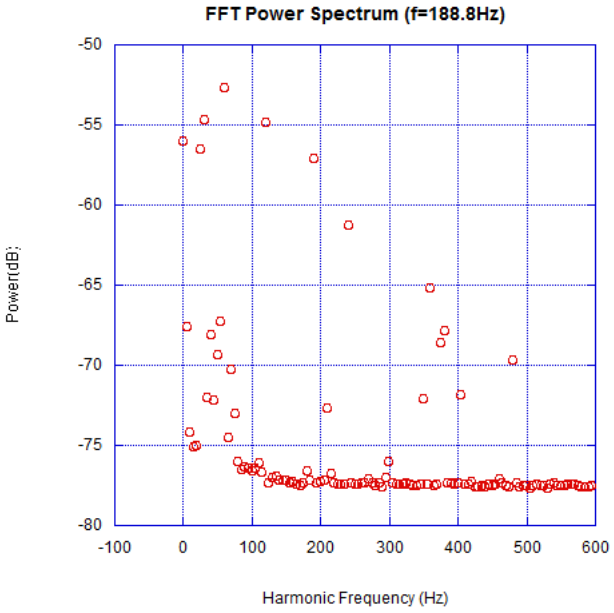
FFT Power Spectrum (f=188.8Hz)
Powerr(dB)
-50
-55
-60
-65
-70
-75
-80
-100
0
100
200
300
400
500
600
Harmonic Frequency (Hz)

(12)

## Second-Order Diffraction Fringes (Time Domain)

**Figure A7.** Intensity signals of (-2)-order fringes on cell A (second trial) at the following driving frequencies (1) $f$ =74.5Hz, (2) $f$ =89.2Hz, and (3) $f$ =130.2Hz. A 30Hz modulation is exhibited in these data.

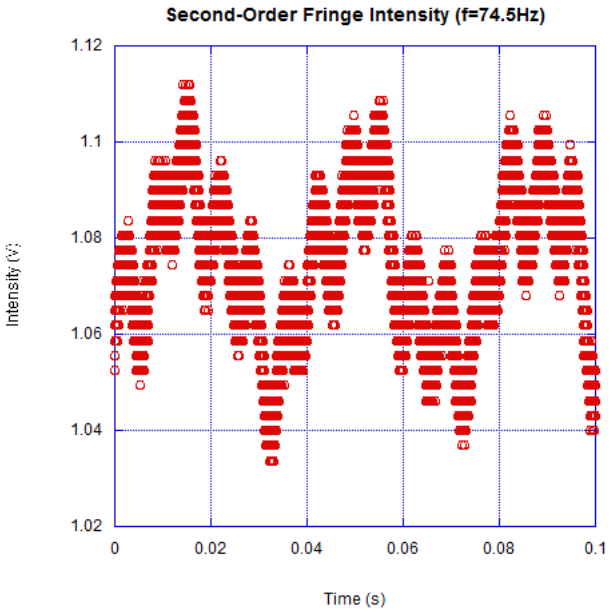


(1)

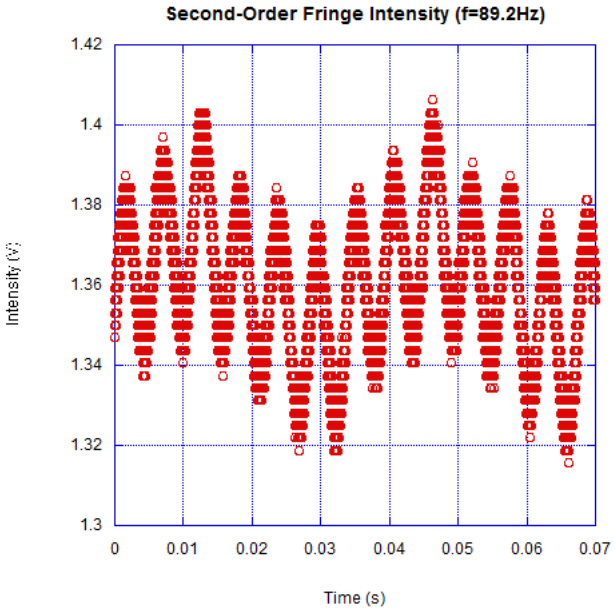


(2)

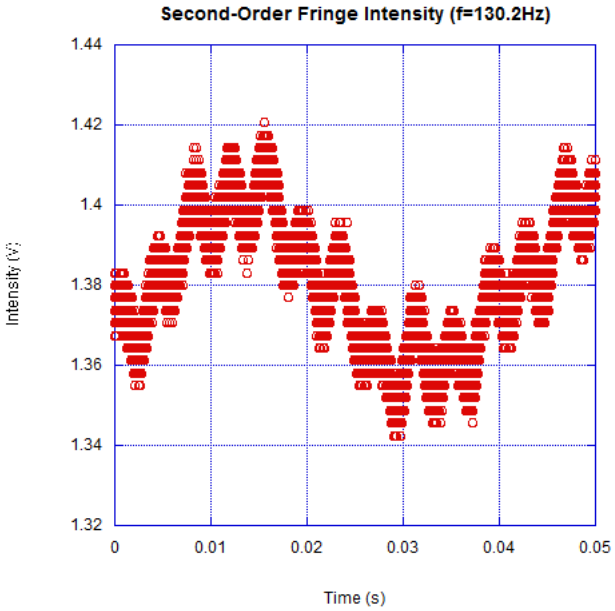


(3)

### Laser Diffraction Results on Central Fringe of Cell A (Hann Windowed)

**Figure A8.** FFT power spectra collected on LC cell A are presented below. These spectra are summed-averaged for 1000 sweeps and multiplied by a Hann window. The measured harmonics are as follows (1) $f = 44.5 \pm 5.0$Hz and $2f = 89.5 \pm 5.0$Hz (2) $2f = 34.5 \pm 5.0$Hz and $3f = 49.5 \pm 5.0$Hz(3)$2f = 134.5 \pm 5.0$Hz (4) $2f = 179.5 \pm 5.0$Hz (5) $f = 134.5 \pm 5.0$Hz and $2f = 269.5 \pm 5.0$Hz (6) $f = 159.5 \pm 5.0$Hz, $2f = 319.5 \pm 5.0$Hz, and $3f = 479.5 \pm 5.0$Hz (7) $f = 169.5 \pm 5.0$Hz and $2f = 339.5 \pm 5.0$Hz(8)$f = 189.5 \pm 5.0$Hz, $2f = 379.5 \pm 5.0$Hz, and $3f = 569.5 \pm 5.0$Hz

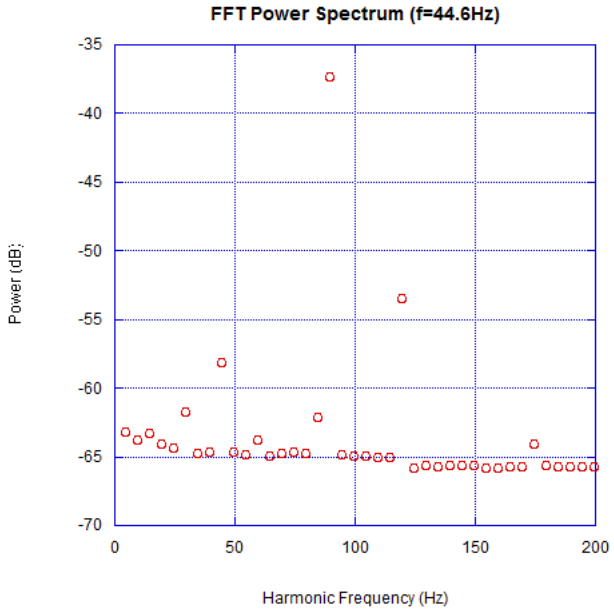
FFT Power Spectrum (f=44.6Hz)
Power (dB)
-35
-40
-45
-50
-55
-60
-65
-70
0
50
100
150
200
Harmonic Frequency (Hz)

(1)

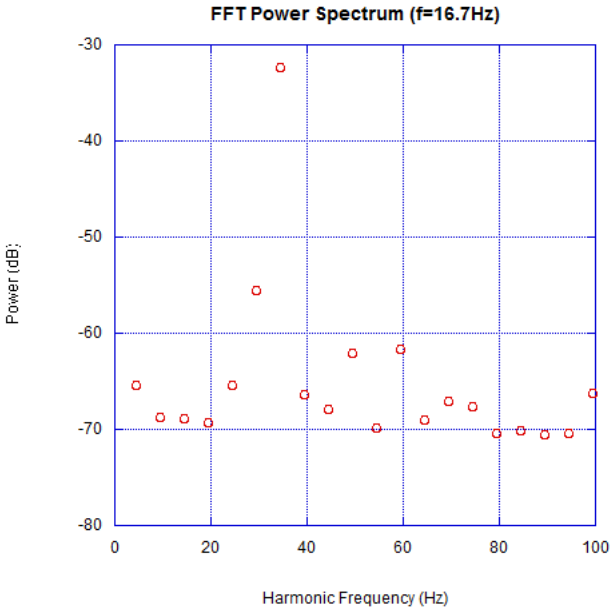
FFT Power Spectrum (f=16.7Hz)
Power (dB)
-30
-40
-50
-60
-70
-80
0
20
40
60
80
100
Harmonic Frequency (Hz)

(2)

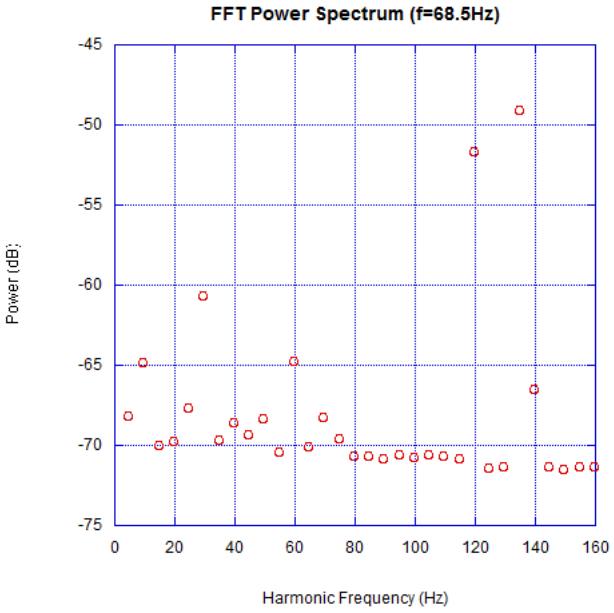
FFT Power Spectrum (f=68.5Hz)
Power (dB)
-45
-50
-55
-60
-65
-70
-75
0
20
40
60
80
100
120
140
160
Harmonic Frequency (Hz)

(3)

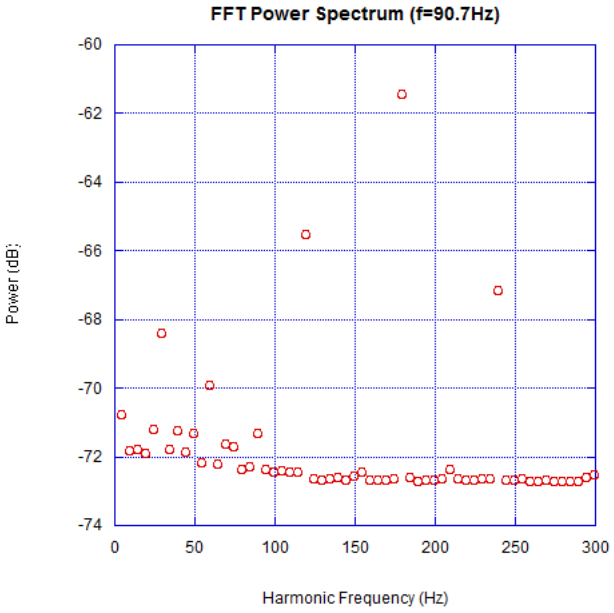
FFT Power Spectrum (f=90.7Hz)
Power (dB)
-60
-62
-64
-66
-68
-70
-72
-74
0
50
100
150
200
250
300
Harmonic Frequency (Hz)

(4)

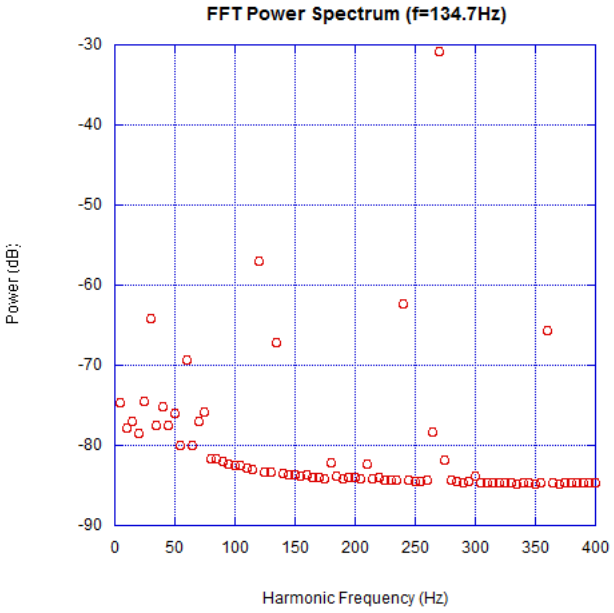
FFT Power Spectrum (f=134.7Hz)
Power (dB)
-30
-40
-50
-60
-70
-80
-90
0
50
100
150
200
250
300
350
400
Harmonic Frequency (Hz)

(5)

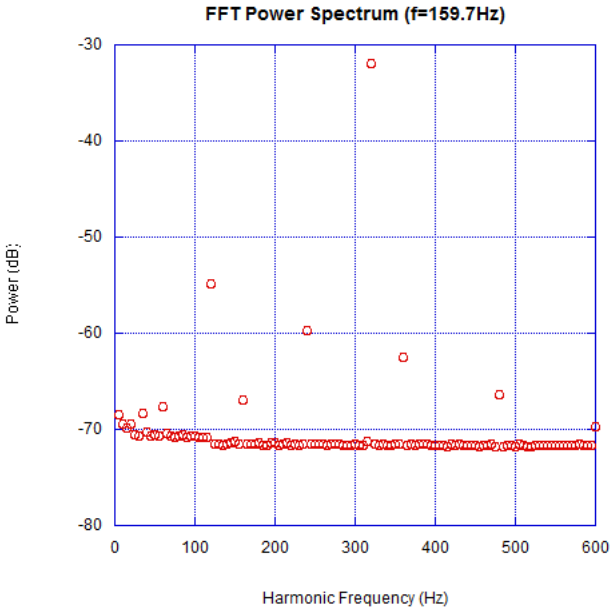
FFT Power Spectrum (f=159.7Hz)
Power (dB)
-30
-40
-50
-60
-70
-80
0
100
200
300
400
500
600
Harmonic Frequency (Hz)

(6)

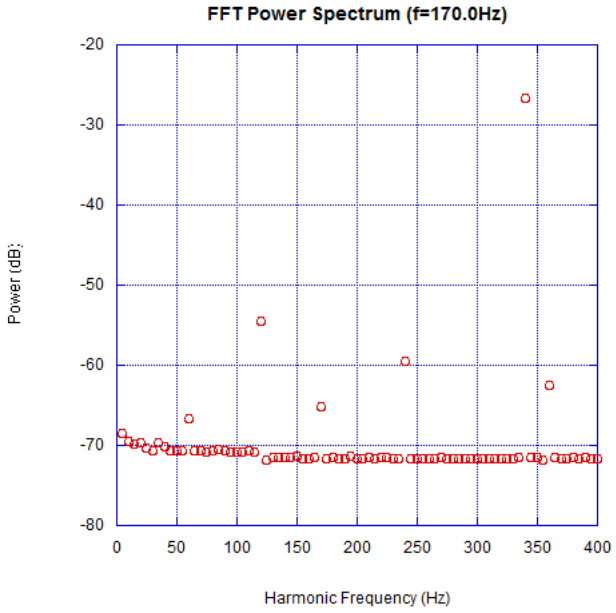


(7)

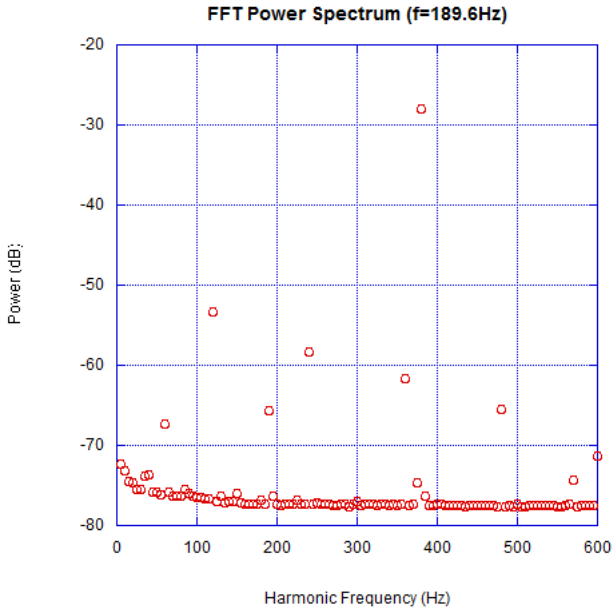


(8)

## Additional Results for the $I_{-4}$ Fringe

**Figure A9.** FFT power spectra collected on LC cell A are presented below. These spectra are summed-

averaged for 1000 sweeps and multiplied by a Hann window. The measured harmonics are as follows $f = 169.5 \pm 5.0$Hz and $2f = 339.5 \pm 5.0$Hz

